THE INTERACTION OF TECTONIC AND MAGMATIC PROCESSES IN THE LONG VALLEY CALDERA, CALIFORNIA

A DISSERTATION

SUBMITTED TO THE DEPARTMENT OF GEOPHYSICS

AND THE COMMITTEE ON GRADUATE STUDIES

OF STANFORD UNIVERSITY

IN PARTIAL FULFILLMENT OF THE REQUIREMENTS

FOR THE DEGREE OF

DOCTOR OF PHILOSOPHY

Stephanie G. Prejean

February 2002

I certify that I have read this dissertation and that in my opinion it is fully adequate, in scope and quality, as a dissertation for the degree of Doctor of Philosophy.

_____
Mark D. Zoback (Principal Advisor)

I certify that I have read this dissertation and that in my opinion it is fully adequate, in scope and quality, as a dissertation for the degree of Doctor of Philosophy.

_____
William L. Ellsworth

I certify that I have read this dissertation and that in my opinion it is fully adequate, in scope and quality, as a dissertation for the degree of Doctor of Philosophy.

_____
Gregory C. Beroza

Approved for the University Committee on Graduate Studies:

_____

Abstract

The Long Valley caldera of eastern California is a hazardous province where tectonic and magmatic processes interact to drive on-going seismicity and deformation. The caldera is located on the boundary between the Basin and Range province and the Sierra Nevada batholith along the actively extending Sierra Nevada range-bounding normal faults. It is not clear if Basin and Range tectonic extension drives magmatic intrusion in this area or if magmatic activity is independent of regional tectonic processes. Magmatic intrusion into the caldera and extensional faulting are temporally coupled, yet it is not clear how these processes mechanically interact and potentially trigger each other.

In this dissertation, I investigate the interaction between tectonic and magmatic processes in the Long Valley caldera over a range of scales, with the goal of developing a comprehensive model for the observed activity in the caldera. To gain a first order understanding of the mechanics by which the Long Valley area deforms, local fault geometries need to be established. To this end I relocated seismicity in the greater Long Valley area. The resulting high-resolution locations reveal a systematic fabric of faults within the caldera and in the Sierra Nevada basement rock to its south. From the focal mechanisms associated with individual faults, I developed a kinematic model for seismic deformation in the Long Valley caldera. Seismicity within the caldera occurs primarily on a set of east/west-trending right-lateral faults in the caldera's south moat. Since the south moat is located in a left step of the Sierra Nevada range-bounding normal faults, the south moat shear zone in essence forms a "transform" zone between loci of Basin and Range extension. In the Sierra Nevada block, directly south of the caldera, tectonic extension is accommodated by an east-dipping oblique-normal fault and two left-lateral strike-slip faults in its hanging wall. The location of these faults in the footwall of the Sierra Nevada range-bounding normal fault at this latitude, suggests that Basin and Range extension is potentially cutting into the Sierra Nevada batholith in this area.

To understand better the mechanical interaction of tectonic and magmatic processes at the regional scale, I performed a series of focal mechanism stress inversions in the caldera area. The inversions show that around the caldera the minimum compressive stress is perturbed from the more regional WNW–ESE direction to a NE–SW orientation. Dislocation modeling of the mapped stress

field reveals that the stress perturbation cannot be explained solely by the intrusion of magma beneath the resurgent dome, but may reflect the large-scale left-stepping offset in the Sierran range-bounding normal faults. Thus, the direction of fault slip seems to be controlled by regional tectonic processes rather than local magmatic processes. This implies that Basin and Range extension governs activity in the caldera and possibly provides conduits for ascending magma.

To understand the relationship between tectonic and magmatic processes at the scale of the earthquake source, I investigate the influence of magmatic activity on earthquakes by examining the source processes of earthquakes and by studying the spatial and temporal development of seismicity during a crisis episode. The great majority of earthquakes in the caldera region appear to be typical "tectonic" earthquakes with source parameters similar to those observed in non-volcanic regions. However, a small number of earthquakes show magmatic signatures. A close examination of a seismicity swarm on November 22, 1997 in the western south moat of the caldera reveals that the swarm was triggered directly by magmatically derived fluids. Thus, although earthquakes slip in accordance with the regional tectonic stress field, magmatic activity can trigger seismicity by decreasing the effective normal stress across faults.

Acknowledgments

I have many people to thank for their help with my Ph.D. First I'd like to thank my advisors, Mark Zoback and Bill Ellsworth. They taught me the power of seismology and tectonophysics in investigating the Earth, but more importantly, they taught me how to think like a scientist. They have been wonderful role models, professionally and personally.

There are countless others at Stanford and the US Geological Survey in Menlo Park who were a great help to me over the years. I'd like to thank all those who support the Stanford-USGS Fellowship and those who support a close connection between the two institutions in general. Greg Beroza, Norm Sleep, George Thompson, and David Hill have been wonderful scientific advisors in my years at Stanford. The help of Satoshi Ide, David Schaff, Eva Zanzerkia, and Felix Waldhauser greatly improved the work described in this thesis. The members of my research group have been supportive in countless ways over the years, so my sincere thanks to them: Balz Grollimund, David Wiprut, Lourdes Colmenares, Naomi Boness, and Paul Hagin. I particularly thank John Townend for many long evening discussions about research and for hacking through the frist draft of every paper I wrote. Dan and Peter Cervelli, Aya Kameda, and Shelley Kenner were great friends in my years here.

I must thank the dear friends and advisors down south whose encouragement got me to Stanford in the first place. David Neblett, my eigth grade Earth science teacher from Clarksville, TN and Phili Deboo, my Geology 101 teacher from Memphis, TN inspired my interest in geology. Arch Johnston, Buddy Schweig, Paul Bodin, Joan Gomberg, and Mike Ellis from CERI in Memphis, TN introduced me to geophysics and pointed me toward Stanford. I must also thank my dear friends from Memphis who have helped me in coutless ways: Tania Brown, Debi Kilb, Becky Knight, and Gisele Goldstein.

I owe tremendous thanks to Stephan Bergbauer for all his help at home and at work in my last year at Stanford. He proof-read my thesis. He fed me. He encouraged me to keep working. He encouraged me to take breaks. Thank you, Steph.

Finally, I thank my parents for always keeping the house full of books. I thank my Mom for buying me telescopes, microscopes, and prisms and for tolerating my "mold colony experiments" on old bread beneath my bed and my "chemistry experiments" with various household chemicals in my closet. I think my Dad for handing me a book when I asked a question rather than simply telling me the answer.

Table of Contents

List of Tables

List of Illustrations

Chapter 1

INTRODUCTION: THE INTERACTION OF TECTONIC AND MAGMATIC PROCESSES IN THE LONG VALLEY CALDERA, CALIFORNIA

1.1 Abstract

The Long Valley caldera is situated on the western border of the Basin and Range province in a left-step of the actively extending Sierra Nevada range-bounding normal faults. Since 1980, 32 **M** 5 and greater earthquakes and more than 2700 **M** 3 and greater earthquakes have occurred in or near the Long Valley caldera, making it one of the most seismically active regions in California. During this time of seismic activity, the caldera's resurgent dome uplifted ~80 cm due to the intrusion of magma deep within the caldera. Thus, geologic activity in the caldera seems to be controlled by a complex interplay of tectonic and magmatic processes. The mechanics of how tectonic and magmatic processes interact to drive the ongoing seismicity and deformation in the Long Valley caldera must be understood to properly evaluate recent activity in the area and its implications for hazard.

In this dissertation, I investigate the interaction of tectonic and magmatic processes in the Long Valley caldera over a wide range of scales. Specifically, I examine if Long Valley earthquakes occur in response to local magmatic processes or regional tectonic extension. I also characterize the source processes of earthquakes to understand better the physics of rupture and the processes that trigger failure. Finally, I describe the 1997-98 episode of unrest in detail with the goal of understanding the succession of events. This chapter gives a brief introduction to the Long Valley caldera in section 1.2. Section 1.3 describes the structure and content of this dissertation and summarizes the results.

1.2 Background: The Long Valley Caldera

1.2.1 *Tectonic Setting*

The Long Valley caldera is a ~30 km by ~17 km oval-shaped caldera with a resurgent dome in its center, situated north of the Owens Valley and south of the Mono Basin, in the depression between the White Mountains and the Sierra Nevada (Figure 1.1). It is located on the border of the Basin and Range province and the Sierra Nevada, in a left-step of the major Sierra Nevada range-bounding faults. Recurring slip across these east-dipping normal faults constitutes the western margin of active Basin and Range west-northwest/east-southeast extension.

The seismic belt in which Long Valley is located has been one of the most seismically active areas of California in historical time (Hill et al., 1985). The Owens Valley fault, whose northern terminus is ~50 km southeast of the caldera, was the site of the great 1872 ~**M** 8 Owens Valley earthquake (Cramer and Toppozada, 1980). The Hilton Creek fault, which extends to the south along the Sierra Nevada margin from the southeastern boundary of the caldera (Figure 1.1), has accommodated at least 20 m of slip in the last 10,000 years based on displacement of glacial moraines (Clark and Gillespie, 1981). Historical earthquakes that most likely ruptured the Hilton Creek fault include four **M** 5 and greater earthquakes and one **M** 6 earthquake in 1941 (Cramer and Toppozada, 1980).

The Hartley Springs normal fault and other Sierra Nevada range bounding faults, which extend northward from the northwestern rim of the caldera (Figure 1.1), have been less active during the Holocene than the Hilton Creek fault to the caldera's south (Bursik and Sieh, 1989; Clark and Gillespie, 1981). This cessation of extensional faulting north of the caldera seems to indicate that regional Basin and Range extension has recently been accommodated by the Holocene intrusion of the Mono/Inyo dike(s) described below (Bursik and Sieh, 1989).

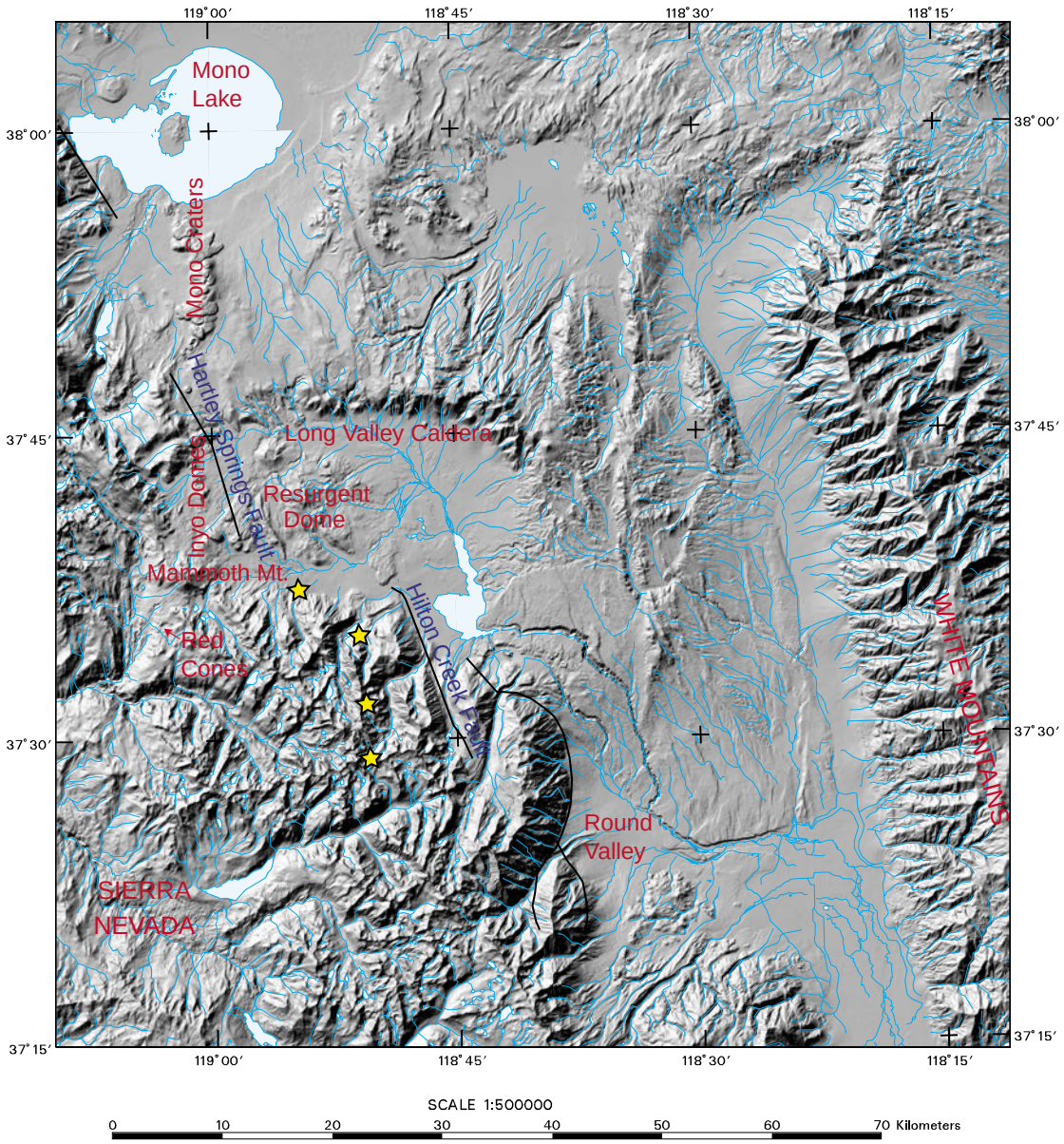

Figure 1.1 - Shaded relief map of the Long Valley caldera area. Blue lines are the Sierra Nevada range bounding normal faults. Yellow stars are the epicenters of the May 1980 ~M 6 earthquakes. Figure courtesy of David Hill.

1.2.2 *Volcanic History*

The Long Valley caldera formed during the catastrophic eruption of the Bishop tuff ~760,000 years ago (~600 km^3 of magma erupted in days to weeks [Hildreth, 1979]). Since that time the caldera has experienced many smaller intermittent eruptions (see Bailey, 1989, for summary). Post-Bishop tuff eruptions occurred on the caldera's resurgent dome, along the caldera's ring fracture system, and in the caldera's west moat. The most recent volcanic activity in the area occurred along the Mono / Inyo dike chain. This chain is manifested by a 40 km north–south trending alignment of rhyolitic domes and craters. The chain extends from the Red Cones, about 3 km south of Mammoth Mountain, through the caldera's west moat, to Mono Lake, ~30 km north of the caldera (Figure 1.1). The most recent eruptions occurred roughly 500 years ago at the northern terminus of this dike chain in Mono Lake (Bailey, 1989).

1.2.3 *Recent Unrest*

The occurrence of 4 **M** 6 and greater earthquakes in the Long Valley area within just three days in May of 1980 (Figures 1.1 and 1.2), alerted the US Geological Survey to the need for improved monitoring of seismicity and deformation in the caldera area. Since that time, 32 **M** 5 and greater earthquakes and more than 2700 **M** 3 and greater earthquakes have occurred in or near the Long Valley caldera (Figures 1.2 and 1.3). The most energetic seismic swarms occurred in 1980, 1990 / 91, 1996, 1982 / 83, 1997 / 98 (in order of decreasing moment) (Hill et al., in press). The seismicity in these "crises" was concentrated primarily in the south moat of the caldera and in the footwall of the Hilton Creek fault in the Sierra Nevada basement rock immediately south of the caldera (Figure 1.3).

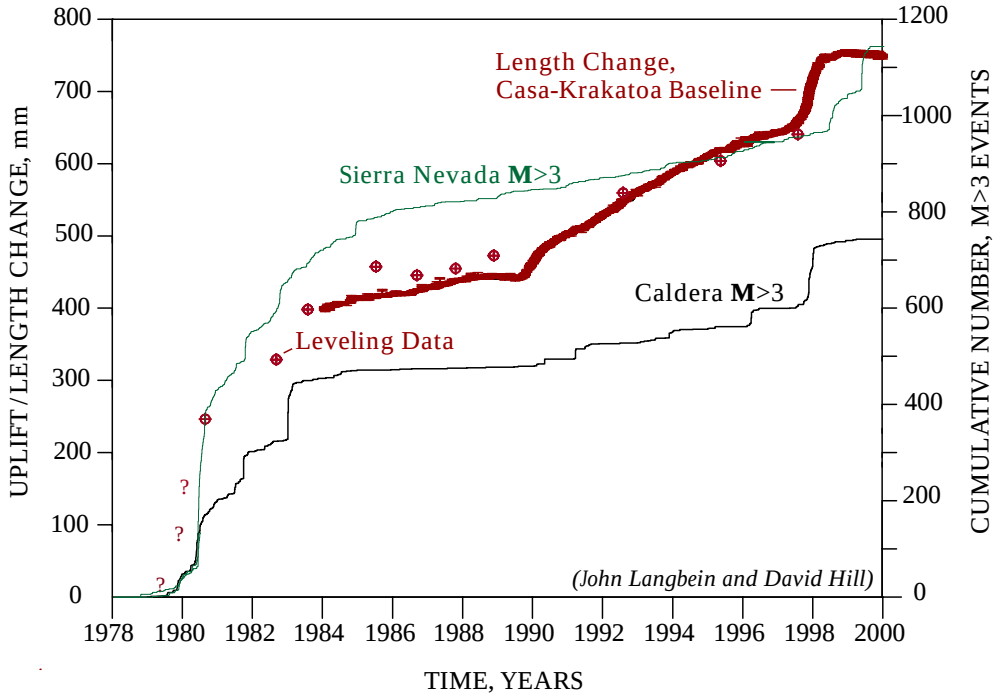

Figure 1.2 - Uplift and seismicity in the Long Valley caldera since 1980. Black line shows intracaldera seismicity. Green line shows seismicity in the Sierra Nevada block directly south of the caldera. See Chapter 5, Figure 5.2 for location of Casa–Krakatoa baseline. Figure courtesy of David Hill.

Each of the recent major swarms was accompanied by and generally preceded by increased uplift rates of the caldera's resurgent dome (Figure 1.2), presumably due to the emplacement of magma deep within the center of the caldera (Savage and Cockerham, 1984; Langbein, 1989; Langbein et al., 1995; Marshall et al., 1997; Battaglia et al., 1999). Resurgence rates reached a maximum of 2 mm/day in 1997/98, and have culminated in a total of ~80 cm of uplift since the late 1970's (Hill et al., in press).

Although most of the recent earthquakes that have occurred in the Long Valley region have been typical "tectonic" earthquakes, characterized by shear

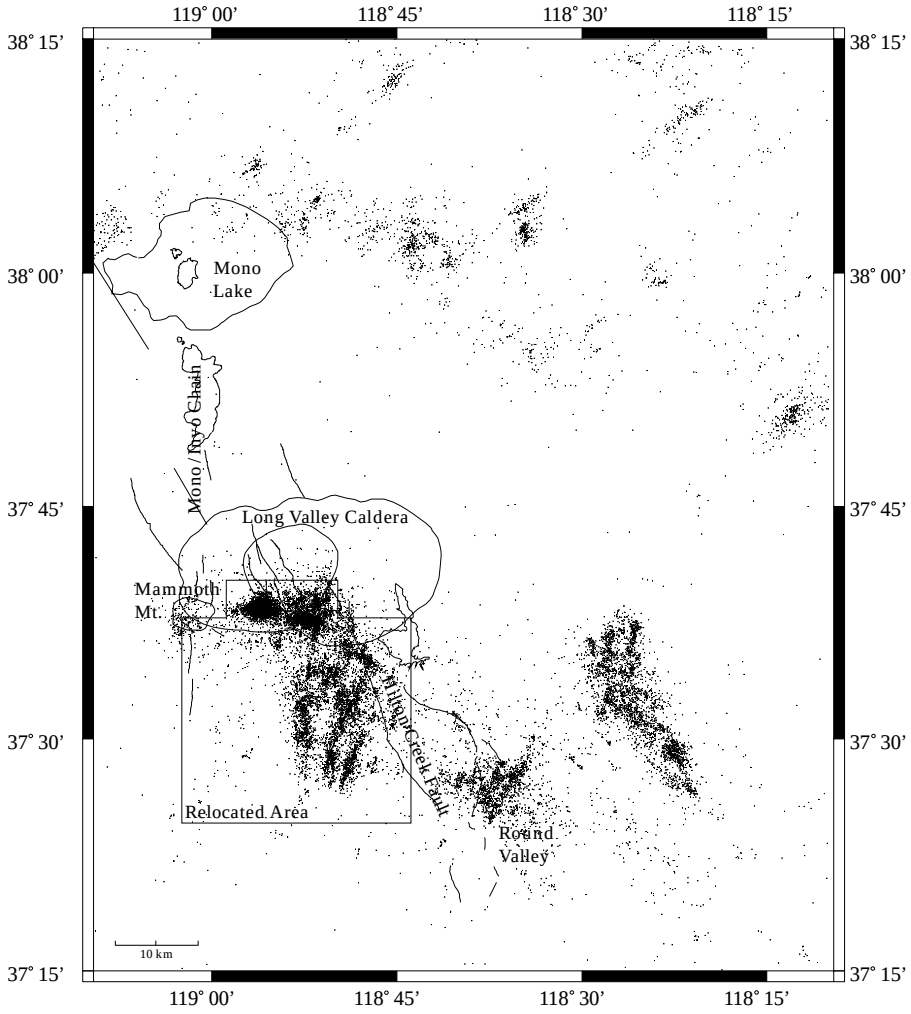

Figure 1.3 - All **M** 2 and greater earthquakes in the greater Long Valley caldera area between 1980 and 2000. Box shows area of earthquakes relocations presented in this paper. Thin lines denote fault traces.

failure of brittle rock, some earthquakes appear to have been influenced by magmatic activity. These "magmatic" events have been identified by long period and hybrid long period waveforms (Pitt and Hill, 1994; Cramer and McNutt, 1997), harmonic waveforms (Hough et al, 2000), and non-double couple focal plane solutions (Julian and Sipkin, 1985; Dreger et al., 2000). The most notable "magmatic" swarm occurred beneath Mammoth Mountain in 1989 (Hill et al., 1990).

This swarm appears to have triggered the release of large amounts of carbon dioxide gas from beneath Mammoth Mountain (Farrar et al., 1995).

Since the 1980 **M** 6 earthquakes, the need to evaluate hazard in the Long Valley area has led to an extensive and growing monitoring program guided by the US Geological Survey. The Long Valley Observatory (LVO) includes a dense surface seismic network, a borehole seismometer, continuous strain and tilt meters, continuous water level monitors in several area wells, carbon dioxide gas gauges in the vicinity of Mammoth Mountain, and frequent leveling, electronic distance measuring (EDM), and most recently, GPS surveys. By integrating these data, the behavior of the Long Valley caldera during crises can be observed at a variety of scales and integrated into a complete model for activity at depth.

1.3 Structure and Content of this Dissertation

In this dissertation, I investigate the interaction of tectonic and magmatic processes in the Long Valley caldera over a range of scales. The research is divided into five chapters. In Chapter 2, I determine the geometry of recently active faults in the Long Valley caldera area using high-resolution earthquake locations. In Chapter 3, I describe the sense of slip on faults based on earthquake focal mechanisms and develop a kinematic model for recent seismic deformation in the Long Valley area. Based on this kinematic model, I discuss the interaction between tectonic and magmatic processes at local scales. Also in Chapter 3, I investigate the interaction of tectonic and magmatic processes at the regional scale by mapping the stress field using focal mechanism stress inversions. I use the mapped stress field to infer which processes drive seismicity in the caldera overall. Chapters 4 and 5 investigate the interaction of tectonic extension and magmatism at small scales by examining earthquake sources and processes that trigger earthquakes. Specifically, in Chapter 4, I quantify attenuation in the caldera and characterize

the source processes of typical "tectonic" earthquakes. In Chapter 5, I describe magmatically influenced earthquakes and develop a model for the development of the 1997-98 crisis episode.

1.3.1 *Interaction of Tectonic and Magmatic Processes at the Local Scale* (Chapters 2 and 3)

To understand seismic deformation in the Long Valley area and its relationship to magmatic inflation and regional tectonics, it is necessary to determine the geometry and sense of slip of active faults. To this end, I relocate earthquakes in the greater Long Valley area in Chapter 2 to reveal fault geometries, and propose a kinematic model of seismic deformation in the Long Valley area based on earthquake focal mechanisms in Chapter 3.

Earthquake locations reveal that seismicity in the south moat of the caldera and Sierra Nevada block to its south generally occurs on a complex fabric of discrete, planar faults. Faults in the south moat form an east/west-trending, right-lateral transform zone between the northern terminus of the Hilton Creek fault in the southeastern caldera and the southern limit of the Mono/Inyo dike chain in the southwestern caldera. In the Sierra Nevada basement rock south of the caldera, seismicity occurs on an east-dipping oblique normal fault, which is located ~10 km west of the Hilton Creek fault, and on two left-lateral strike-slip faults in its hanging wall.

Seismicity in the caldera and Sierra Nevada appear to be generally tectonic in nature because it occurs on discrete planar faults. In contrast, seismicity beneath Mammoth Mountain does not occur on well-defined faults. Rather, Mammoth Mountain seismicity in 1989 occurs in a northeast-trending keel-shaped volume with two rings of seismicity above it. The shape of these structures strongly suggests that they are reflecting the local intrusion of magma.

1.3.2 *Interaction of Tectonic and Magmatic Processes at the Regional Scale* (Chapter 3)

To understand the interaction of tectonic and magmatic processes at the regional scale, it is necessary to have knowledge of the regional stress field and its local variations. To this end, I performed a detailed suite of focal mechanism stress inversions to map the stress in the greater Long Valley region (Chapter 3). Results indicate that the regional stress field, which is characterized by west-northwest/east-southeast extension, is strongly perturbed in the vicinity of the caldera to northeast/southwest extension. Dislocation modeling suggests that this perturbation is not caused by the inflation of a magma chamber beneath the resurgent dome. Rather, the observed stress perturbation may result from the left-step in the locus of tectonic extension across the caldera's south moat. Thus, although seismic swarms may be triggered by local magmatic activity (see section 1.3.3), faults slip in response to Basin and Range extension.

1.3.3 *Interaction of Tectonic and Magmatic Processes at the Scale of the Earthquake Source* (Chapters 4 and 5)

Finally, to understand better the interaction of tectonic and magmatic processes at the scale of the earthquake source, it is necessary to determine if the crust fails in pure shear, or if the source processes of earthquakes involve opening or resonance due to the movement of magma or magmatically-derived fluids. I address these questions in Chapters 4 and 5 by examining the details of the seismic source as recorded by a 2 km deep borehole seismometer and by carefully observing the spatial and temporal development of the 1997-98 seismic swarm.

Chapter 4 examines the source processes of typical "tectonic" earthquakes, as recorded in the quiet environment of a deep borehole. The majority of Long

Valley earthquakes are "tectonic" events, characterized by pure shear failure in brittle crust. Static stress drops and apparent stresses of "tectonic" Long Valley earthquakes range from 0.01 MPa to 30 MPa, and scale similarly to earthquakes in other non-volcanic regions (e.g. Abercrombie, 1995). Thus, source parameters of most Long Valley earthquakes are similar to those in purely tectonically deforming regions.

As Chapter 5 explains, however, many earthquakes which occurred in the western south moat of the Long Valley caldera in 1997 appear to have been magmatically-influenced. A high pressure transient emanating from a magmatic source seems to have triggered a radially migrating front of seismicity in the western south moat on November 22, 1997. The source processes of these earthquakes have unusual characteristics which are commonly observed in volcanic areas and appear to reflect the movement of fluids. Therefore, although tectonic processes appear to drive seismicity in the caldera overall, magmatic processes govern the development of individual swarms and may trigger earthquakes by reducing the effective normal stress across faults.

Chapter 2

ACTIVE FAULTS IN THE LONG VALLEY CALDERA 1980-2000, REVEALED BY HIGH-RESOLUTION EARTHQUAKE LOCATIONS

A shorter version of this chapter combined with Chapter 3 will be published with Bill Ellsworth, Mark Zoback, and Felix Waldhauser as coauthors in the *Journal of Geophysical Research*.

2.1 Abstract

We have determined high-resolution hypocenters for 45,000+ earthquakes that occurred between 1980 and 2000 in the Long Valley caldera area using a double-difference earthquake location algorithm and routinely-determined arrival times. The locations reveal numerous discrete fault planes in the southern caldera and adjacent Sierran block. Intracaldera faults are closely spaced and include a series of east / west-striking faults beneath the caldera's south moat, and a series of more northerly-striking faults beneath the caldera's resurgent dome. Intracaldera faults all dip steeply (60˚–90˚) toward the northeast and tend to rupture in brief, intense seismic swarms. Seismicity in the Sierra Nevada basement rock south of the caldera is confined to a crustal block bounded on the west by an east-dipping fault and on the east by the Hilton Creek fault. Two northeast-striking vertical faults are responsible for most of the seismicity within this block. Unlike in the south moat and Sierra Nevada block, seismicity beneath Mammoth Mountain does not occur on discrete, planar faults. Rather, Mammoth Mountain seismicity in 1989 is best described as a northeast-trending keel-like feature with two rings above it. This structure may be directly reflecting the local intrusion of magma.

2.2 Earthquake Locations

In order to understand processes driving activity in the Long Valley caldera, we must determine where the active faults are located and how they are oriented. To accomplish this goal, we relocated ~ 45,000 earthquakes that occurred between 1980 and August 2000 in the Long Valley caldera and in the Sierra Nevada block (SNB) to its south, using the double-difference earthquake location algorithm of Waldhauser and Ellsworth (2000) and routinely determined P-phase arrival time readings from the Northern California Seismic Network (NCSN), operated by the United States Geological Survey (USGS) (Figure 2.1). The double-difference algorithm minimizes the residuals between observed and calculated travel-time differences for pairs of earthquakes at common stations by iteratively adjusting the vector difference between the hypocenters. Thus, the double-difference method minimizes effects of unknown Earth structure without the need for station corrections. The double-difference algorithm has been shown to produce sharp images of fault structure along the Hayward fault (Waldhauser and Ellsworth, 2000) and the San Andreas Fault near Parkfield (Ellsworth et al., 2000).

The dense distribution of both seismicity (Figure 2.1) and NCSN seismometers in the Long Valley area (Figure 2.2) allows us to obtain relative locations with approximately 100 m accuracy using the double-difference method and catalog arrival times. To relocate 20 years of seismicity in the Long Valley area we divided the data into spatial and temporal subsets and relocated the subsets independently. We selected a group of common reference events and included them in each subset to observe variation in their location between individual runs. The master event locations were consistent within ~200 m for all relocated subsets. Thus, we have confidence that absolute locations are fairly robust.

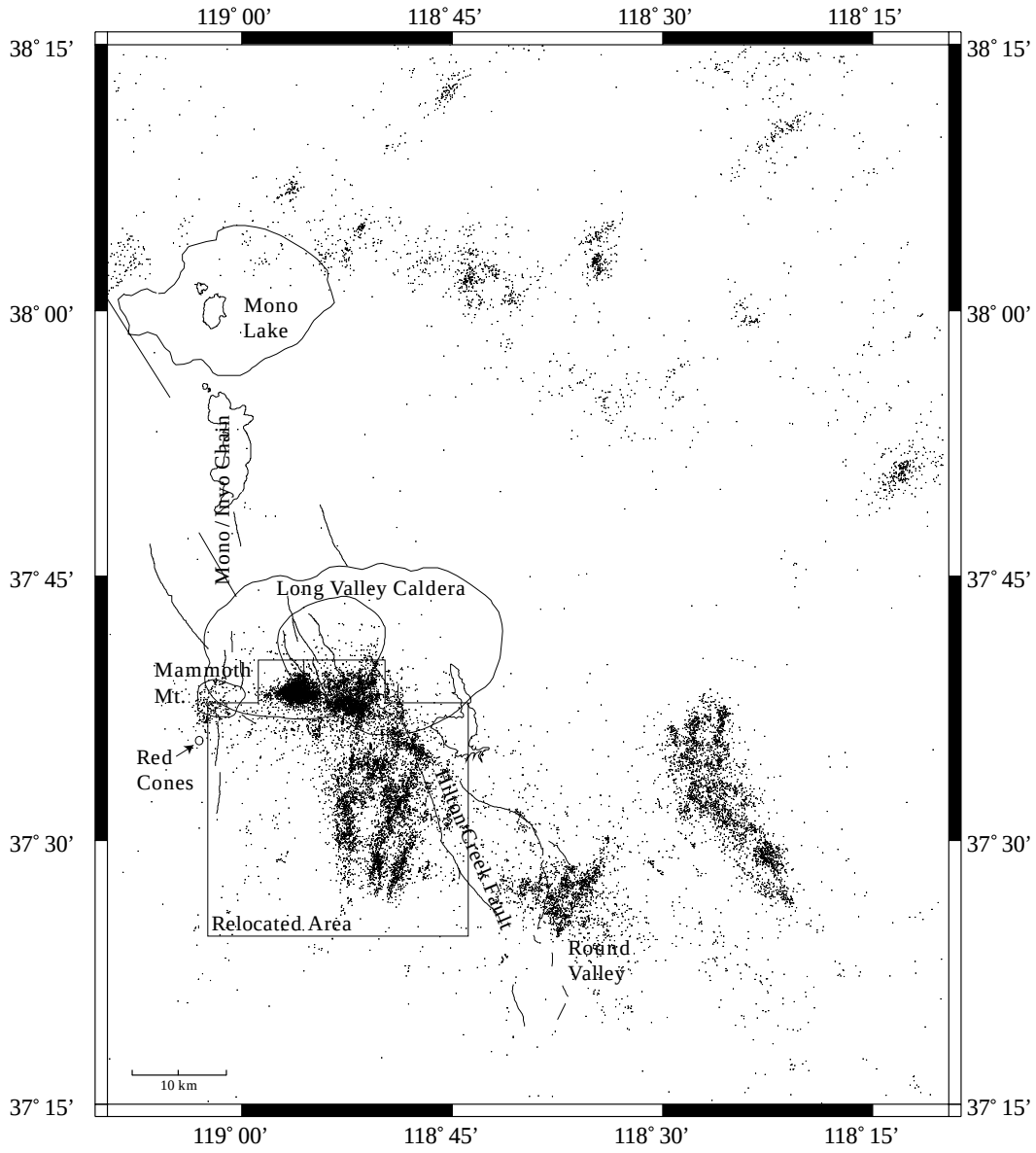

Figure 2.1- All recorded earthquakes >= **M** 2 in the greater Long Valley area between 1980 and 2000. The box encloses seismicity relocated in this chapter. Thin lines denote fault traces

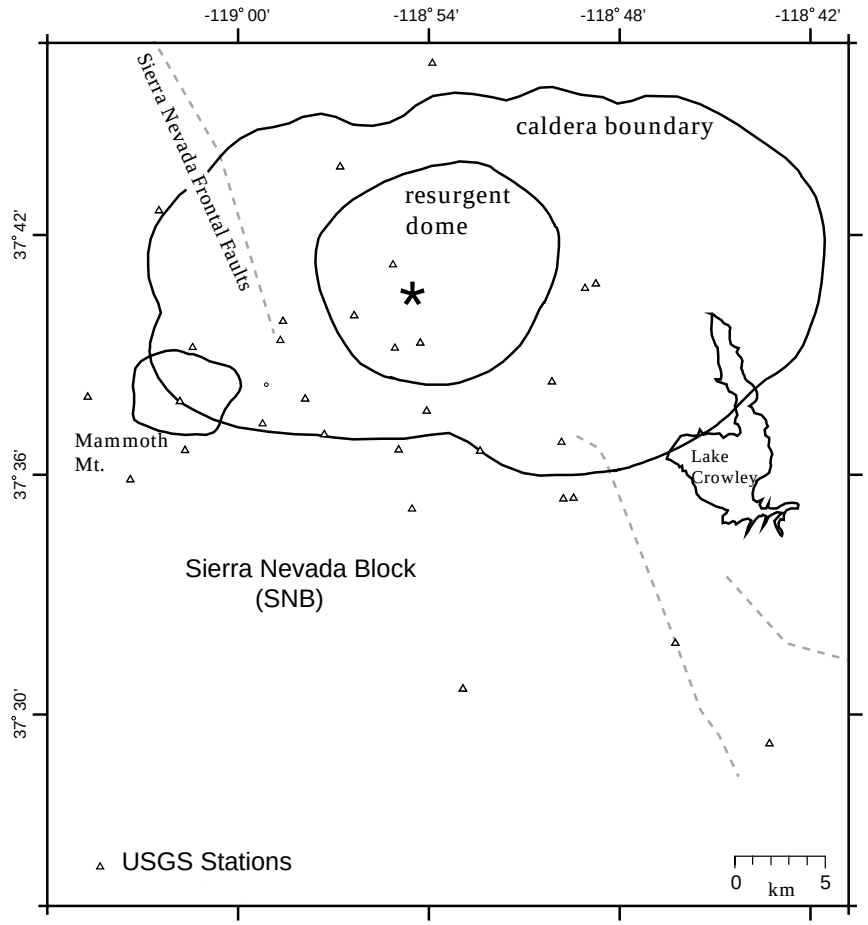

Figure 2.2 - Map of NCSN stations used for earthquake relocations.

Figure 2.3 shows a comparison of the 1997 south moat seismicity routinely located by the Northern California Earthquake Data Center (NCEDC) using *HYPO71* (Lee and Lahr, 1975) and relocated using the double-difference program, *hypoDD* (Waldhauser, 2001). The same arrival time picks were used in both cases. The double-difference locations clearly define many faults that are not discernible in the standard locations. Below we describe in some detail the family of faults revealed by our locations.

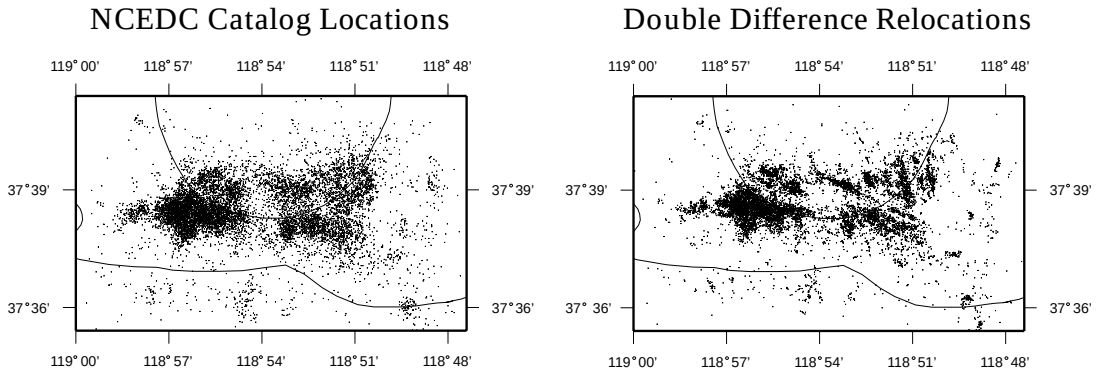

Figure 2.3 - July 1997–January 1998 Long Valley caldera seismicity before (left) and after (right) double-difference relocation (Waldhauser and Ellsworth, 2000) using P-phase catalog arrival times obtained by the Northern California Earthquake Data Center. (NCEDC)

2.3 South Moat and Resurgent Dome Seismicity

The south moat and southern resurgent dome of the caldera have jointly comprised an area of near-continuous seismicity since 1980. The relocated epicenters (> **M** 1) are shown in Figure 2.4 in two year "snapshots". Figure 2.4 illustrates that seismicity has largely occurred on the same set of faults since 1980. The patches of solid colors in this figure indicates that these structures have been activated in discrete temporal bursts of seismicity, or seismic swarms. In some cases, we observe temporal propagation of seismicity within an individual swarm along the length or width of a fault (see Section 2.6 and Chapter 5).

Seismicity in late 1997 and early 1998 was particularly intense and well recorded. Thus, we determined the orientations of active fault planes in the caldera based on seismicity during this time period. Figure 2.5 shows the 1997/1998 seismicity. The major resolvable structures are summarized in Figure 2.6 and

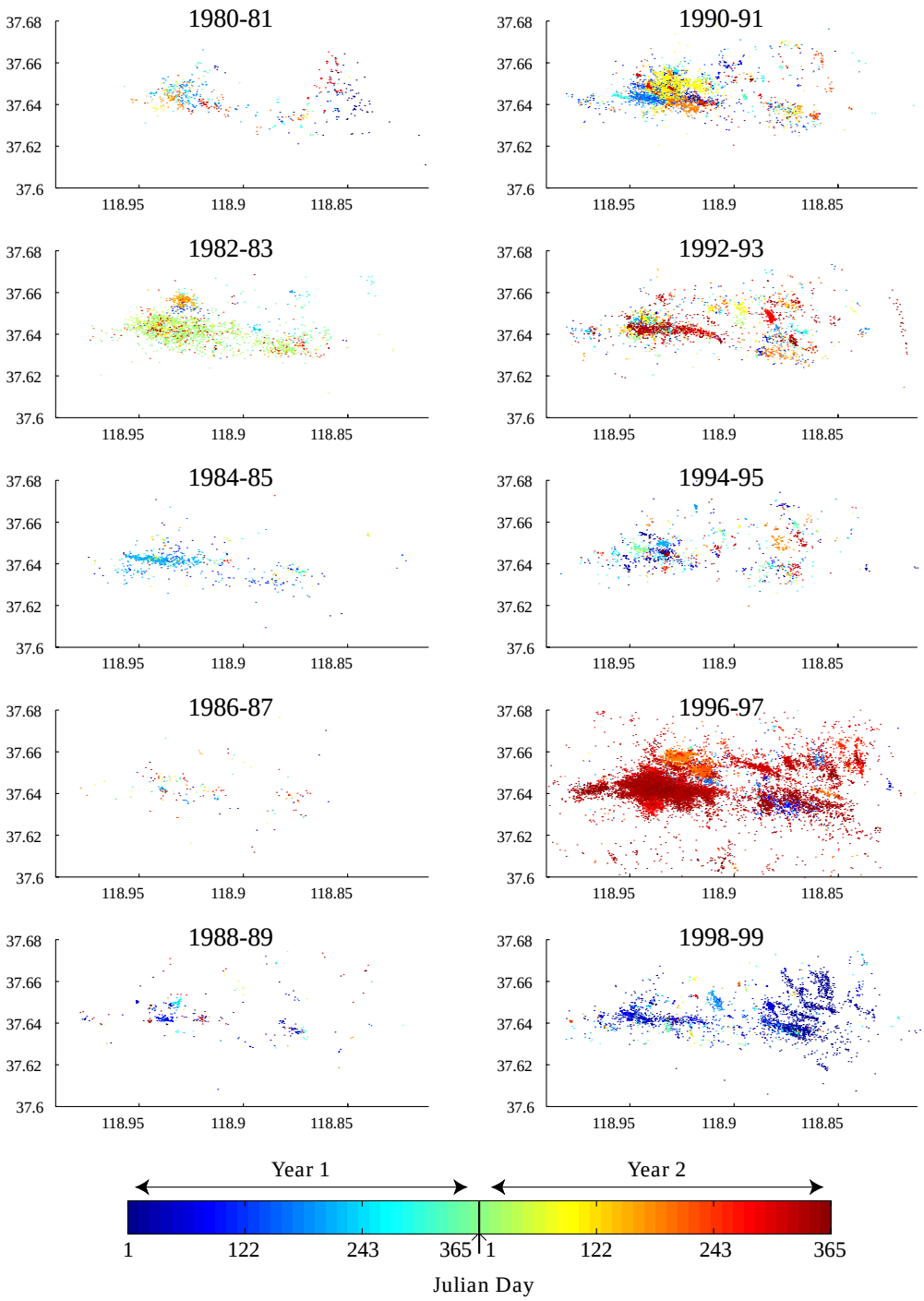

Figure 2.4 - Epicenters of relocated >= **M** 1 earthquakes in the Long Valley caldera between 1980 and 2000 in two year time spans, colored with time. Note that the catalog was not complete at **M** 1 until at least 1983.

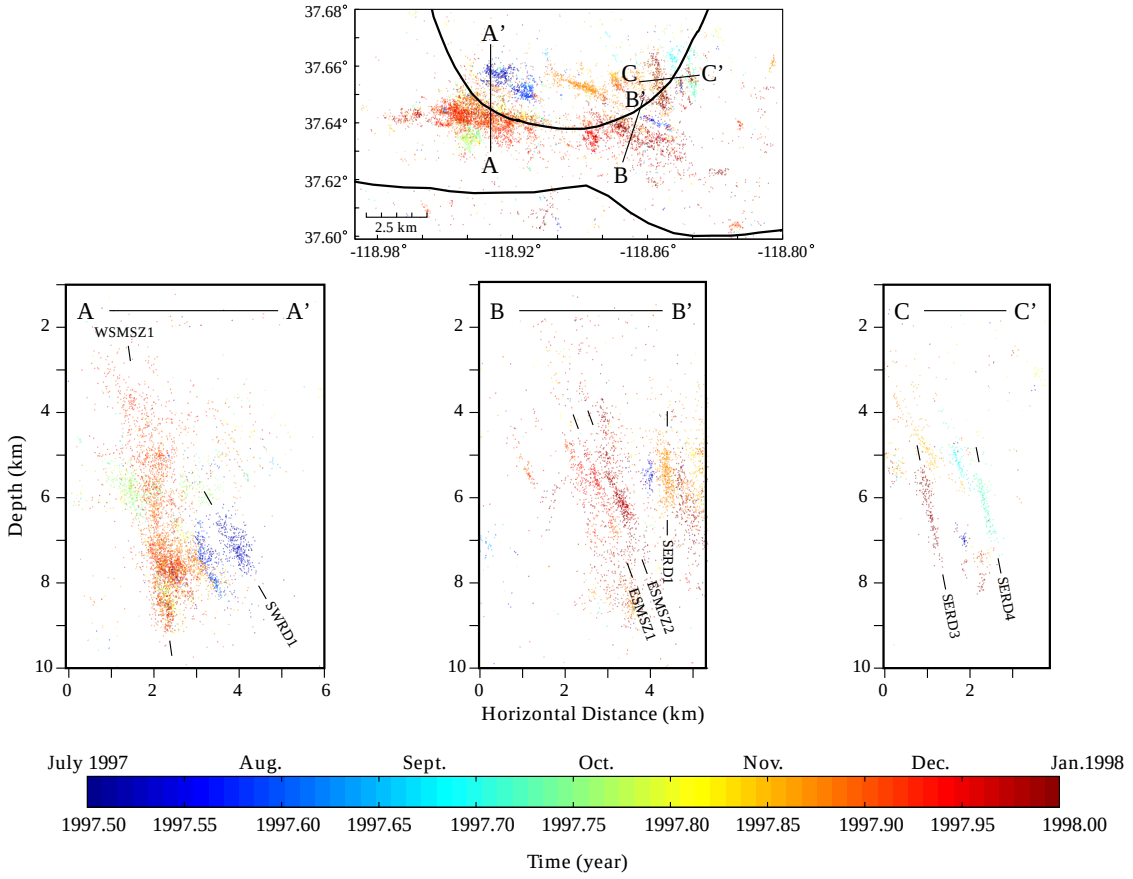

Figure 2.5 - Relocated hypocenters of July 1997–January 1998 Long Valley caldera seismicity in map view (top) and three cross sections (bottom), colored with time. See Figure 2.6 for fault labels. Cross section A-A' shows hypocenters west of -118.905; B-B' shows hypocenters east of -118.905˚ along transect line shown in map view; C-C' shows hypocenters east of -118.905˚ and north of 37.643˚ along transect line shown in map view.

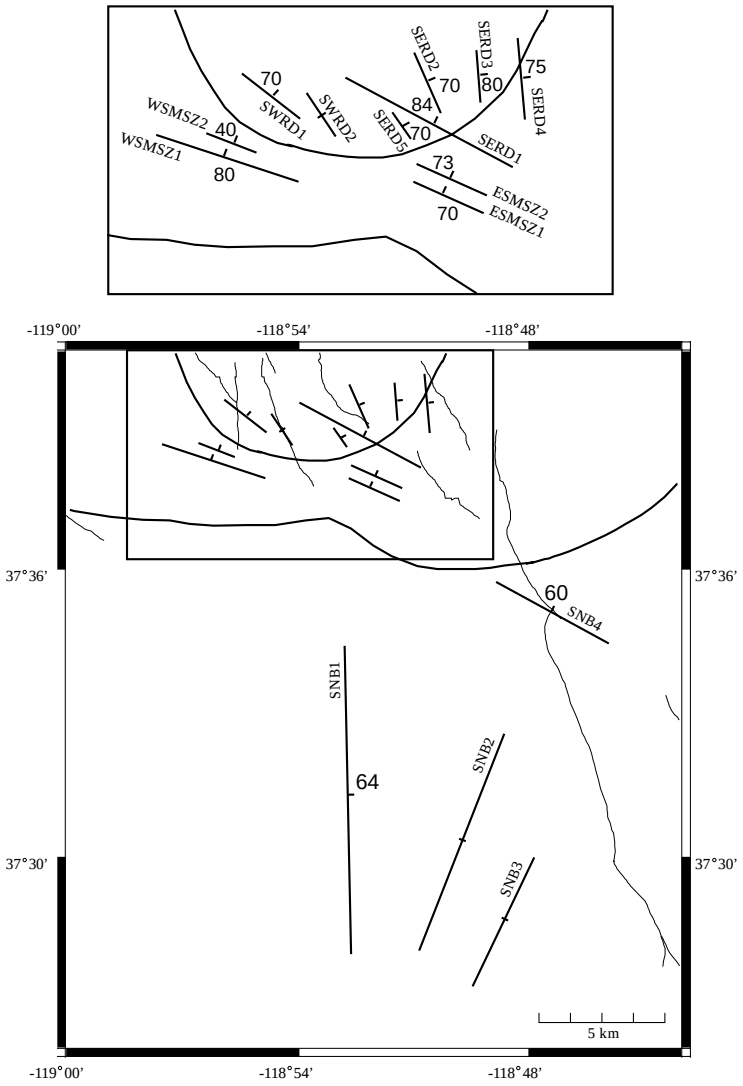

Figure 2.6 - Map of faults identified by relocated recent seismicity in the Long Valley caldera and in the Sierra Nevada basement south of the caldera (see Figure 2.8). Faults are named based on their location, where WSMSZ = west south moat seismic zone, ESMSZ = east south moat seismic zone, SERD = southeast resurgent dome area, SWRD = southwest resurgent dome area, and SNB = Sierra Nevada block. Arrows show the relative sense of slip on the faults. Thin lines are the mapped surface traces of faults (Bailey, 1989).

Table 2.1
Faults in the Long Valley Area and Their Sense of Slip

Fault	Longitude	Latitude	Depth (km)	Strike	Dip	Width (km)	Length (km)
SNB1	-118.8712	37.5198	6.5	359	64	7	12
SNB2	-118.8291	37.5052	6	21	90	6	9
SNB3	-118.8110	37.4774	6	26	90	10	5.6
SNB4	-118.7850	37.5919	7.5	298	60	3.5	5
SERD1	-118.8729	37.6475	5.5	298	84	2	5.3
SERD2	-118.8712	37.6576	4.8	336	70	1.6	1.84
SERD3	-118.8558	37.6584	6	355	80	2	1.5
SERD4	-118.8406	37.6580	6.3	354	75	2.6	2.3
SERD5	-118.8804	37.6469	8	326	70	1	1
ESMSZ1	-118.8639	37.6337	7	294	70	4.4	2.3
ESMSZ2	-118.8648	37.6347	6	294	73	2.1	2.3
WSMSZ1	-118.9354	37.6422	6	288	80	6.1	4.2
WSMSZ2	-118.9331	37.6475	7.6	326	70	1.1	1
SWRD1	-118.9210	37.6559	7.5	307	70	2.1	2.1
SWRD2	-118.9077	37.6487	8	327	90	2	1.5

Table 2.1 and are discussed further below. We only consider an imaged feature to be a fault if a cluster of earthquakes clearly defines a three-dimensional fault plane. A line of seismicity, for example, is not considered a fault plane although it may rupture one. Therefore, the faults shown in Figure 2.6 and described in Table 2.1 are only the most active in the south moat and Sierra Nevada block. There are many other smaller faults which are currently active as well, yet do not satisfy our criteria.

In recent seismic swarms, the largest seismic moment release in the caldera has occurred consistently in the western portion of the south moat. We refer to this region as the western lobe of the south moat seismic zone (WSMSZ) following Hill et al. (in press). The WSMSZ is dominated by WSMSZ1, a fault zone

oriented ~N72W/80NE. WMSZ1 appears to have a complex structure that is best described by two north-dipping segments at the top and base of the zone with a near vertical segment between them (Figure 2.7). This feature is the southernmost active structure within the caldera (Figures 2.5 and 2.6), and may be related to the caldera ring fracture system (Bailey, 1989).

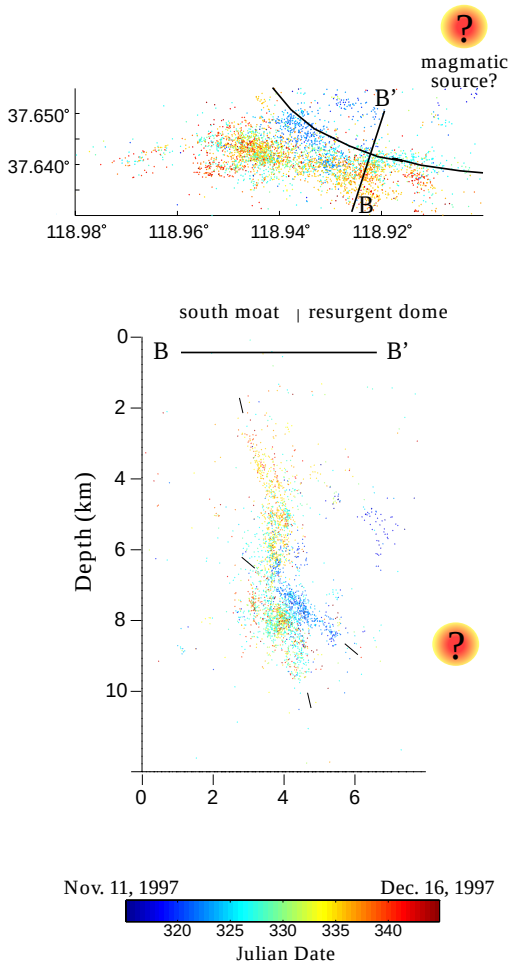

Figure 2.7 - Seismicity in the west south moat seismic zone fault 1 (WSMSZ1) in November and December 1997, colored with time. Upper panel is map view. Lower panel is a vertical cross section oriented N17E–S17W.

Seismic swarms have occurred repeatedly in WSMSZ1 since 1980 (Figure 2.4). Unlike most of the other faults we have identified in the caldera, seismicity in this fault zone does not lie along a simple plane. Rather, the WSMSZ1 appears to be a 1 kilometer-wide zone of highly fractured crust. We confirmed that this fault zone width is real and not location error by observing travel time differences in the Long Valley Exploratory Well (LVEW) borehole data (see Chapter 4 for more information on LVEW data) in earthquakes whose locations span the width of the WSMSZ1.

To improve locations further in the WSMSZ area and search for smaller subfaults, we relocated 671 earthquakes which occurred in the area on November 22, 1997, incorporating well-constrained first motion picks from the 2 km deep LVEW station in the relocations. Although the borehole data improved locations significantly, no distinct subfaults were discernible in the hypocenter locations. However, as Chapter 5 explains, it is likely that the WSMSZ1 is a complex system of interconnected faults that are repeatedly reactivated by fluids or transient high pressure pulses emanating from magmatic activity below the south moat or resurgent dome of the caldera.

Subparallel to WSMSZ1, there are at least three smaller faults in the western lobe of the south moat seismic zone and the southwestern portion of the resurgent dome (SWRD following Hill et al., in press), which have been active in each of the major seismic episodes in the caldera (1980, 1982/83, 1990/91, 1996, 1997/98) (Figure 2.4). These faults, including WSMSZ2 and SWRD1, appear to fan outward and northward from the lower segment of WSMSZ1 (Figures 2.4 and 2.7). They are active over a smaller depth range (6.5 to 8 km depth) than WSMSZ1 (3 to 9 km depth) and dip more shallowly to the northeast (~50˚) than WSMSZ1 (Figure 2.5, A-A'). These faults may form connecting pathways between WSMSZ1 and the inflating magma chamber beneath the resurgent dome, whose

existence is suggested by deformation data (Langbein, 1989; Langbein et al., 1995; Marshall et al., 1997; Battaglia et al., 1999).

Seismicity in the south moat continues into the eastern lobe of the south moat seismic zone (ESMSZ) across an apparent 2 km-wide seismic gap in the central south moat, although the distribution of seismic moment release indicates that this eastern extension of the fault zone is much less active than its western counterpart (Figure 2.5). Like the WSMSZ, the ESMSZ is comprised of at least two subparallel faults striking N66W and dipping roughly 70˚ N (faults ESMSZ1, ESMSZ2) (Figure 2.5, B-B'). However, unlike the WSMSZ, the ESMSZ can be resolved as a suite of well-defined, discrete fault planes. As in the WSMSZ, the ESMSZ1 forms the southern border of seismicity in the south moat of the caldera and may be related to the ring fracture system.

North of the ESMSZ, relocated hypocenters define many smaller, more northerly-striking faults in the southeastern resurgent dome. Interestingly, a more complex fabric of discrete faults is visible in the southeastern resurgent dome than in the southwestern resurgent dome (Figures 2.5 and 2.6). A major fault in the south eastern resurgent dome area, SERD1, is a near-vertical fault striking N60W. North of SERD1, fault orientations rotate to a more north-south orientation (SERD2, SERD3, SERD4) (Figure 2.6).

The western and eastern lobes of the south moat seismic zone dominate each seismic episode in the south moat, but there is no evidence for surface rupture of the major east-west trending faults in these fault zones (David Hill, personal communication), presumably because they are covered with a thick layer of poorly-consolidated sediments inter-layered with lava flows (Bailey, 1989). However, many of the smaller, more northerly-striking faults in the south moat and southern resurgent dome of the caldera have roughly the same orientation as mapped surface faults (Figure 2.6) (Bailey, 1989). Specifically, the faults in the

south eastern resurgent dome and SWRD2 may be related to the resurgent dome's medial graben or the northern extension of the Hilton Creek fault, which splinters into multiple segments within the caldera (Bailey, 1989).

Overall, the base of the seismogenic zone appears to be more shallow inside the caldera (~9 km depth), than in the Sierra Nevada block immediately south of the caldera, where seismicity extends to ~16 km depth. This may result from an unusually high temperature gradient inside the caldera due to magmatic activity. Alternatively, it may reflect the transition between the relatively thin crust Basin and Range province at Long Valley and the thick, cold crust of the Sierra Nevada batholith, south of Long Valley.

2.4 Sierra Nevada Seismicity

The Sierra Nevada block (SNB), which is directly south of Long Valley, has a more simple fault structure than the caldera. Figure 2.8 shows our locations of SNB seismicity, while Figure 2.6 and Table 2.1 summarize the major identifiable features. In general, the maximum depth of the seismogenic zone in the SNB increases toward the east (Figure 2.8, F-F'). There are four primary faults in this region and many minor faults.

Fault SNB1, which forms the western boundary of seismicity, is a north-striking, east-dipping fault (Figure 2.8, D-D') whose dip shallows slightly toward the north and possibly with depth. In the region immediately north of SNB1, seismicity is intense, yet diffuse, with no clearly discernible planes. Thus, this region may have a complex fault structure. Faults SNB2 (N28E / ~90) and SNB3 (N28E / ~90) are two subvertical structures (Figures 2.6 and 2.8, E–E') which dominate seismicity in the hanging wall of SNB1. However, like SNB1, SNB2 and SNB3 may not be simple planes. Figure 2.8 shows that SNB2 may actually be composed of two parallel structures (map view), while SNB3 may be a pair of en

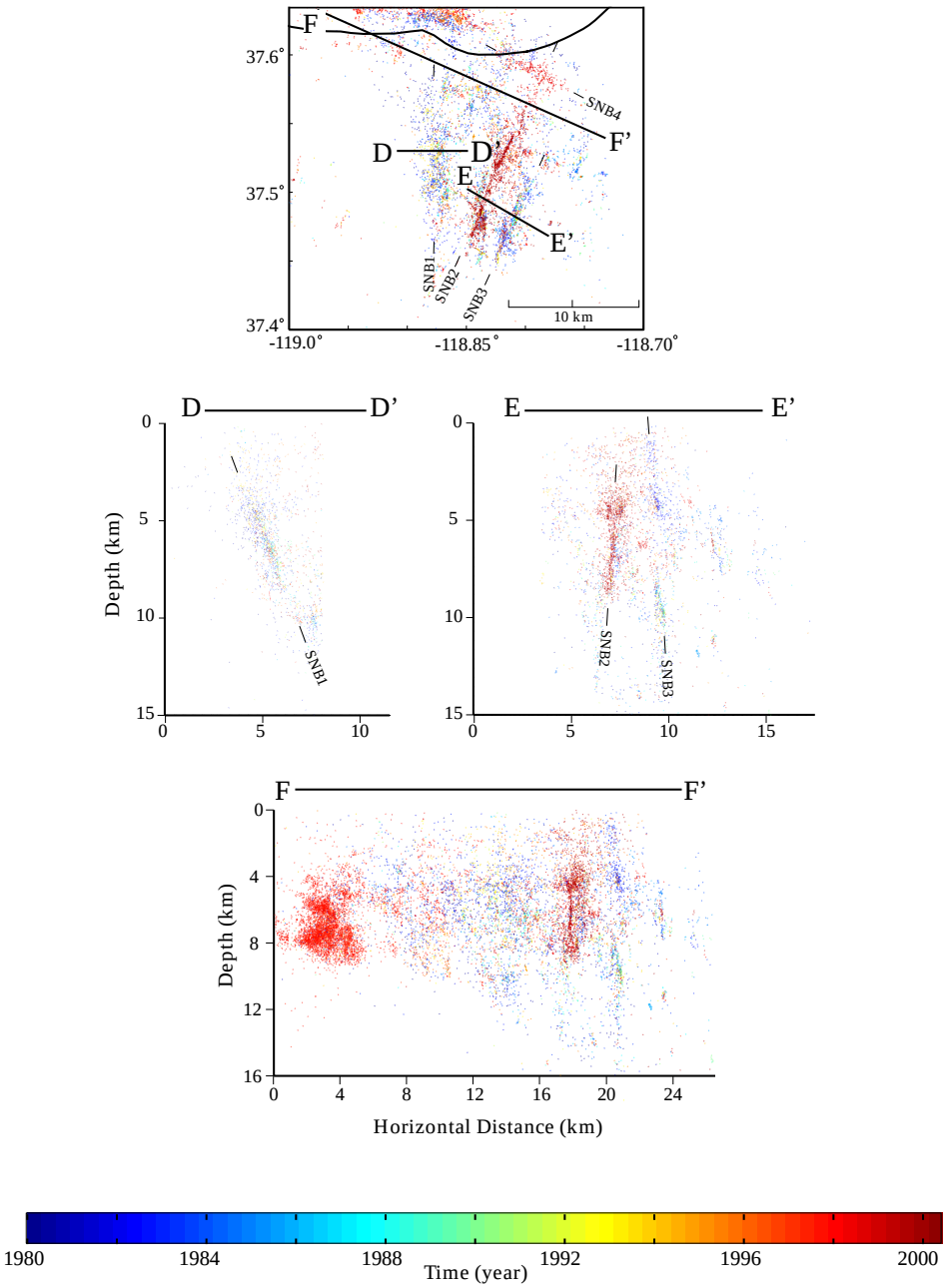

Figure 2.8 - Locations of > **M** 2.5 earthquakes in the Sierra Nevada Block between 1980 and August 2000 in map view (top) and three cross sections (bottom), colored with time. See Figure 6 for fault labels. Cross section D-D' shows hypocenters south of 37.55 and west of -118.85; E-E' shows hypocenters south of 37.57 and east of -118.85; F-F' shows all relocated hypocenters.

echelon planes rather than one continuous plane with depth (E-E'). Background seismicity in the SNB occurs predominately on small vertical planes parallel to SNB2 and SNB3, the easternmost of which are visible in Figure 2.8, but small crosscutting planes also appear to exist in the area. These more subtle features are visible only in stereographic projection (Figure 2.9). Their orientations are not constrained well enough by seismicity locations to be defined in Table 2.1. SNB4 is a N70W /60˚NE feature that generally lies along the same trend as faults in the west and east south moat seismic zones. Although SNB4 may have slipped in the **M** 6 1980 earthquake sequence, this fault was otherwise seismically quiet after 1980 until 1997.

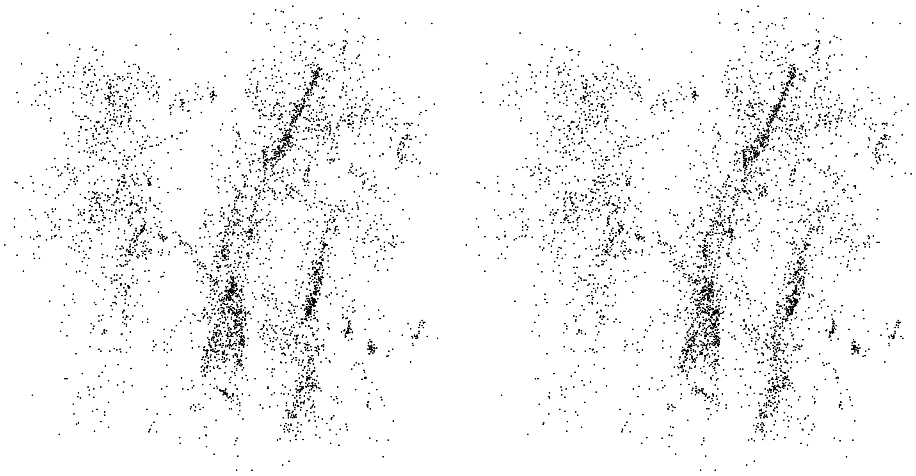

Figure 2.9 - Stereoscopic plot of relocated seismicity, **M** >=2.5.

2.5 M 5+ Earthquakes in the Long Valley Area, 1980-2000

Figure 2.10 and Table 2.2 give the double difference locations for all earthquakes of **M** 5 or larger in the Long Valley area since 1980, numbered chronologically. In order to understand these events better and to understand how seismic deformation is distributed in the caldera region, we have attempted to identify the fault planes that accommodated slip in these earthquakes based on their locations and focal plane solutions. Most of the **M** 5+ events are located on one of the faults defined by seismicity. In these cases, we assume that the nearby faults were the earthquakes' rupture planes if a well constrained double-couple focal mechanism supports this inference or if the focal mechanism is not known (Table 2.2). The focal plane solutions for earthquakes that have well-defined first motion mechanisms or that have complete moment tensor solutions are shown in Figure 2.10. In the cases in which the earthquakes are not located along known faults, we have not listed any associated planes in Table 2.2.

Based on these locations, all of the SNB faults shown in Figure 2.6 and the WSMSZ and ESMSZ have probably ruptured since 1980 in moderate-sized earthquakes. However, available seismicity data does not seem to illuminate all of the major faults in the area, based on the locations of earthquakes #10 (September 1981) and #15 (July 1998). These two earthquakes have reliable focal mechanism solutions that are inconsistent with nearby planes defined by microseismicity. Thus these earthquakes must have occurred on unmapped planes. Seismic slip is truly distributed throughout this region, as the microseismicity suggests.

Since many of the **M** 5+ earthquakes occurred in intense swarms, the first motion focal mechanisms are often poorly defined. Even though the focal mechanisms for the 1980 **M** 6 earthquakes (events #1, #3, and #8) are debated and may be non-double-couple (NDC) events (Given et al., 1982; Wallace et al., 1982; Julian and Sipkin, 1985; Wallace, 1985), we attempt to associate these earthquakes with

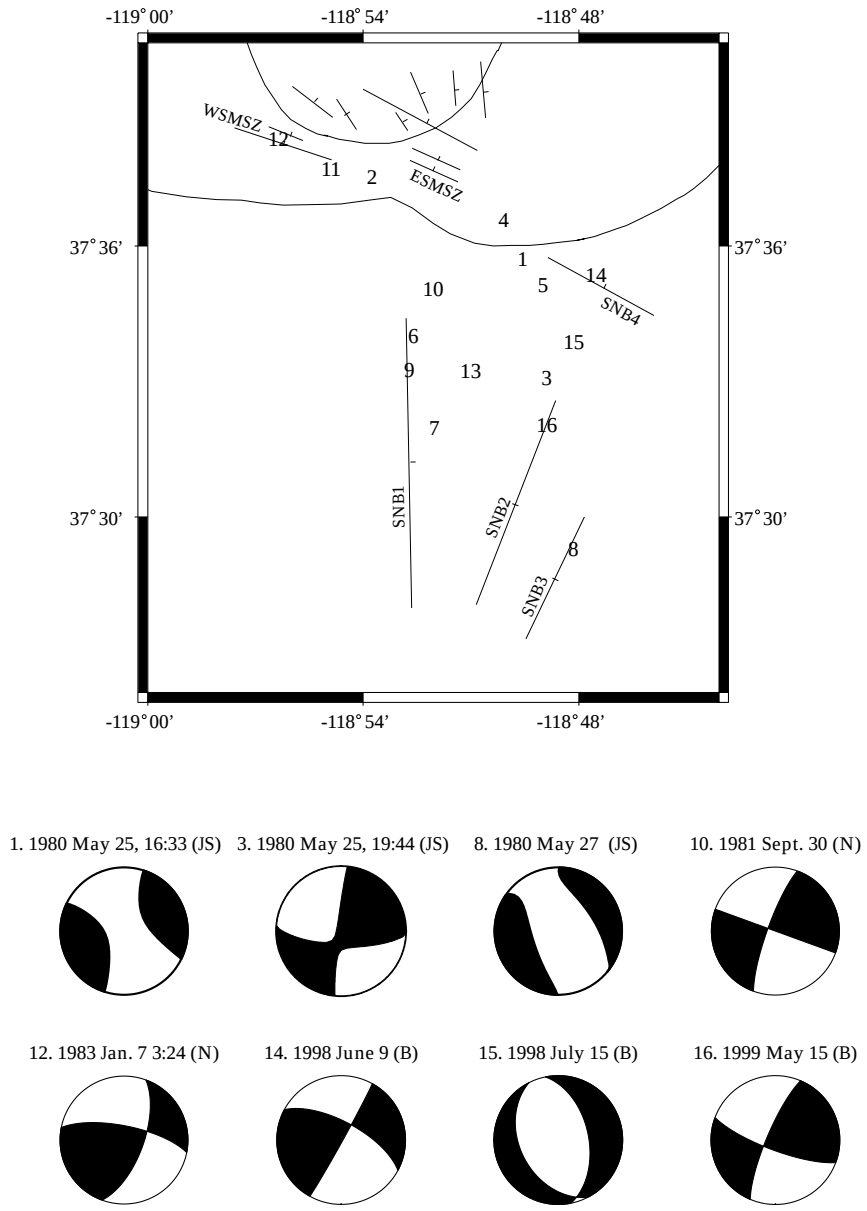

Figure 2.10 - Map of hypocenters for all earthquakes > = **M** 5 in the Long Valley area, 1980–2000, numbered chronologically. Focal plane solutions for the well-constrained events are shown below. Sources of focal plane solutions: JS–Julian and Sipkin (1985); N–Northern California Earthquake Data Center; B–Univ. of California, Berkeley Seismological Laboratory. See Figure 2.6 for fault labels.

Table 2.2
M 5+ Long Valley Region Earthquakes, 1980 - 2000

	Date	Hr: Min	**M**	Latitude	Longitude	Depth (km)	Associated Planes
1*	1980 May 25	16:33	6.10	37.59524	-118.82621	8.214	SNB4
2	1980 May 25	16:49	6.00	37.62577	-118.89601	4.833	WSMSZ/ ESMSZ
3*	1980 May 25	19:44	6.10	37.55127	-118.81492	12.866	SNB2
4	1980 May 25	20:35	5.70	37.60962	-118.83481	4.627	-
5	1980 May 25	20:59	5.00	37.58573	-118.81657	7.642	-
6	1980 May 26	12:24	5.10	37.56686	-118.87672	7.035	SNB1
7	1980 May 26	18:57	5.70	37.53278	-118.86699	6.773	SNB1
8*	1980 May 27	14:50	6.20	37.48816	-118.80260	14.380	SNB3
9	1980 Aug. 1	16:38	5.40	37.55440	-118.87867	7.287	SNB1
10*	1981 Sept. 30	11:53	5.90	37.58434	-118.86764	6.410	-
11	1983 Jan. 7	1:38	5.40	37.62841	-118.91474	4.365	WSMSZ
12	1983 Jan. 7	3:24	5.30	37.63956	-118.93922	7.153	WSMSZ
13	1983 July 3	18:40	5.30	37.55373	-118.85021	11.095	SNB1
14	1998 June 9	5:24	5.13	37.58946	-118.79198	8.252	SNB4
15	1998 July 15	4:53	5.11	37.56453	-118.80235	7.604	-
16	1999 May 15	13:22	5.60	37.53404	-118.81471	7.062	SNB2

* Events with well constrained focal mechanisms shown in Figure 8.

known fault planes. The NDC nature of these earthquakes could result from simultaneous shear slip and magmatically driven fluid injection or simultaneous slip on multiple rupture planes, as discussed in Julian and Sipkin (1985). If the NDC nature results from complex slip on multiple rupture planes, the moment tensors obtained for earthquake #1 may reflect simultaneous strike-slip motion on plane SNB4 and normal motion on a fault orientated like SNB1, as shown in Figure 2.11. Similarly, the mechanism for earthquake #8 may result from simultaneous strike-slip motion on SNB3 and normal motion on a second fault oriented parallel to SNB1. Because the Long Valley caldera is a strike-slip / normal faulting stress regime in which the maximum horizontal stress and vertical stress are approximately equal (see Chapter 3), this slip configuration is plausible. The

earthquakes nucleated near the base of the seismogenic zone and might have conceivably ruptured upward along two planes simultaneously. This hypothesis is supported by the aftershock distribution for these two earthquakes because both earthquakes #1 and #8 produced aftershocks on fault SNB1.

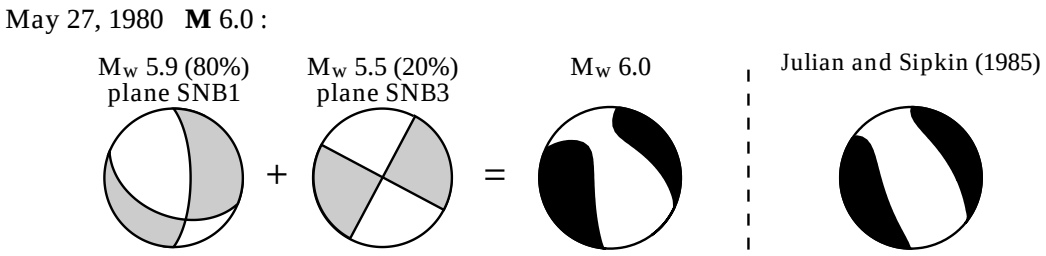

Figure 2.11 - Possible explanation for the May 27, 1980 non-double-couple focal mechanism. Focal mechanism resulting from moment tensor sums of simultaneous shear faulting on two planes shown on left. Observed focal mechanism shown on right.

2.6 Mammoth Mountain Seismicity

Between 1980 and mid-1989 Mammoth Mountain was seismically very quiet with only diffuse background seismicity occurring (Figure 2.12). However, in mid 1989 a seismic swarm began under Mammoth Mountain that was unlike any other swarm yet observed in the caldera region (see Hill et al., 1990 for review). The locations of earthquakes in this swarm are shown in Figure 2.13.

The 1989 swarm began with seismicity at 7–9 km depth in a NNE trending keel-like structure beneath the center of Mammoth Mountain. This feature was seismically active from late May until early July, and has been interpreted as an intruding dike (Hill et al., 1990). After mid-July, seismicity moved upward and was concentrated between 6 km to 1 km depth, primarily on two half-ring-like features (Figure 2.13 upper panel). The center of these two rings was virtually aseismic. If Hill et al.'s (1990) hypothesis that the deep keel of seismicity represents an intruding dike is correct, the overlying rings of seismicity may result from stress concentrations formed above a pocket of magma due (Nettles and Ekstrom, 1998). This interpretation is supported by an observed rotation of focal mechanism nodal planes about Mammoth Mountain (Foulger et al., in preparation).

Between the 1989 sequence and February 1999, earthquakes occurred beneath Mammoth Mountain at very low rates on many small faults of widely varying orientations. In February 1999, a seismic swarm occurred along a northwest-striking, steeply southwest dipping fault beneath the southeast flank of Mammoth Mountain (Figures 2.12 and 2.14). Seismicity propagated a distance of 1 km up this feature in ~ 9 hours (Figures 2.14). The migration of seismicity upward along this fault implies that this activity may be magmatic in origin (see Chapter 5).

In summary, because Mammoth Mountain swarms are not coeval with caldera swarms, earthquakes under Mammoth Mountain seem to be driven by different processes from earthquakes in the south moat and in the Sierra Nevada block. Hypocenter locations suggest that seismicity under Mammoth Mountain is directly reflecting the local movement of magma.

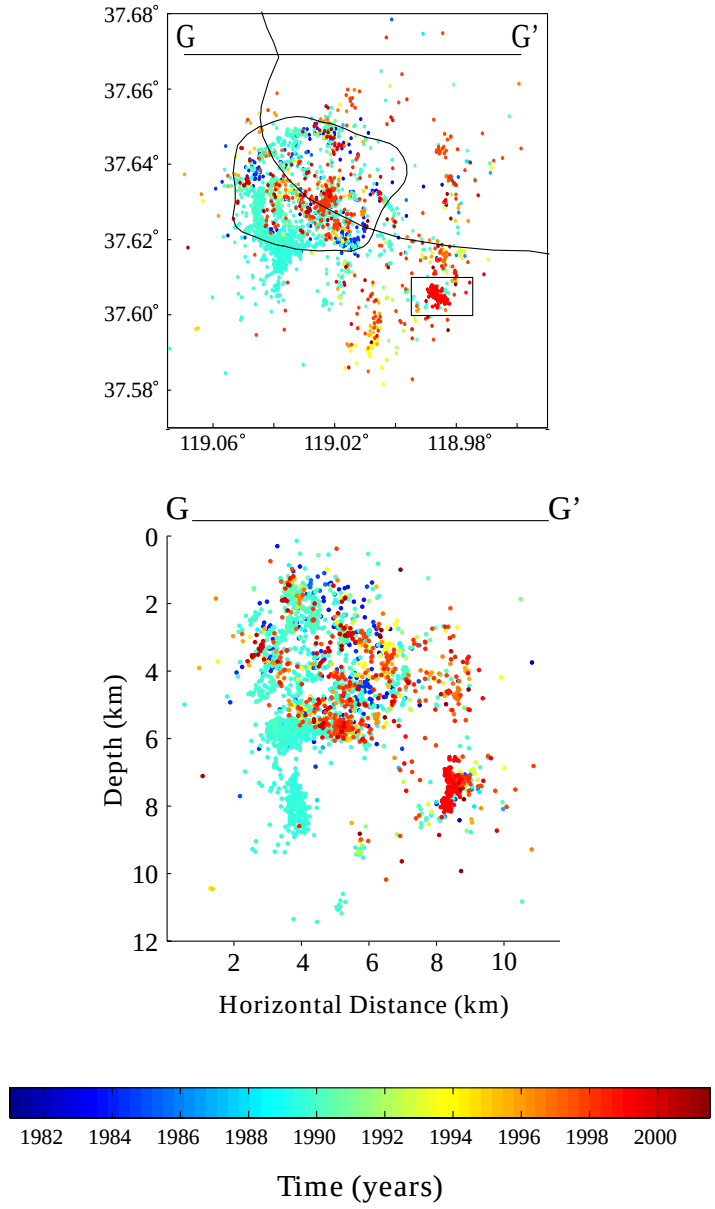

Figure 2.12 - 1980–2001 Mammoth Mountain seismicity in map view (upper) and E–W cross section (lower). Box south of caldera indicates area of Figure 2.14.

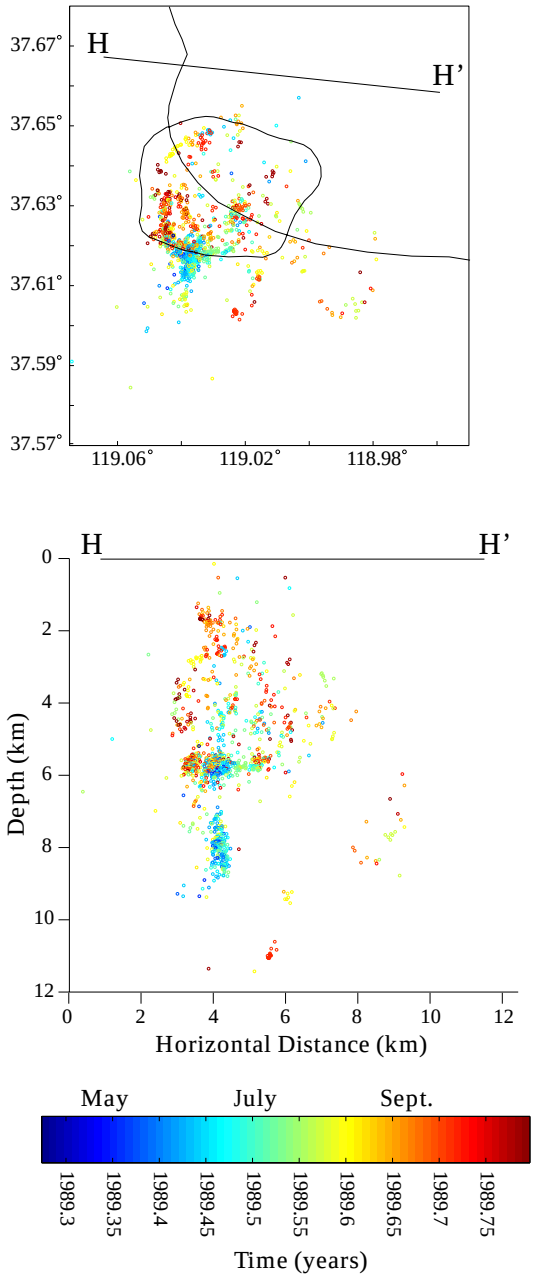

Figure 2.13 - 1989 Mammoth Mountain seismicity in map view (upper) and E07S–W07N cross section (lower), color-coded in time.

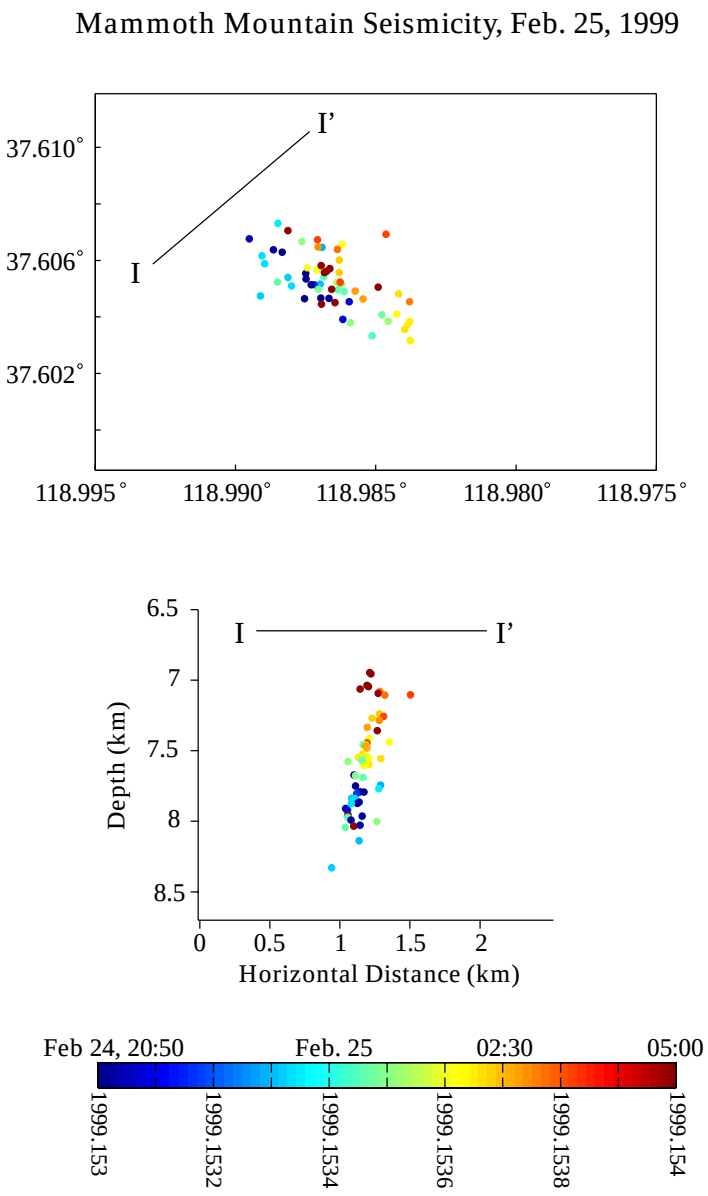

Figure 2.14 - February 25, 1999 Mammoth Mountain seismicity in map view (upper) and N53E–S53W cross section (lower), color coded in time. Area of plot shown in Figure 2.12.

2.7 Summary

High-resolution hypocenter locations obtained using a double-difference method (Waldhauser and Ellsworth, 2000) reveal an intricate fabric of faults in the south moat and southern resurgent dome of the caldera that tend to rupture in brief, intense seismic swarms. Complex fault zones in the south moat of the caldera have accommodated most of the recent seismic moment in the caldera. These fault zones form the southern boundary of intracaldera seismicity and consist of several subparallel faults, oriented roughly N70W/80NE. Many smaller faults with more northerly strikes (maximum strike of N06W) are active to the north of the main south moat fault zone.

Seismicity in the Sierra Nevada basement south of the caldera is largely confined to an east-dipping north-south striking fault and to faults within its hanging wall. This active east-dipping fault is located ~10 km inside the Sierra Nevada from the major range-bounding Hilton Creek fault. Two N28E-striking vertical faults dominate hanging wall seismicity.

Seismicity beneath Mammoth Mountain in 1989 was concentrated on a deep (~8 km depth) keel-like structure and two overlying ringlike features. The shape of these structures suggests that seismicity beneath Mammoth Mountain is controlled directly by the local intrusion of magma.

Acknowledgements

We would like to thank Eva Zanzerkia, David Schaff, and Felix Waldhauser for assistance in relocating the earthquakes.

Chapter 3

LONG VALLEY AREA KINEMATICS AND A POSSIBLE DRIVING SCENARIO BASED ON FOCAL MECHANISM STRESS INVERSIONS

A shorter version of this chapter combined with Chapter 2 will be published with Bill Ellsworth, Mark Zoback, and Felix Waldhauser as coauthors in the *Journal of Geophysical Research*.

3.1 Abstract

In order to understand better the stresses driving seismicity in the vicinity of the Long Valley caldera, we performed a detailed suite of stress inversions using focal mechanisms constrained by 50 or more first motions. This analysis reveals that the least compressive stress direction systematically rotates across the studied region, from NE–SW in the caldera's south moat, to WNW–ESE in Round Valley, 25 km to the southeast. Because WNW–ESE extension is characteristic of the western boundary of the Basin and Range province, stresses within the caldera appear to be locally perturbed. This stress perturbation does not seem to result from magma chamber inflation but may be related to the significant (~20 km) left-step in the locus of extension along the Sierra Nevada/Basin and Range province boundary. This implies that regional-scale tectonic processes are driving seismic deformation in the Long Valley caldera.

3.2 Introduction

Although high seismicity and deformation rates have led to extensive seismic and geodetic monitoring in the Long Valley caldera, the mechanics of the interaction between Basin and Range tectonics, the comparatively stable Sierra Nevada block (SNB), and the caldera magmatic system remain enigmatic. One clue towards understanding deformation in the Long Valley area is the existence of a local stress perturbation. Previous studies have shown that the minimum compressive horizontal stress (Sh_{MIN}) in the resurgent dome of the caldera is oriented NE–SW (Vetter and Ryall, 1983; Moos and Zoback, 1993), in marked contrast to the WNW–ESE to E–W Sh_{MIN} direction characteristic of the western Basin and Range province (Zoback, 1989; Bellier and Zoback, 1995), the west moat and Mammoth Mountain areas (Hill et al., 1990; Moos and Zoback, 1993), and the Mono-Inyo volcanic chain (Bursik and Sieh, 1989). Magmatically influenced earthquakes (Dreger et al., 2000) (see Chapter 5) and inflation of the caldera's resurgent dome (Savage and Cockerham, 1984; Langbein, 1989; Langbein et al., 1995; Marshall et al., 1997; Battaglia et al., 1999) indicate that a magmatic system at depth is influencing deformation in the Long Valley area, but the exact nature of these processes, their interaction with regional tectonics, and their relationship to the observed stress perturbation are not understood.

To help address these issues, we performed a series of focal mechanism stress inversions to map spatial stress variations. By examining focal mechanisms and combining the precisely-imaged fault orientations described in Chapter 2 with knowledge of the stress field, we can accurately describe motion along faults with respect to one another, yielding insight into the kinematics of this complex system. Based on this analysis, we suggest a simple, tectonically driven explanation for the observed stress perturbation in the south moat of the caldera.

3.3 Focal Mechanism Stress Inversions

To constrain the stresses driving slip on faults in the Long Valley area, we performed focal mechanism stress inversions following both Gephart and Forsyth (1984) and Michael (1987). We used first motion focal mechanisms determined by the Northern California Earthquake Data Center (NCEDC) with *FPFIT* (Reasenberg and Oppenheimer, 1985). Focal mechanism stress inversion algorithms are based upon the premise that faults slip in the direction of maximum resolved shear traction on the fault plane. Additionally, estimating the stress field using earthquake focal mechanisms requires three assumptions, namely (see Gephart, 1990b, for discussion), (1) the focal mechanisms are accurate representations of the earthquake source, (2) stresses are homogeneous in the volume containing the selected focal mechanisms, (3) the focal mechanisms represent a variety of faulting orientations, because one cannot deduce reliable stress orientations from either a single focal mechanism or an arbitrary number of similar focal mechanisms (McKenzie, 1969).

In attempt to satisfy the first assumption, we inverted only those mechanisms which are constrained by at least 50 first motions and have unique solutions. Most focal mechanisms in the Long Valley area that fit this description are very well constrained. In attempt to minimize problems associated with the second assumption, we limit each inversion to an area with dimensions of 5 km x 5 km (Figure 3.1). Finally, in attempt to satisfy the third assumption, we only inverted areas (shown in Figure 3.1) in which at least 30 earthquakes occurred between 1980 and 2000. Figure 3.1 shows the areas in which we determined the stress, the epicenters of the earthquakes used in the inversions, stereographic projections of the corresponding P and T moment tensor axes for the focal mechanisms, and stereographic projections illustrating the confidence intervals of our results.

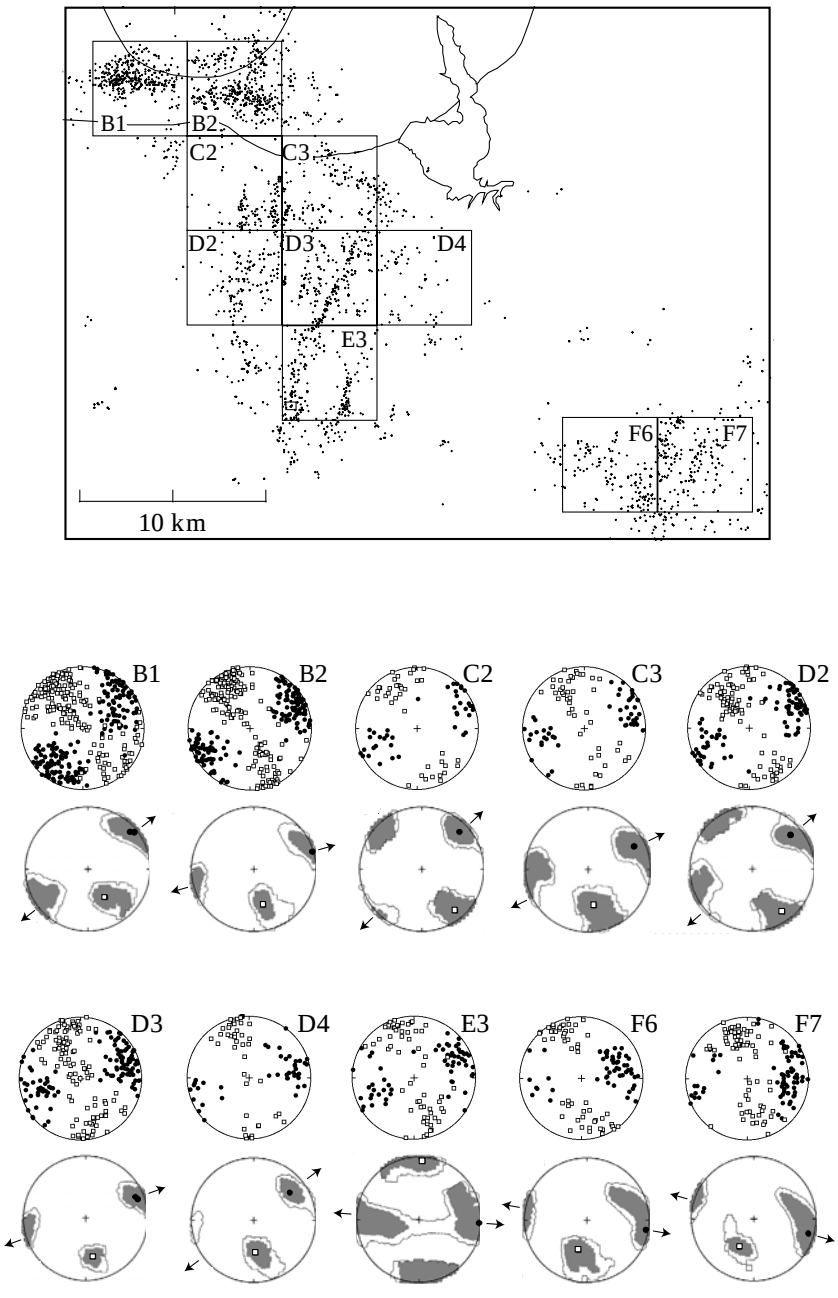

Figure 3.1 - Map of earthquakes used in focal mechanism stress inversions using FMSI (Gephart, 1990). Inverted regions are shown in numbered boxes. For each box, P / T axes of the inverted earthquakes are shown in lower hemisphere projections (T axes = black circles, P axes = white squares) with the corresponding stress axes results shown below the P / T plots (S3 = black circle, S1 = white square). The 68% (white with black outline) and 95 % (shaded) confidence regions are shaded. Stereographic plots were constructed using FMSI software (Gephart, 1990).

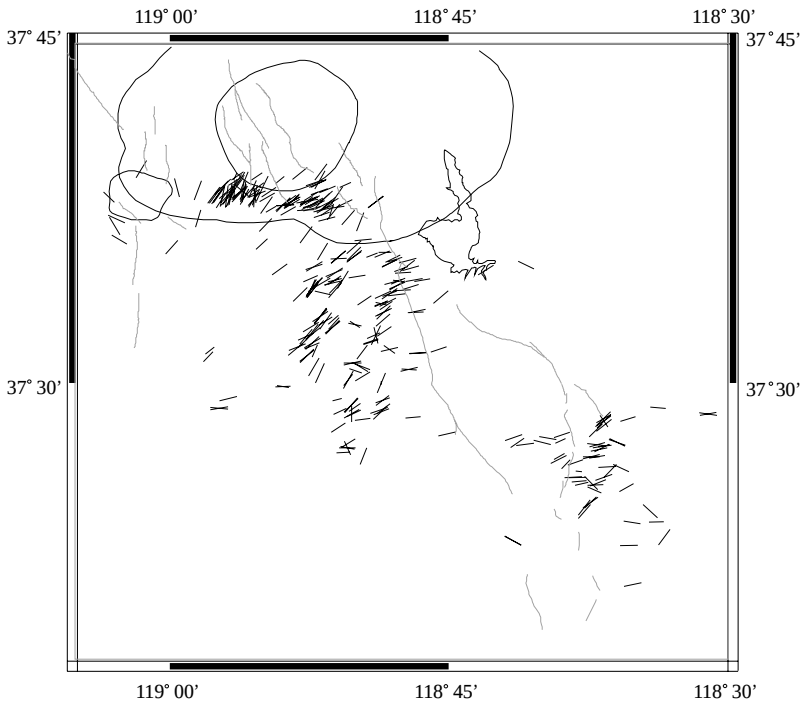

Figure 3.2 - T axes for all earthquakes with more than 75 first motion readings.

Figure 3.2 shows the directions of T axes from focal mechanisms in the Long Valley area to illustrate how the data vary spatially within the region.

We find that the Gephart and Forsyth (1984) method and the Michael (1987) method give results that generally agree, although the uncertainties reported by each method differ (see Hardebeck and Hauksson, 2001, for discussion of errors). Because the uncertainties estimated by the Gephart and Forsyth (1984) method are greater than the uncertainties estimated by the Michael (1987) method (and because we prefer to possibly overestimate uncertainties rather than underestimate them), we present only the results of the Gephart and Forsyth

(1984) method in Table 3.1. We find that calculated R values ($R=(\sigma2-\sigma1)/(\sigma3-\sigma1)$, where $\sigma1$, $\sigma2$, and $\sigma3$ are the maximum, intermediate, and minimum effective stresses, respectively) tend to be highly variable in adjacent regions and poorly resolved (Gephart and Forsyth, 1984). Specifically, multiple inversions of the same data using slightly different input parameters yield variable R values, although the principal stress direction results are robust and independent of minor variations in input parameters. Therefore, we conclude that R values are insufficiently reliable to be used in subsequent analysis.

Table 3.1
Focal Mechanism Stress Inversion Results

Grid Interval	S1 az	S1 pl	S2 az	S2 pl	S3 az	S3 pl	Misfit
B1	148	45	315	45	52	6	14.9
B2	165	40	342	50	74	2	12.8
C2	141	15	272	68	46	16	10.1
C3	170	41	316	44	64	18	11
D2	145	16	272	64	49	19	12
D3	168	37	326	51	70	11	10
D4	176	46	304	31	53	28	8.7
E3	4	7	198	83	94	2	14
F6	195	48	6	42	100	4	9.9
F7	206	48	8	41	106	9	11.8

S1, S2, and S3 are the maximum, intermediate, and minimum principal stresses, respectively. Misfit is the average difference in degrees between the obseved slip vector and the traction vector predicted by the best fitting stress feild.

Figure 3.3 shows the Sh_{MIN} directions obtained from the inversions combined with other stress indicators. The E–W Sh_{MIN} direction in the Round Valley area, southeast of Long Valley, and the NW–SE Sh_{MIN} direction in the Long Valley caldera west moat and Mammoth Mountain areas are consistent with the regional Sh_{MIN} direction characteristic of the Walker Lane zone on the western edge of the

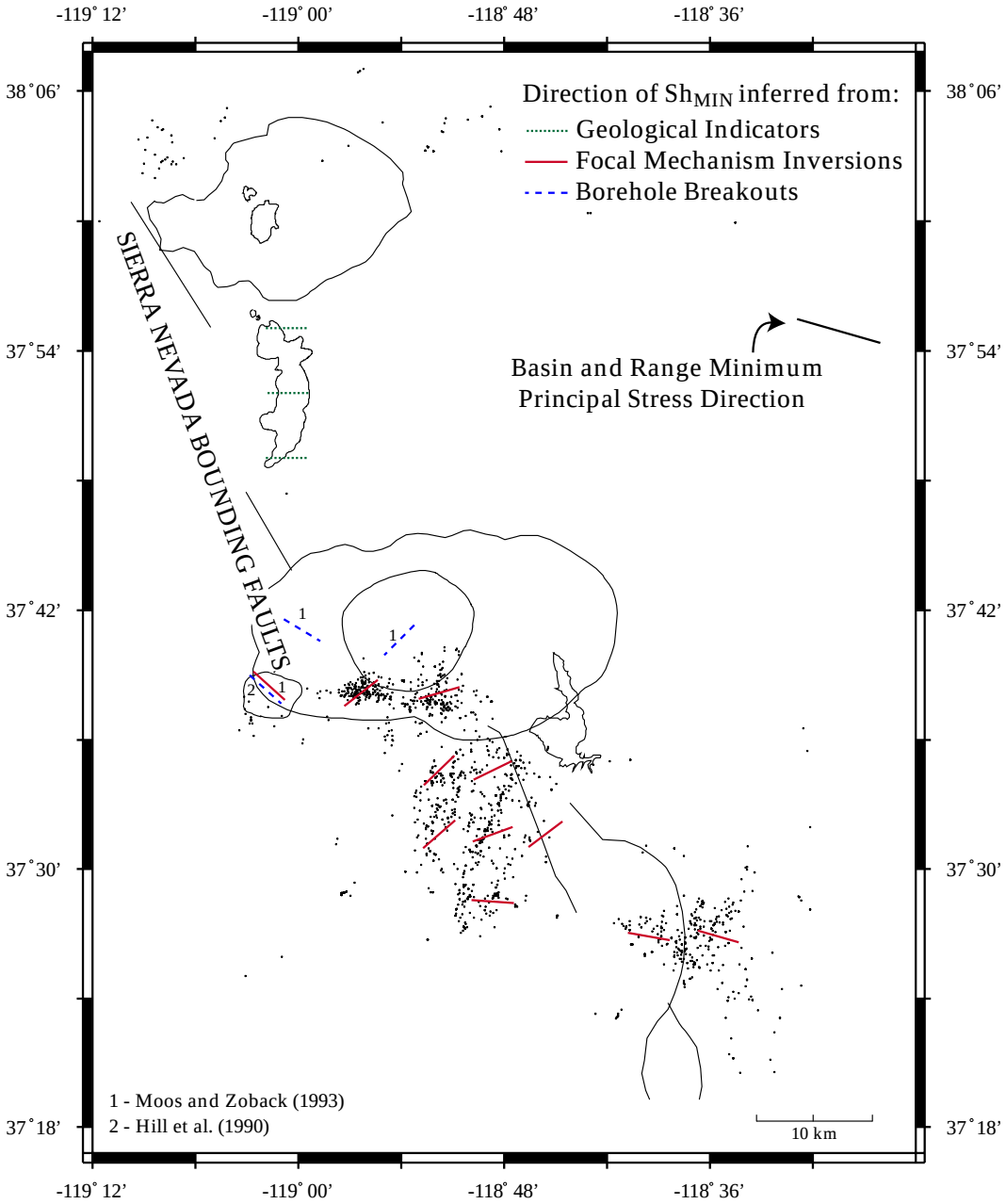

Figure 3.3 - Map showing trajectories of Sh_{MIN} in the Long Valley area based on focal mechanism stress inversions (this work) (red solid lines), borehole breakouts (1) (Moos and Zoback, 1993) and T axes (2) (Hill et. al, 1990) (blue dashed lines), and geological indicators (Bursik and Sieh, 1989) (green dotted lines). Dots are epicenters of earthquakes used in stress inversions.

Basin and Range province (Bellier and Zoback, 1995). The E–W Sh_{MIN} direction implied by opening of the N-S trending Mono / Inyo dike (Bursik and Sieh, 1989) is also generally consistent with this regional stress field. However, we find that within the caldera, the Sh_{MIN} direction is locally rotated to a NE–SW relative extension direction, verifying the results of Moos and Zoback (1993) (Figure 3.3, Table 3.1). This apparent perturbation is strongest in the western south moat and gradually rotates to the regional Sh_{MIN} direction with distance south and east of the caldera. Although focal mechanism data are too sparse for a formal stress inversion immediately north and southwest of the Long Valley caldera, P and T axes from those focal mechanisms that have been determined in these areas imply E–W to NW–SE relative extension, consistent with the background stress field (Figure 3.4). This implies that the stress perturbation is centered roughly on the south moat / southern resurgent dome area.

The average misfit values for these inversions are high considering the large number of first motions used to constrain the focal mechanisms (Table 3.1). However, despite the high misfits, we have confidence that the observed stress rotation is real since it is quite evident in the spatial variations of T axes (Figure 3.2). The high misfits probably result from a combination several reasons. First, stress field may vary temporally and / or spatially over small distance scales. In the west south moat, for example, where misfits are highest, magmatic activity may temporarily alter the stress field in very local areas. If the stress field varies within a 5 km x 5 km bin, we do not satisfy the assumption that the stress field be homogeneous within each inversion area, over the 20 year time interval considered. However, if we decrease the bin size, we will greatly reduce the number of active faults in each bin, leading to insufficient fault diversity and poorly constrained results. A second possible cause of the large misfits is errors in the focal mechanisms themselves. Although these events have a large number of first

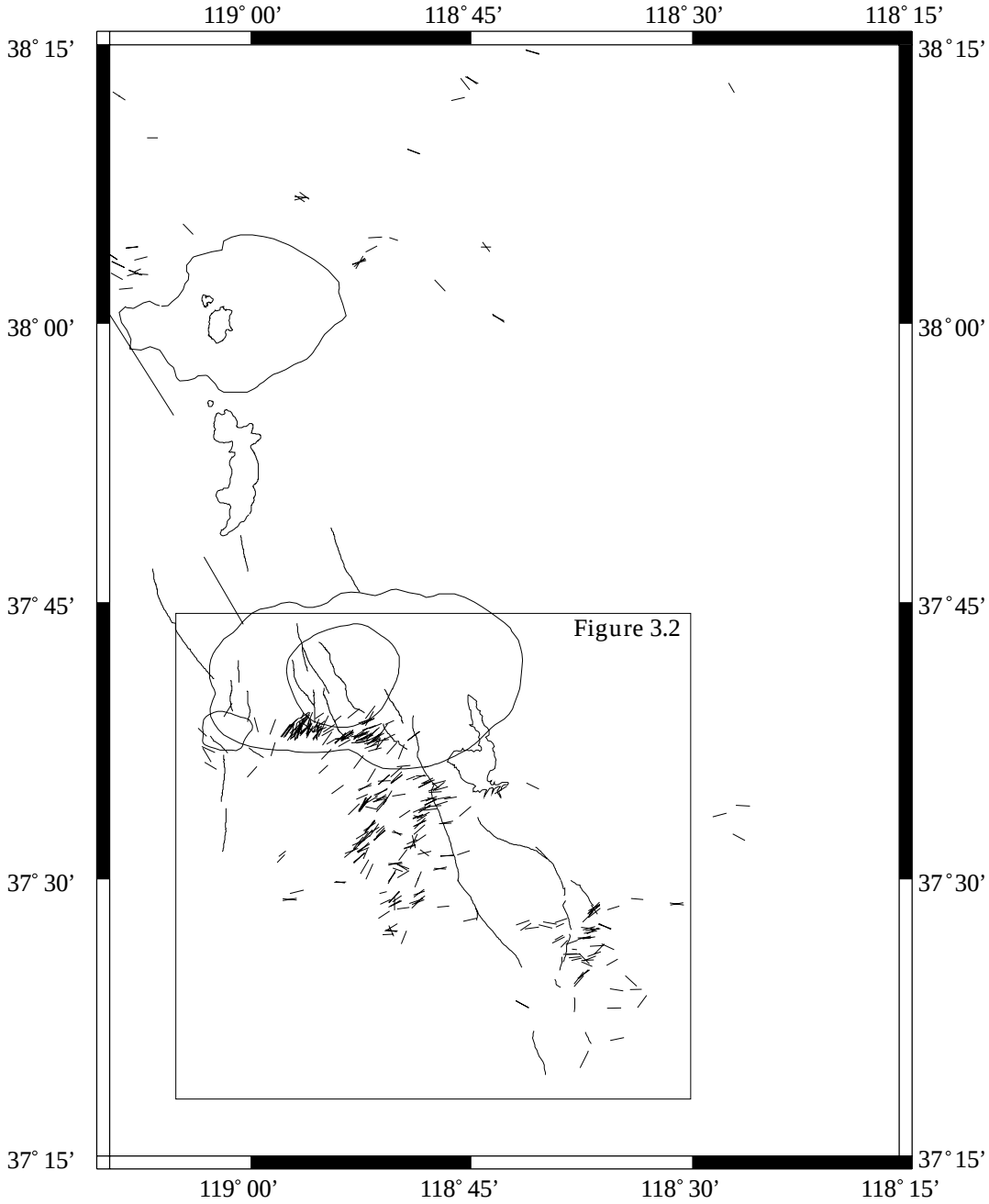

Figure 3.4 - T axes for all earthquakes with more than 75 first motion readings. Box indicates area shown in Figure 3.2.

motions, in some cases the nodal planes are poorly constrained due to erroneous polarity readings and a lack of data in crucial areas of the focal sphere.

A third possible cause of high misfits, particularly in the western south moat, is transient high pore pressure. As explained in Chapter 5, it is possible that during seismic crises, fluids are exsolved from intruding magma bodies, or intruding magma bodies heat ground water. These fluids or gases may create pressure transients which raise the pore pressure and decrease the effective normal stress across faults of all orientations. This hydraulic weakening process enables faults of widely varying orientations to slip in the same stress field. Based on evidence presented in Chapter 5, we believe this hypothesis to be the most likely cause of high misfits in the west south moat.

3.4 Synthesis: Fault Kinematics of the Long Valley Area

By combining fault orientation information obtained from relocated seismicity (see Chapter 2) with knowledge of focal mechanisms and stress inversion results, we can determine slip vectors on the fault planes and generate a model of fault motions in the caldera and SNB. We find average slip vectors in two ways. We average the rakes on the fault planes based on focal mechanisms (method 1), and we calculate slip vectors on fault planes (determined from the relocated seismicity) using stress results from the focal mechanism inversions and an assumed R value (method 2).

To estimate the average rake on each fault plane using focal mechanisms directly (method 1), we select all focal mechanisms that are located within 200 m of a given fault plane. For many of these, one of the nodal planes coincides with the measured fault plane within +/– 25˚. If the disagreement is greater than 25˚, we assume that the earthquake did not occur on the fault plane or that the focal mechanism is not well constrained, and remove it from the data set. The rakes on

the presumed fault plane are then averaged to obtain an average rake (Rake 1 in Table 3.2).

As an example of method 1, Figure 3.5 shows focal spheres with compression and dilatation readings and the corresponding focal plane solutions for plane SERD4. We selected this fault as an example because the limited amount of data permits us to show all of the focal mechanisms used in this study. In 8 out of 9 cases, the fault defined by microseismicity is either consistent with the focal mechanism solution (a-d) or is generally consistent with constraints provided by the compression and dilatation measurements (e-h). This implies that many of the earthquakes with focal mechanisms which do not correspond well with the relocation-defined fault plane may simply be poorly

Table 3.2
Rake Analyses

Fault	Rake 1*	(Standard Deviation)	Rake 2**	Region
SNB1	-45	30	-33	D2
SNB2	2	45	-15	D3
SNB3	7	28	-5	E3
SNB4	178	38	-159	C3
SERD1	-	-	-174	B2
SERD2	-	-	-115	B2
SERD3	-2	29	-45	B2
SERD4	-20	27	-59	B2
SERD5	-	-	-135	B2
ESMSZ1	179	24	-165	B2
ESMSZ2	176	19	-167	B2
WSMSZ1	NA	-	-168	B1
WSMSZ2	NA	-	-96	B1
SWRD1	-	-	-138	B1
SWRD2	-	-	-180	B1

* Method 1 - rake averaged from focal mechanisms [not enough data (-), not a simple fault plane (NA)]
** Method 2 - rake calculated based on stress model, assuming R=0.

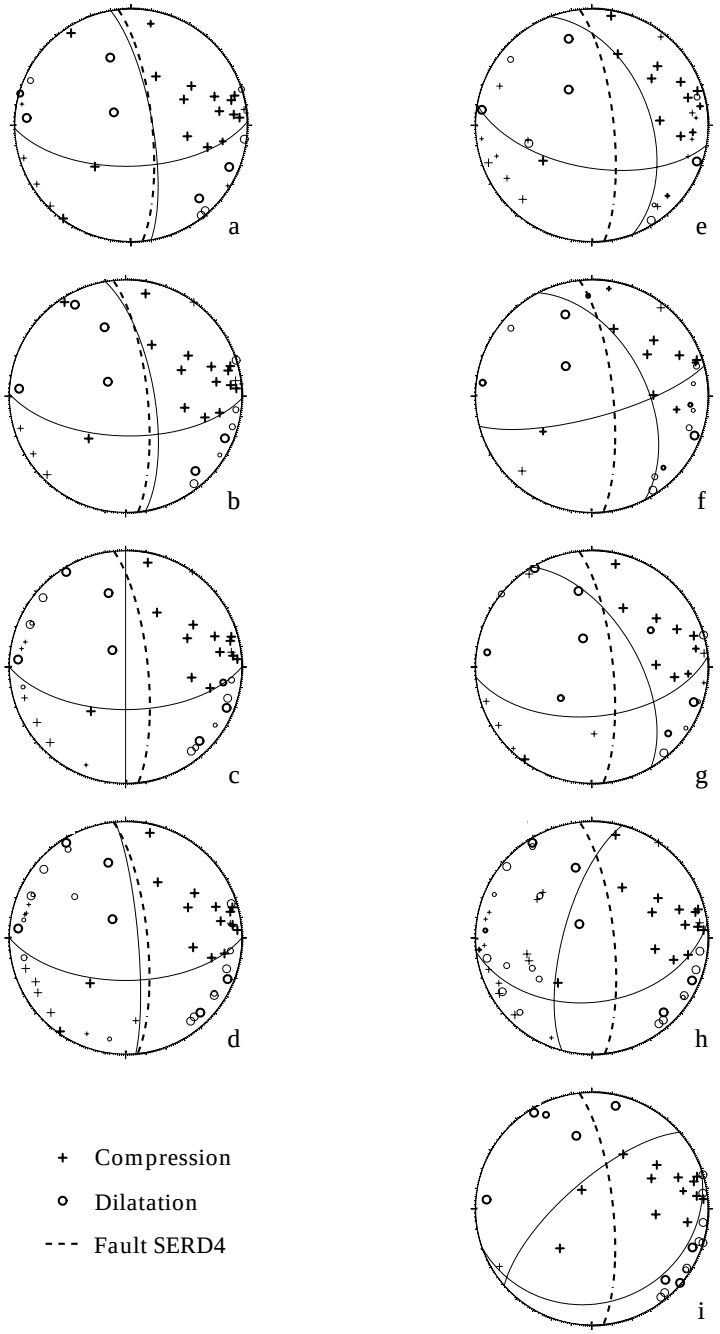

Figure 3.5 - Focal mechanisms used in this study for earthquakes within 200 m of plane SERD4. Mechanisms in the left column agree with the identified plane (dashed line) within 25˚, and are therefore to obtain an average rake on the plane (Table 1). Mechanisms in the right column are not included in finding the average rake as they do not fit the defined plane within 25˚. Compression is signified by +, and dilatation by o. Size of symbol indicates weight.

determined, rather than actually rupturing a different plane. This inference is true for focal mechanisms in the east south moat and southeast resurgent dome areas, and for focal mechanisms in the SNB, provided that they are located on a seismicity-defined plane (The SNB contains much background seismicity that appears to rupture small planes of varying orientations.). The example in Figure 3.5 demonstrates the reliability of rake method 1 for determining fault motions for most of the Long Valley caldera area. Method 1 is not reliable for the WSMSZ fault zone, however, since earthquakes in this region are not occurring on a small number of well defined fault planes (see Chapters 2 and 5).

To calculate rakes on the fault planes using method 2, we must know the orientations of the principal stresses and their relative magnitudes. The stress inversions described previously provide the orientations of the principal stresses throughout the region. Because the R values from the stress inversions are poorly constrained, however, we use other information about the tectonic environment to establish the relative magnitudes of the stresses and complete the stress model. Because this is a normal/strike-slip faulting regime (Zoback, 1989; Moos and Zoback, 1993; Bellier and Zoback, 1995), we assume $S_{HMAX} \sim S_V$ and R~0.

Table 3.2 demonstrates that method 1 and method 2 give results that are generally consistent, with the exception of faults SERD3 and SERD4. Because method 2 predicts a greater component of normal motion than we observe on SERD3 and SERD4, the R value in the southeast resurgent dome area may be slightly higher than in other regions of the study area, for which R=0 seems to be a good approximation. The general agreement between the two methods supports the appropriateness of our stress model and its use to determine the direction of slip on these faults. Therefore, we proceed to use the stress model described in Table 3.1 to calculate the sense of motion on planes in the caldera for which the slip direction cannot be determined from focal mechanisms.

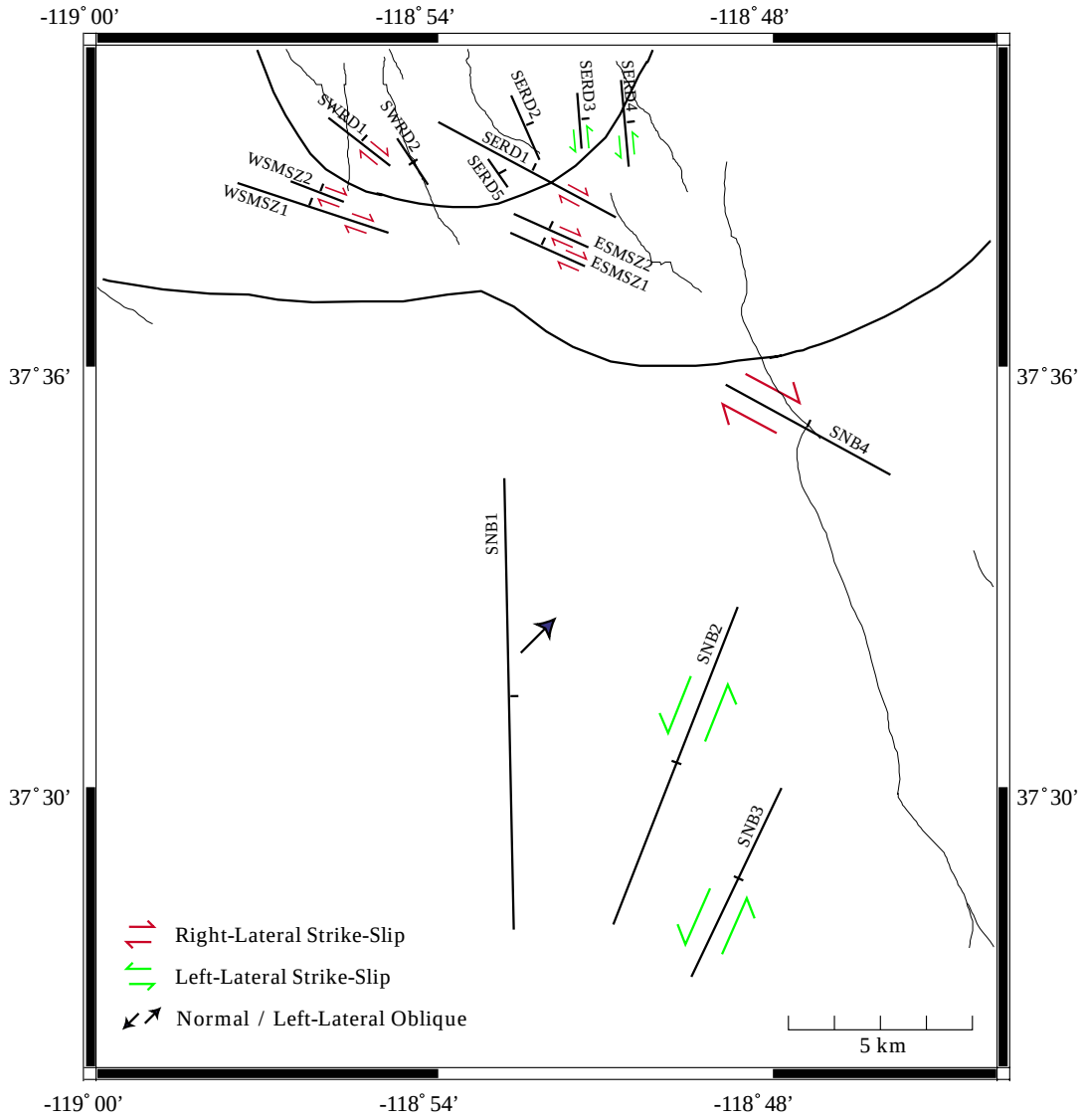

Figure 3.6 - Map of faults identified by relocated recent seismicity in the Long Valley caldera and in the Sierra Nevada basement south of the caldera. Fault are named based on their location, where WSMSZ = west south moat seismic zone, ESMSZ = east south moat seismic zone, SERD = southeast resurgent dome area, SWRD = southwest resurgent dome area, and SNB = Sierra Nevada block. Arrows show the relative sense of slip on the faults. Thin lines are mapped surface traces of faults (Bailey, 1989).

Figure 3.6 demonstrates schematically how fault blocks are moving seismically in the caldera. In the western and eastern lobes of the south moat seismic zone (WSMSZ and ESMSZ), most of the subparallel faults trending roughly E–W and dipping 70˚–80˚NE have nearly pure right-lateral strike-slip motion. This observation is also true for fault SNB4. Although fault SNB4 is not directly connected to the south moat seismicity, kinematically it appears to be an extension of the south moat shear zone formed by the WSMSZ and the ESMSZ because these fault zones are aligned, have similar orientations, and are characterized by right-lateral motion. Despite their northward fault dips, the south moat seismic zone and SNB4 faults are currently not acting as normal faults. Rather, they may be preexisting faults (see Chapter 2) which are currently slipping in a right-lateral sense in the current stress field to form a right lateral shear zone.

Similarly, the more northerly-trending, east-dipping faults in the eastern resurgent dome area are slipping in a left-lateral sense. These planes are relatively poorly oriented for faulting in the current stress field. This observation supports the hypothesis that they are also reactivated preexisting structures (see Chapter 2).

The slip distribution on faults inside the caldera based on our slip analysis is reflected in 1997/98 geodetic data. Deformation in 1997/98 was dominated by inflation beneath the resurgent dome (Simons et al., 2000). However, inflation beneath the resurgent dome does not account for all of the deformation observed. The residual deformation is best modeled by a N80W-striking, steeply-dipping right-lateral strike slip fault across the length of the south moat (J. Langbein, personal communication 2001).

In the Sierra Nevada block, fault SNB1 is a normal fault with a significant left-lateral strike-slip component, while SNB2 and SNB3 are pure left-lateral strike-slip faults. If SNB1 is assumed to continue along its down-dip projection to

depths ~ 2 km deeper than the observed seismicity (Chapter 2, Figure 2.8), seismicity in the SNB is confined to the hanging wall of SNB1. Because SNB1 is subparallel to the Hilton Creek fault, its activity might be thought of as the westernmost extent of Basin and Range normal faulting at this latitude.

Right-lateral slip on fault SNB4 combined with right-lateral slip in the south moat and left lateral slip on fault SNB2 have delineated a sub-block of Sierra Nevada crust which appears to be escaping to the southwest relative to the caldera, as described by Hill et al. (in press) (Figure 3.7). It is important to note, however, that this kinematic analysis reveals only the relative sense of motion of crustal blocks in the caldera and the Sierra Nevada block. Large scale geodetic surveys which extend into the SNB are needed to correctly resolve absolute motion.

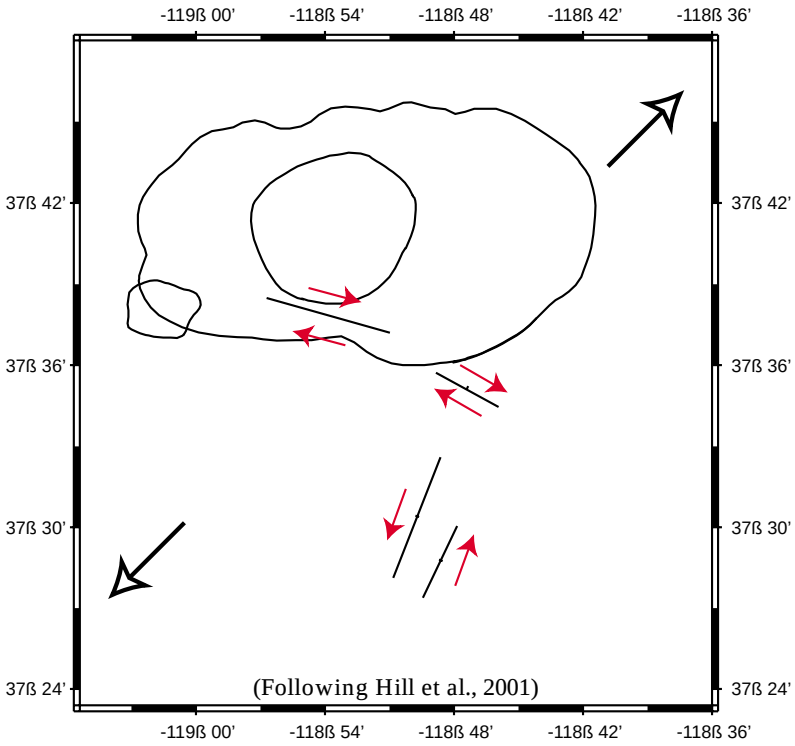

Figure 3.7 - Sense of motion on faults most active from 1997 to present (see Chapter2).

3.5 Evaluating Possible Sources of the Stress Perturbation

We now use the mapped stress field to examine possible driving forces for activity in the caldera region and the interaction between tectonic and magmatic processes. To do this, we model two simple end-member scenarios using the dislocation modeling program, *Coulomb 2.0* (Toda et al., 1998) and investigate the apparent stress anomaly predicted for each in the south moat and adjacent Sierra Nevada block. We evaluate the likelihood of each model based on its consistency with the stress inversion results shown in Figure 3.3. The first model, in which we calculate stresses resulting from an inflational source, represents a purely magmatically driven system. The second model, in which we calculate stresses resulting from extension across the Mono/Inyo dike chain and the Hilton Creek fault, represents a primarily tectonically-driven system.

To understand how the local stresses that we model interact with the larger scale tectonic environment, we must also estimate the background regional stress field. To do this, we use Coulomb faulting theory and assume R=0, a coefficient of friction of 0.6 (see Townend and Zoback, 2000, for review), and that S_3 is oriented N80W (Zoback, 1989; Bellier and Zoback, 1995). We consider two cases, one in which the pore pressure is hydrostatic ($Pp = 0.4\ S_V$), and one in which the pore pressure is super-hydrostatic ($Pp = 0.8\ S_V$), as previously suggested for this region by Moos and Zoback (1993). This leads to the following regional stress regimes at 6.5 km depth (the average depth of seismicity and of the focal mechanism stress inversion measurements): In the hydrostatic case, S_1 (N10E) = S_V = 175 MPa, S_3 (N80W) = 101 MPa; in the super-hydrostatic case, S_1 (N10E) = S_V = 175 MPa, S_3 (N80W) = 151 MPa.

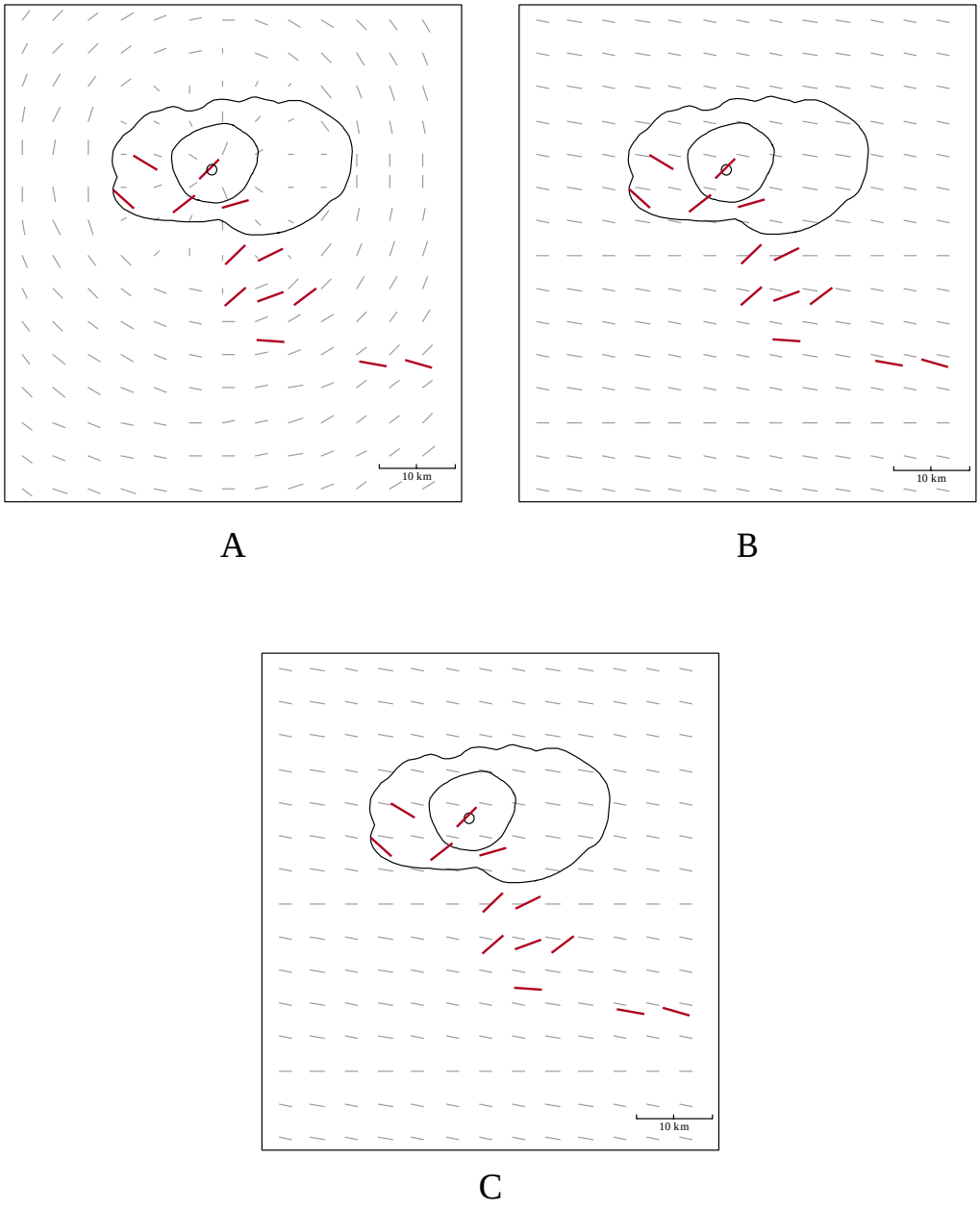

Figure 3.8 - Dislocation modeling results of S_3 direction due to 0.1 km^3 inflation of a Mogi source at 10 km depth (gray lines). Red lines are S_3 observations for comparison. Line length indicates plunge of S_3 axis where short lines are steeply plunging. Location of Mogi source shown with circle. (a) S_3 direction due to inflation combined with an isotropic background stress field. (b) S_3 direction due to the inflational source combined with estimated regional stress field assuming hydrostatic pore pressure (Pp = 0.4 S_V). (c) S_3 direction due to the inflational source combined with estimated regional stress field assuming high pore pressure (Pp = 0.8 S_V).

In the first model, we represent magma chamber inflation beneath the resurgent dome as a Mogi point source at 10 km depth (Simons et al., 2000) with 0.1 km^3 of inflation (Battaglia et al., 1999). Figure 3.8 shows the calculated directions of S_3 at 6.5 km depth due to inflation of the Mogi source in the cases of a) an isotropic background stress field, b) a background stress field associated with hydrostatic pore pressure, and c) a background stress field associated with super-hydrostatic pore pressure. In the isotropic stress field case, where the inflational source strongly controls the direction of the least principal stress (Figure 3.8a), inflation creates a radially symmetric pattern in the S_3 direction about the center of the resurgent dome (short lines denote steeply plunging S_3). This magmatically-driven model is inconsistent with stress observations within the caldera, immediately south of the caldera, and in Round Valley (30 km southeast of the caldera), although it correctly predicts the S_3 direction in the mid-SNB. Interestingly, when the stresses from the inflational source are combined with more realistic regional stress fields, the inflation signal is too weak to perturb the stresses significantly from the background stress field (Figure 3.8b, c) at the average depth of seismicity, and therefore, cannot explain the observed stress field rotation. These conclusions do not change for source depths ranging from 7 km to 15 km. Thus, an inflating magma chamber beneath the resurgent dome as the sole source of the stress perturbation does not seem to be a likely hypothesis.

Alternatively, regional tectonic processes could be instrumental in driving deformation in the area, resulting in the observed stress perturbation. South of the caldera, the large normal-slip displacements in the glacial moraines on the Hilton Creek fault indicate that this fault has accommodated a large portion of regional WNW–ESE extension during the Holocene, averaging one **M**6.5 earthquake every 500 years (Bailey, 1989) (Figure 3.9). North of the caldera, the

opening of the Mono / Inyo dike chain has likewise accommodated a large portion of regional WNW–ESE extension along the Sierran front (Bursik and Sieh, 1989). For example, the eruption which formed Obsidian Dome ~600 years ago (Bailey, 1989) was fed by a dike approximately 7 m thick in the E-W direction (Eichelberger et al., 1986). As Figure 3.9 shows, the WNW-ESE trending faults in the south moat of the caldera, form a right-lateral "transform" zone in the left step-over between the Hilton Creek fault and the Mono / Inyo dike. Thus, we suggest that the south moat stress perturbation may be a result of the overall geometry of the Sierran front and localized areas of tectonic extension might be providing conduits for magma and magmatically-derived fluids to move to the surface.

To test this possibility, we constructed a model of normal slip on the Hilton Creek fault and E-W opening along the Mono / Inyo dike that represents deformation of these structures over about the last 1000 yrs. The purpose of this model is to investigate the state of stress in the Long Valley caldera area resulting from the interaction of extension across these two structures. Thus, the model assumes that local extension has occurred relatively recently, such that any stress perturbations caused by the interaction of these structures have not yet relaxed. We imposed a maximum of 6 m of pure normal slip on the Hilton Creek fault and a maximum of 10 m of E–W opening across the Mono / Inyo dike and simplified the geometry of these features (Figure 3.10). Displacement across both the dike and the fault is tapered to zero at the top and sides, and both features are assumed to cut through the entire crust and the upper mantle. Realistically, extension across these discrete structures probably occurs over a more shallow depth range. However, because the lower crust at the base of the seismogenic zone is not truly elastic, as is assumed in our model, we extended displacement to great depth to avoid

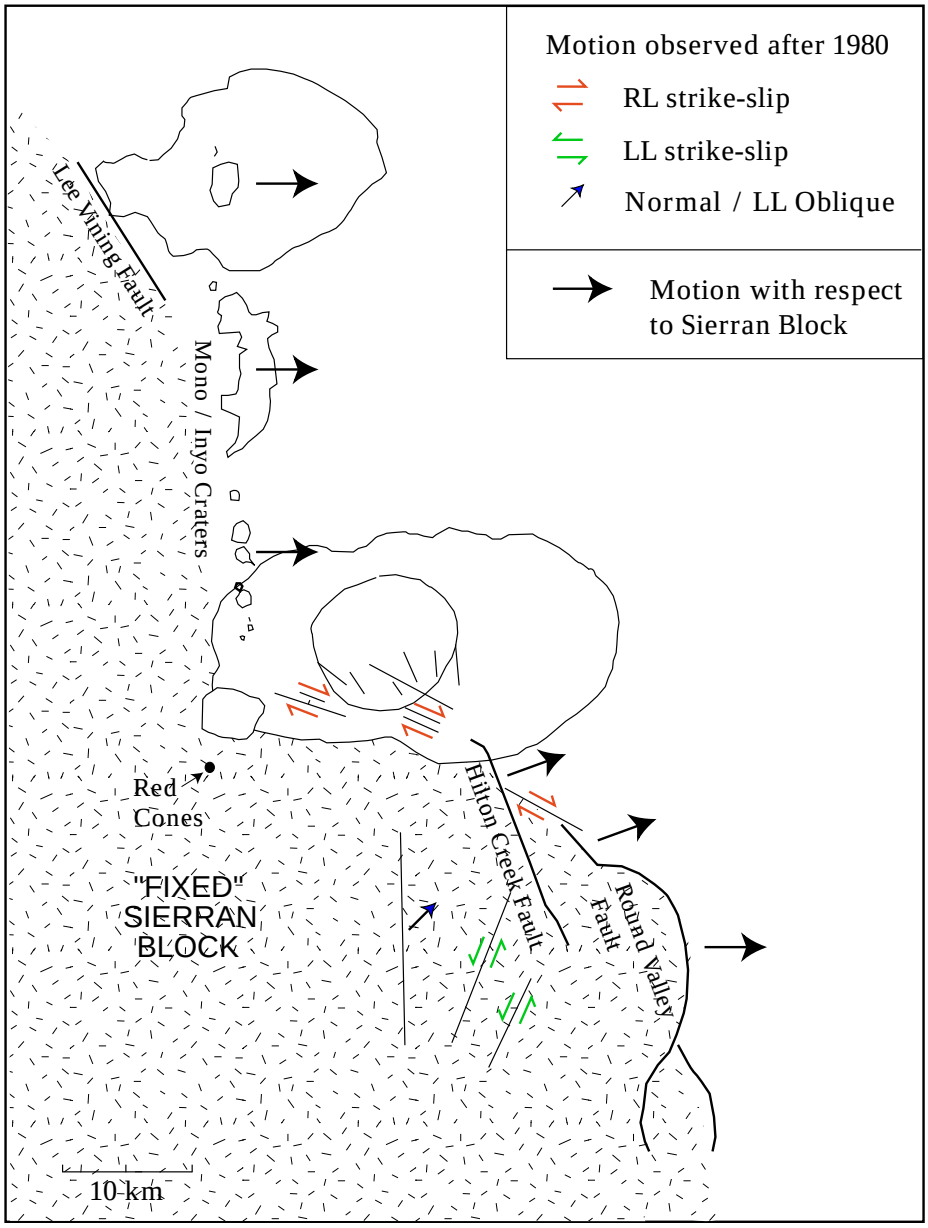

Figure 3.9 - Schematic map of Long Valley area kinematics. Large solid arrows show motion in reference to a stationary Sierra Nevada Block. Small open arrows show relative motion on faults. The southern caldera forms a right-lateral "transform" zone in the left-step between locales of extension, which are shown by solid arrows with reference to a stable Sierra Nevada.

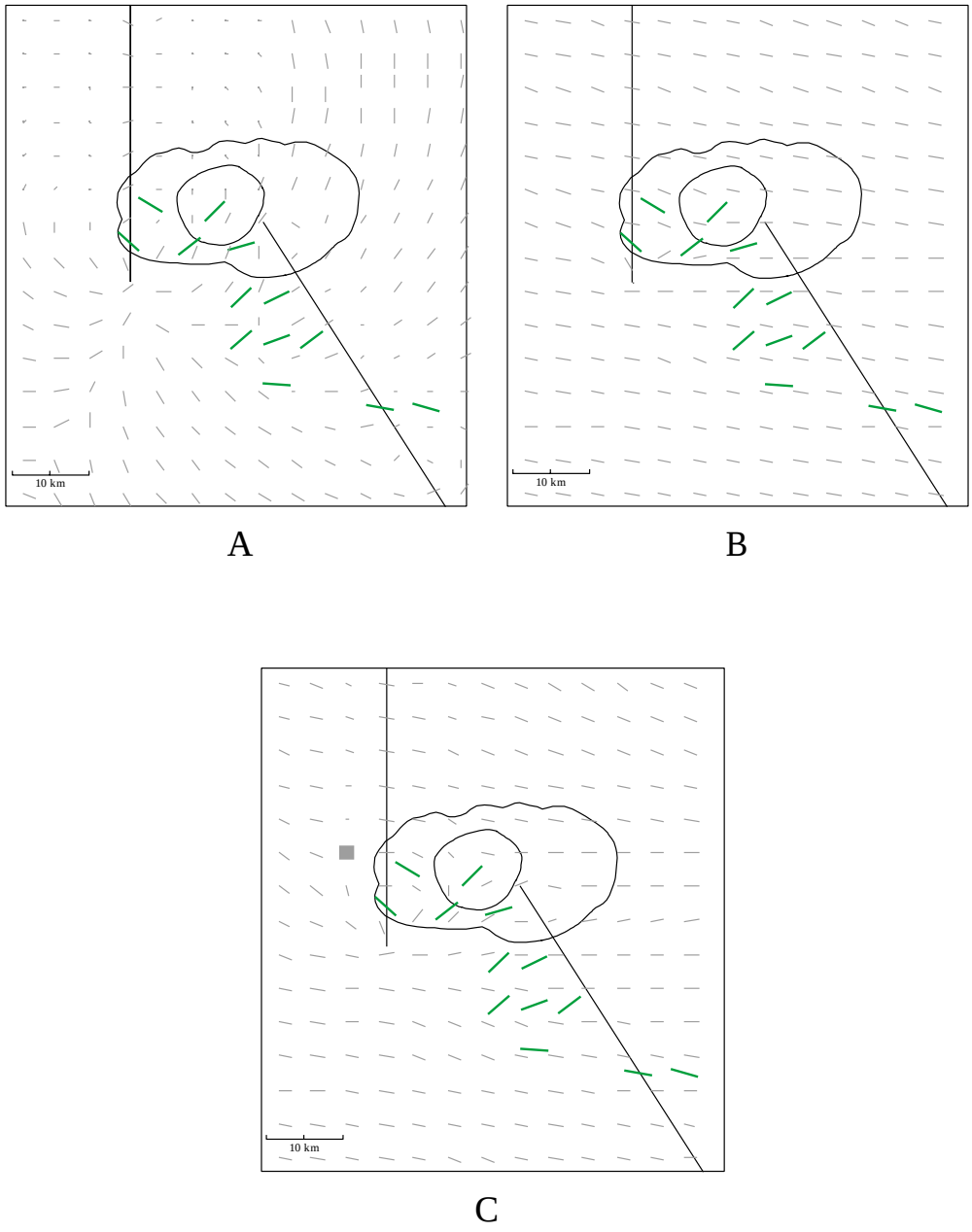

Figure 3.10 - Dislocation modeling results of S_3 direction resulting from opening across the Mono/Inyo dike chain and normal slip on the Hilton Creek fault (gray lines). Black lines are S_3 observations for comparison. Line length indicates plunge of S_3 axis; short lines are steeply plunging. (a) S_3 direction due to extension combined with an isotropic background stress field. (b) S_3 direction due to extension source combined with estimated regional stress field assuming hydrostatic pore pressure ($Pp = 0.4\ S_V$). (c) S_3 direction due to extension combined with estimated regional stress field assuming high pore pressure ($Pp = 0.8\ S_V$).

unrealistic stress concentrations at the base of the faults. Models in which displacement only occurs through the seismogenic upper crust give similar results. The Hilton Creek fault is modeled by a fault dipping 60˚ towards N60E that extends slightly into the caldera. The Mono/Inyo dike is modeled as a vertically opening feature extending from Mono Lake to ~5 km beyond the Red Cones (Figure 3.9).

The S_3 directions resulting from extension across these structures combined with the three theoretical regional stress fields described earlier are shown in Figure 3.10. If local effects due to extension across the Hilton Creek fault and Mono/Inyo dike dominate the stress field in the area, as in the isotropic background stress field case (Figure 3.10a), the calculated stress field agrees poorly with observations. If the more realistic anisotropic regional stress field model with hydrostatic pore pressure is correct, the local stress perturbations in this model are too weak to perturb the background stress field to the degree we observe (Figure 3.10b). However, if pore pressure is unusually high, local stress perturbations due to extension result in a stress distribution that is reasonably consistent with the observations throughout the caldera, in the southern SNB, and in Round Valley (Figure 3.10c). Although this model (3.10c) does not correctly reproduce stress directions observed in the SNB just south of the caldera, overall, it fits the other observations fairly well. This model also provides a reasonable explanation for why seismicity is concentrated in the south moat of the caldera, while the caldera's north moat is essentially aseismic.

Due to the simplicity of these models, we are overlooking additional likely sources of stress in the caldera area (such as other inflational sources, dikes, and faults) that might account for the discrepancies between the models presented here and the observations. Also, because the details of the calculated stress distributions are strongly dependent on the details of the models, adjusting model

parameters could lead to results more consistent with the observations, particularly in the case of the tectonically driven stress perturbation with high pore-pressure (Figure 3.10c). For example, if we have underestimated the pore pressure or overestimated the magnitudes of the regional stresses in the SNB in the model shown in Figure 3.10c, S_3 would be more strongly rotated to the NE in this area (Figure 3.10a) and would therefore be more consistent with the observations. However, we do not want to tweak model input parameters arbitrarily to generate results which better fit observations. Another important consideration is that we have modeled these dislocations as occurring in a homogeneous elastic half-space. If the crust were modeled by an elastic plate over a viscoelastic lower crust, the magnitude and extent of the south moat stress perturbation due to the left-step in locales of extension would be greater.

Because the true details of the distribution of crustal properties, the distribution of tectonic activity, and the magnitudes of the regional stresses at depth are unknown, we cannot correctly resolve the extent or the magnitude of the stress rotation across the south moat created by tectonic activity. Thus, the tectonically-driven model is somewhat speculative and poorly constrained. However, in the tectonically-driven model the general direction of the stress perturbations created by the step-over in Sierran bounding extension is consistent with observations, whereas the stress perturbations created by the inflation-driven model are inconsistent with observations.

3.6 Summary

Focal mechanism stress inversions reveal that the direction of minimum compressive stress systematically rotates across the studied region, from a NE–SW relative extension direction in the south moat of the caldera, to a WNW–ESE relative extension direction in Round Valley, 25 km SE of the caldera. Because WNW–ESE extension is characteristic of the western boundary of the Basin and Range province, the stress rotation in the vicinity of the caldera appears to reflect a local stress perturbation centered near the caldera south moat area. This stress perturbation does not appear to result from magma chamber inflation beneath the center of the resurgent dome, but may reflect the large-scale left-step offset in the Sierran range bounding normal faults. Thus, although magmatic activity may trigger earthquakes in the Long Valley area, the direction of fault slip seems to be controlled by regional tectonic processes rather than local magmatic processes.

Acknowledgements

We are grateful to Dave Hill, George Thompson and Roy Bailey for sharing their knowledge about the Long Valley caldera in stimulating discussions. We also thank Ross Stein for his time and advice on using Coulomb 2.0 software and Jim Savage and Fred Pollitz for their helpful reviews.

Chapter 4

SOURCE PARAMETERS OF TECTONIC EARTHQUAKES AND ATTENUATION IN THE LONG VALLEY CALDERA

A shorter version of this chapter was published with Bill Ellsworth as coauthor in the *Bulletin of the Seismological Society of America*, **91**, April 2001.

4.1 Abstract

To understand better the source processes of typical “tectonic” earthquakes in the Long Valley caldera, California, we measured source parameters for 41 earthquakes (**M** 0.5 to **M** 5) recorded at 2 km depth in the Long Valley Exploratory Well (LVEW). Borehole recordings provide a wide frequency bandwidth, 1 to 200 Hz in the case of LVEW, and greatly reduce seismic noise and path effects compared to surface recordings. We calculated source parameters in both the time and frequency domains for P and S waves. Source parameters are corrected for radiation pattern and attenuation. Earthquakes studied in this analysis are well described by the ω^2 source model (Brune, 1970). However, at frequencies above the corner frequency, spectra decay faster than ω^3, indicating that attenuation is significant in the caldera and plays an important role in shaping the spectra (path averaged Q_p = 100–400, Q_s = 200–800).

Both static stress drops and apparent stresses range from approximately 0.01 to 30 MPa. Although static stress drops do not vary with seismic moment for these data, our analyses are consistent with apparent stress increasing with increasing moment below ~**M** 2. Above **M** 2, we generally observe self-similar scaling in apparent stress. To estimate tectonic driving stress and seismic efficiencies in the region, we combine source parameter measurements with knowledge of the stress field and a Coulomb failure criterion to infer a driving stress of 40 - 70 MPa. Subsequent seismic efficiencies are consistent with McGarr's (1999) hypothesis of a maximum seismic efficiency of 6%. These source parameters are consistent with those measured in a deep borehole in Cajon Pass, California (Abercrombie, 1995). Thus, Long Valley "tectonic" earthquakes appear to have the same source processes as earthquakes in non-volcanic regions.

4.2 Introduction

To understand better the nature of faulting in the Long Valley caldera, this study investigates earthquake source parameters of typical tectonic-style earthquakes in the caldera and the nearby Sierra Nevada by estimating static stress drop, apparent stress, and seismic efficiency of small to moderate-sized "tectonic" earthquakes recorded at 2 km depth in the Long Valley Exploratory Well (Figure 4.1). Abercrombie (1998) demonstrated that seismic noise and path effects, particularly scattering and intrinsic attenuation, are greatly reduced in deep boreholes as compared to surface recordings. Therefore, separating the signal of the earthquake source from path effects is much simpler and more reliable in a deep borehole than at the Earth's surface.

Previously, Archuleta et al. (1982) and Archuleta (1986) used shallow borehole and surface recordings to determine source parameters of earthquakes occurring in the south moat of the Long Valley caldera and in the adjacent Sierra Nevada basement to the south. They found that events with moments above $1x10^{14}$ N-m exhibited constant stress drop scaling with stress drops of 0.1 to 10 MPa, while at smaller moments stress drops decrease with decreasing moment. However, Abercrombie's (1995) study of southern California earthquakes recorded in the Cajon Pass borehole showed that constant stress drop scaling continues to $\mathbf{M} < -1$. This result was corroborated by Hough et al. (1999) and supports Anderson and Hough (1884) and Anderson (1986), who speculated that the observed breakdown of constant stress drop scaling is an artifact of high near surface attenuation. Abercrombie also found that apparent stress (rigidity times the ratio of radiated seismic energy to moment) decreases with decreasing moment for earthquakes in southern California along the same trend as seen by Kanamori et al. (1993), Mayeda and Walter (1996), and Singh and Ordaz (1994).

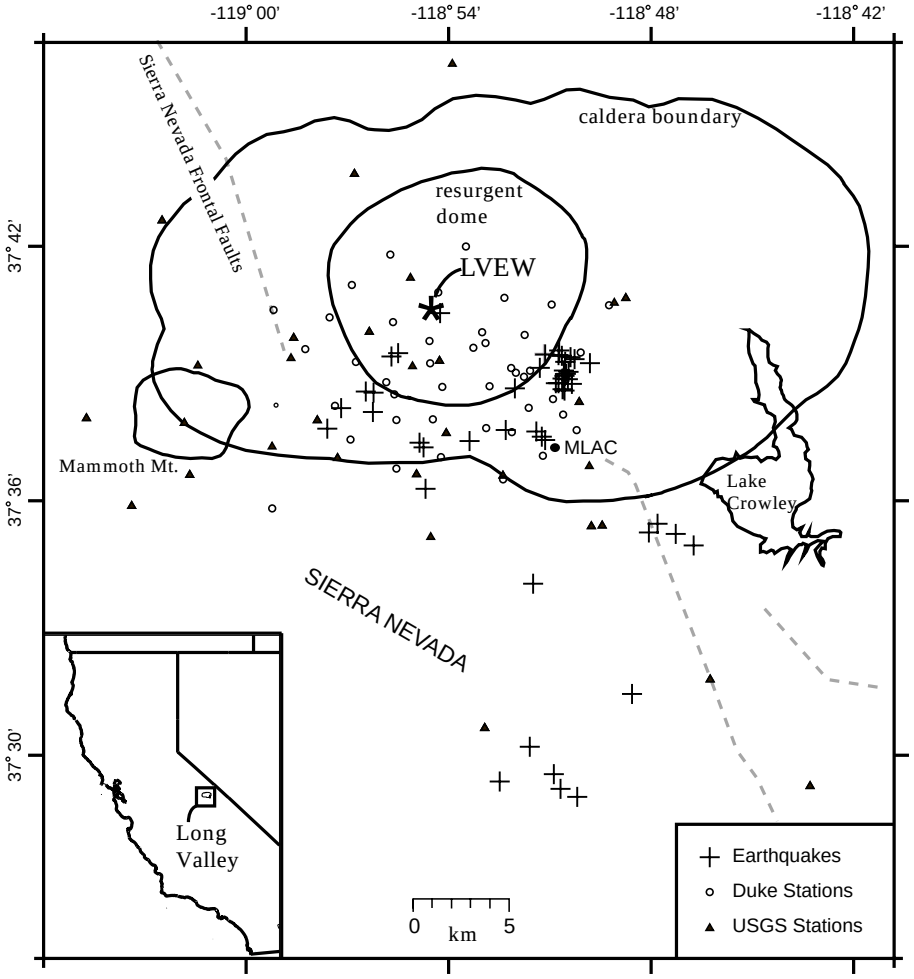

Figure 4.1 - Map of the Long Valley caldera showing the caldera and resurgent dome boundaries and the events and seismic stations included in this study. The crosses are the earthquakes analyzed. The open circles represent the temporary network operated by Duke University, and the triangles represent the permanent USGS array. TERREscope station MLAC is indicated with a dot. The location of the Long Valley Exploratory Well is show by the star in the middle of the resurgent dome of the caldera (37:40.8' N, 118:54.6' W). The inset shows the location of the caldera in California.

In this study we test the generality of Abercrombie's source scaling results by conducting a similar study in the Long Valley caldera. We only analyze earthquakes that appear to have typical tectonic waveforms (due to shear failure in a brittle environment) to determine if Long Valley caldera tectonic-type earthquakes are governed by the same failure mechanisms as earthquakes in other non-volcanic regions. We constrain tectonic driving stresses in the Long Valley caldera using Coulomb faulting theory and combine these results with calculated source parameters to investigate the seismic efficiency of earthquakes in the caldera.

4.3 Data

In September 1997 a three-component high-temperature geophone was installed at 2050 m depth in the Long Valley Exploratory Well, which is located in the center of the resurgent dome of the caldera (Figure 4.1). The 10 Hz seismometer was clamped in competent metapelite basement rock, just below a 2 km thick layer of Bishop tuff, intrusives, and other volcanics (Figure 4.2) (McConnell et al., 1997). Recording began during the buildup of activity leading to the episode of seismic unrest in late 1997 and continued into June 1998.

We analyzed 41 earthquakes ranging in size from **M** 0.5 to **M** 5.0 and in distance 1 to 20 km from the sensor (Figure 4.1). Hypocentral depths are 3 to 9 km (Table 4.1). Most of these events were recorded in September 1997, two months before the crisis described in Chapter 5, when Duke University was operating a dense temporary seismic network in the caldera (Figure 4.1) (Stroujkova and Malin, 2000). The exceptional seismic network obtained by combining the Duke

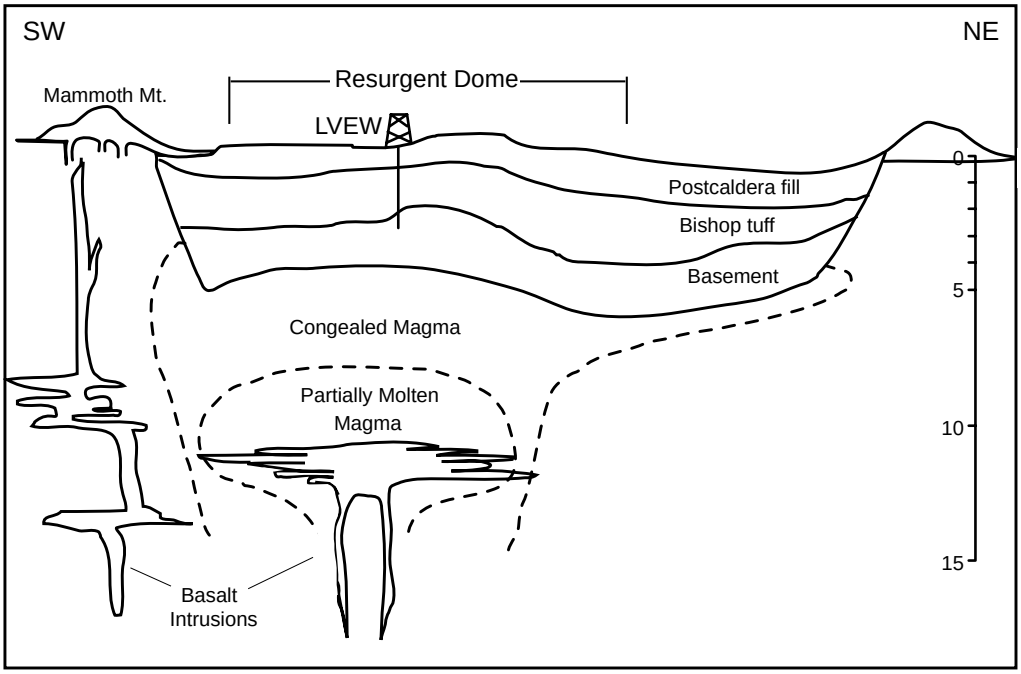

Figure 4.2 - Schematic NE/SW cross section of the Long Valley caldera showing location of borehole with respect to caldera structure and suspected magmatic activity (Bailey, 1989).

and USGS networks allows us to generate well constrained focal mechanisms and accurate hypocentral coordinates using these earthquakes. The earthquakes were recorded on Reftek 72A data loggers at sample rates of 1000/s in September 1997, and 250/s in September 1997 - May 1998 (no data for December 1997). Data in April – June 1998 were recorded at 10,000/s on a Kinkei EDR 6000 data logger.

Table 4.1
Events Analyzed

Event Date*	M	Latitude	Longitude	Depth	Dip Direction	Dip	Rake
9701111854	1.6	37.6498	118.9183	4.21	NA	NA	NA
9709112323	1.9	37.5237	118.8088	5.33	210	75	-180
9709151934	1.8	37.6572	118.8392	7.24	195	25	-160
9709152242	1.7	37.6553	118.8837	5.76	90	45	10
9709160251	1.7	37.6588	118.6588	5.90	110	55	0
9709160912	1.5	37.6577	118.9287	5.96	280	80	20
9709170247	1.7	37.6580	118.8440	5.11	85	85	-10
9709172200	2.8	37.4888	118.8747	4.10	40	90	180
9709201047	2.0	37.5030	118.8695	5.44	225	30	-130
9709210331	0.8	37.6582	118.9075	3.55	115	65	0
9709210949	1.9	37.6580	118.8520	5.69	105	80	0
9709211614	2.4	37.6470	118.8465	6.35	90	85	-10
9709211620	1.2	37.6565	118.8417	5.60	95	90	0
9709211659	1.4	37.5745	118.8628	5.15	NA	NA	NA
9709211856	2.1	37.6488	118.8432	6.31	85	80	-30
9709211910	1.8	37.6467	118.8385	6.26	185	60	-180
9709211915	1.0	37.6502	118.8552	5.25	190	50	-130
9709212050	2.9	37.6497	118.8457	5.39	185	70	-170
9709212102	2.0	37.6500	118.8422	6.25	190	70	-170
9709212107	2.3	37.6507	118.8417	5.84	185	65	-170
9709212115	1.7	37.6515	118.8402	5.5	90	80	-20
9709212301	1.4	37.6258	118.8718	8.19	210	45	-180
9709212340	1.4	37.6550	118.8298	7.77	90	85	-10
9709220213	1.8	37.6442	118.8423	6.47	185	55	-150
9709230130	2.2	37.6052	118.9115	5.73	205	70	180
9709230256	2.1	37.4845	118.8432	7.98	310	70	10
9709230326	1.6	37.4860	118.8440	7.18	305	55	10
9709230631	0.5	37.6561	118.8757	3.37	NA	NA	NA
9709230734	0.6	37.6629	118.8763	3.22	NA	NA	NA
9709240150	0.9	37.6243	118.8520	4.77	120	55	10
9709240911	1.4	37.6290	118.9607	8.45	150	35	30
9711041302	2.3	37.6457	118.8632	5.05	170	80	-180
9711071517	3.1	37.6235	118.8915	3.78	25	90	-150
9711230219	3.5	37.6402	118.9515	7.4	5	80	170
9802971938	3.3	37.6347	118.9337	8.56	55	60	-60
9805240310	2.6	37.6280	118. 8553	7.92	205	50	-170
9806080355	3.5	37.5900	118.7972	6.61	120	60	10
9806090524	5.0	37.5888	118.7953	6.73	130	60	20
9806090829	2.8	37.5852	118.7887	7.62	220	65	150
9806090845	3.4	37.5825	118.7813	6.98	125	75	10
9806091330	3.4	37.5862	118.8002	5.83	120	65	10

*First six digits are the year, month, and day. Seventh and eigth digits are the hour. Last two digits are the minute.

The borehole data have impulsive P and S phases, show minimal scattering, and have excellent high frequency content compared to surface recordings, reflecting high attenuation in the upper 2 km of caldera fill (Figures 4.3 and 4.4). Spectra display high signal to noise ratios at frequencies up to 300 Hz for nearby earthquakes (Figure 4.5) and 150 Hz for more distant events. Removing the instrument response typically allows us to recover the low frequency spectrum to 2–3 Hz for **M**<2 events and to lower frequencies for larger magnitude events.

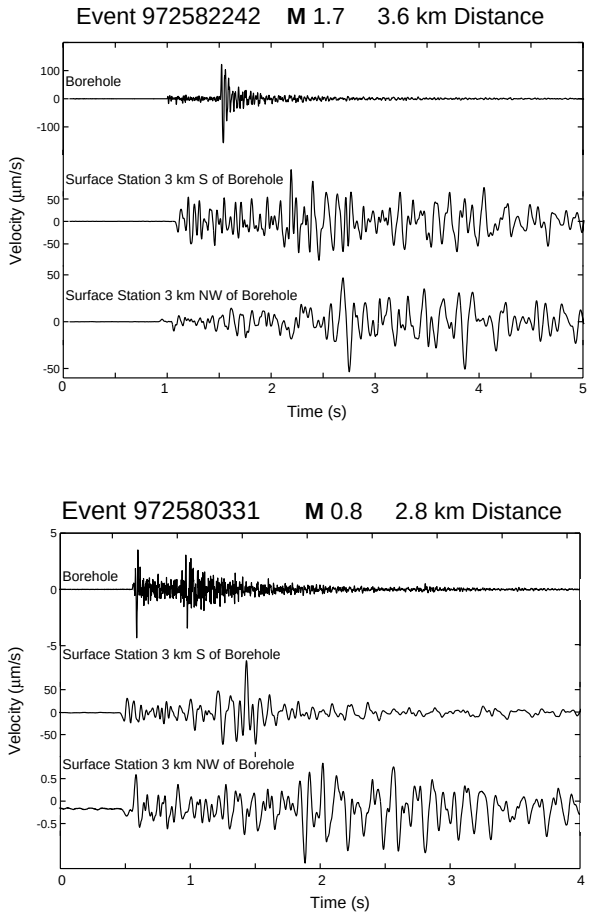

Figure 4.3 - Comparison of vertical component seismograms recorded in the borehole with vertical records from the two surface stations nearest the borehole. Note the impulsive nature of the P and the S wave arrivals, the high frequency content, and the relative lack of scattering or coda in the borehole records with respect to the surface records.

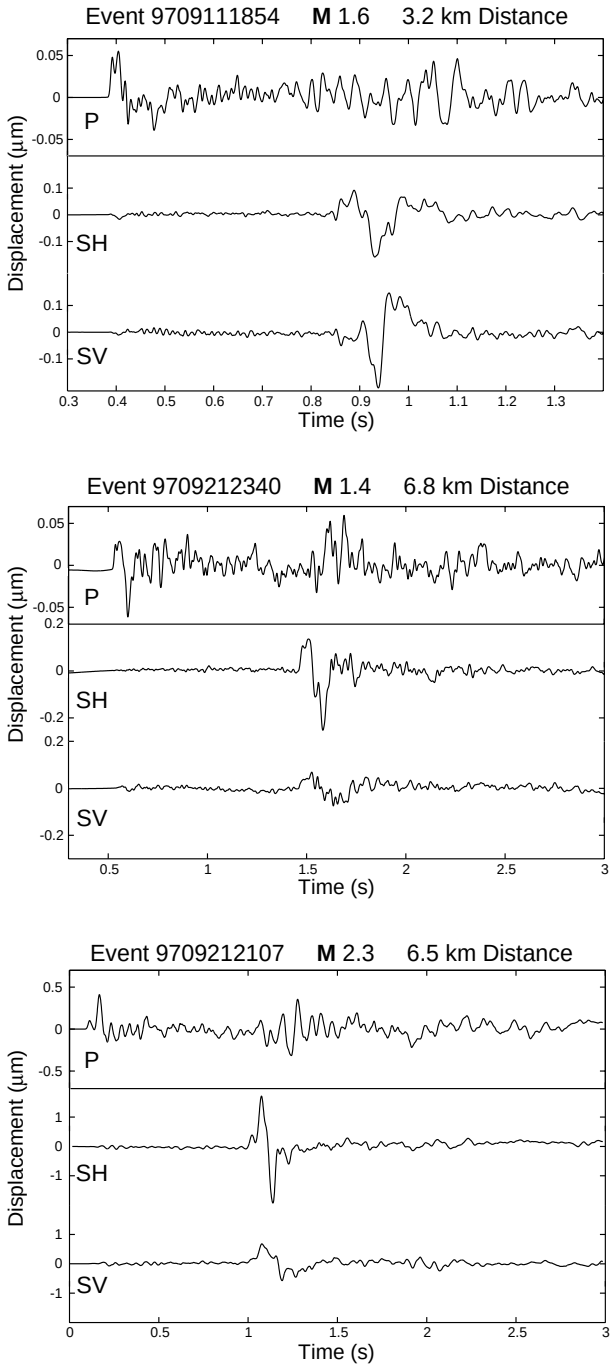

Figure 4.4 – Examples of complex velocity pulse shapes. The SH and SV arrivals are plotted on the same scale. Notice that the P pulses are narrower than the S pulses, indicating that the S waves have lower corner frequencies than the P waves.

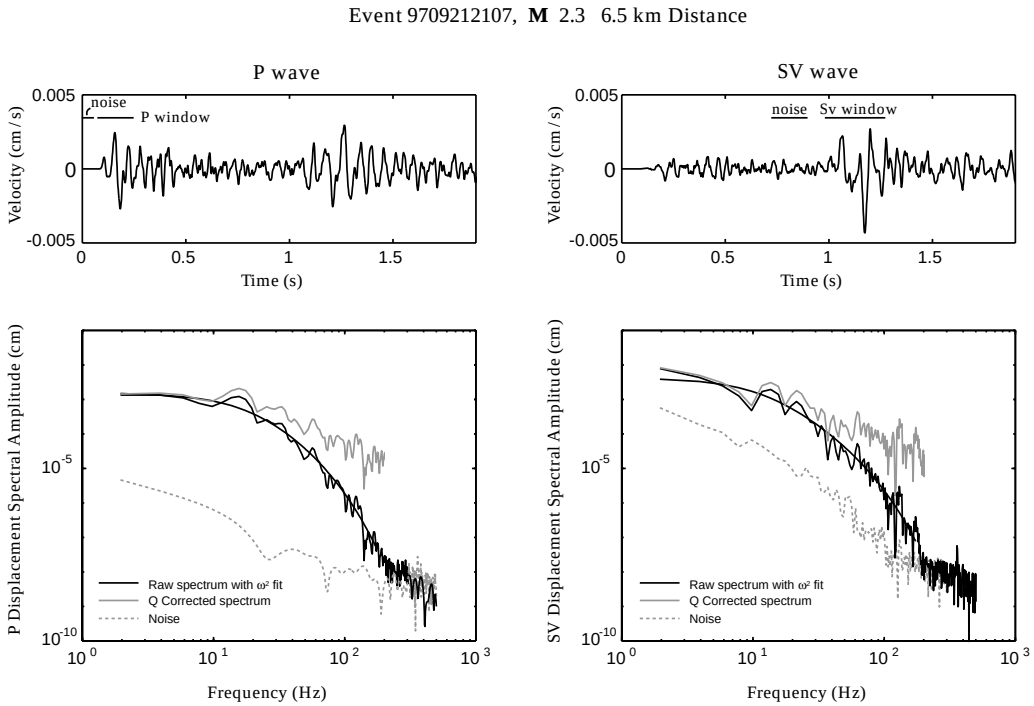

Figure 4.5 - Example of frequency domain processing for event 9709212107. The windows used to find the P and S spectra and the noise spectra (gray dashed lines) are shown in the time domain seismograms. The signal is above the noise (black dashed line) to about 200 Hz. The model fits for the P and S displacement spectra (fitting w^2 spectral shape, W_o, f_o, and Q) are shown in black lines. The resulting Q corrected spectra that are integrated to find the energy are shown in gray.

Some studies of the Long Valley caldera region suggest that many earthquakes have volcanic signatures and cannot be accurately described as simple tectonic earthquakes with pure double couple moment tensors. These studies are based on non double couple focal mechanism solutions (Julian et al., 1999), low frequency dominated and harmonic spectra (Cramer and McNutt, 1997; Hough et al., 2000), moment tensor solutions with significant volumetric expansion and waveforms with long source processes (Dreger et al., 2000). The earthquakes

documented in these studies might reflect the movement of magma that is intruding into the caldera, as surface deformation suggests (Langbein et al., 1995). The November 22, 1997 swarm is an example of a magmatically influenced swarm and is discussed in detail in Chapter 5.

The spectra of earthquakes described in this chapter, however, are characterized by flat low frequency responses below the corner frequency and rapid fall off above the corner frequency without distinct spectral peaks often associated with magmatically influenced earthquakes (Figure 4.5). Therefore, these earthquakes appear to be typical tectonic events, occurring in relatively cold brittle crust. To eliminate earthquakes with a non double couple source from our data set, we have only included events which have P, SH, and SV wave amplitude ratios that are consistent with the amplitudes predicted by double couple moment tensors. Although spectral shapes are consistent with the ω^2 source model (Brune, 1970), high frequencies decay significantly faster than is predicted by the ω^2 and ω^3 source models (Figure 4.5) (Haskell, 1964; Aki, 1967; Brune, 1970), implying that attenuation in the caldera basement is damping high-frequency components of the signal. We use this observation to characterize attenuation in the caldera basement rock.

4.4 Method

For each earthquake, we rotated the seismograms into P, SH, and SV components, where P is along the ray path and SH and SV are the horizontal and vertical directions in the ray plane. We measured seismic source parameters for each component in both the time and frequency domains. Preprocessing included extracting 60 Hz noise with a subtractive filter of our design and removing FIR filter effects from the Reftek recordings (Sherbaum, 1996). Spectra are smoothed using a five point trapezoidal operator (Daniell window). All measurements

were corrected for radiation pattern except for the four events without focal mechanisms (Table 4.1). Radiation pattern corrections were determined theoretically from focal mechanisms following Aki and Richards (1980).

4.4.1 *Time Domain Analysis*

In the time domain, we computed seismic moment and seismic energy for P, SH, and SV arrivals using the following relations (Figure 4.6):

$$Mo = \frac{4\pi\rho v^3 r \int u\, dt}{F} \qquad (4.1)$$

$$Es = \frac{4\pi\rho v r^2 \langle F \rangle^2 \int u^2 dt}{F^2} \qquad (4.2)$$

where ρ is density (2.7 gm/cm^3), α is velocity (5.8 km/s and 3.3 km/s for P and S waves, respectively), r is hypocentral distance, <F> is the average radiation pattern (0.52, 0.41, and 0.48 for P, SH, and SV waves, respectively), and F is the radiation pattern correction (Aki and Richards, 1980). We averaged the P and S wave seismic moments for each event and summed P, SH, and SV energies to find the total radiated seismic energy.

We computed the source radius, d, from the width of the P displacement pulse by assuming the rupture duration is equivalent to half the pulse width and

assuming a circular rupture with rupture velocity of 2.6 km / s (0.8*V_s). Following Eshelby (1975), the static stress drop is then

$$\Delta\sigma = \frac{7\ Mo}{16\ d^3} \qquad (4.3)$$

These time domain measurements provide insight into source processes but are not corrected for attenuation. Therefore, they are only used as a consistency check with frequency domain measurements before correction for attenuation.

4.4.2 *Spectral Analysis*

Following Abercrombie (1995), we solve for the spectral level, Ω_o, and corner frequency, f_o, while simultaneously correcting for path-averaged attenuation, Q, by fitting P and S wave spectra with the ω^2 source model (equation 4.4) (Figure 4.5) (Aki, 1967; Brune, 1970).

$$\Omega(f) = \frac{\Omega_o e^{-(\pi f t / Q)}}{\left[1 + \left(f / f_o\right)^2\right]} \qquad (4.4)$$

where t is travel time and f is frequency. We obtained initial model fits for each event by minimizing the L2 norm of the log difference between the observed and modeled spectra. Weights inversely proportional to frequency were used to equalize the influence of all frequency measurements across the log frequency spectrum. A Nelder-Meade simplex algorithm (MATLAB^{TM}) was then applied to determine the best fitting spectral parameters based on the initial model estimate.

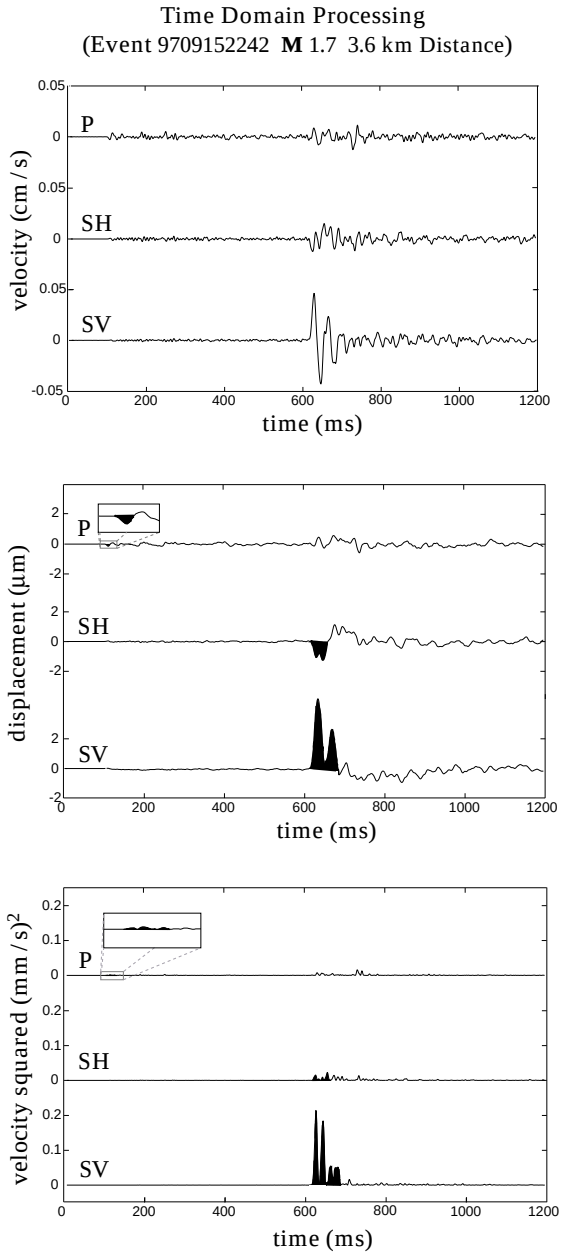

Figure 4.6 - Example of time domain processing for event 9709152242 (see previous figures). The upper plot shows the 3 components rotated into the P, SH, and SV directions. The middle plot shows the rotated seismograms integrated to displacement with shaded areas showing areas integrated in equation 4.1 to find the moment. The lower plot shows the velocity squared records with shaded areas indicating the areas integrated in equation 4.2 to find the seismic energy. Notice how little S energy is lost to scattering on the P component.

We also examined spectral parameters using the ω^3 model (Haskell, 1964), but relative to the ω^2 model the ω^3 model fits most spectra poorly, indicating that the ω^2 model better represents sources in the caldera. For this reason and because we prefer to risk overcorrecting for attenuation rather than undercorrecting, we only report spectral parameters derived from the ω^2 model in this paper. We have not calculated source parameters using models that vary the sharpness of the corner frequency, as done by Abercrombie (1995). Although such models would not significantly change seismic energy measurements, they could affect stress drop estimates. Considering the inherent uncertainty in stress drop estimates (equation 4.3), we believe that the corner frequency calculated with the ω^2 model yields a stress drop estimate within errors.

Since Ω_o is equal to the area under the displacement pulse, we substituted Ω_o for the integral of the displacement pulse in equation 4.1 to obtain the seismic moment for each component. The reported seismic moment is the average of moments obtained from the P, SH, and SV components. Likewise, we substituted the integral of the Q corrected velocity squared spectrum for the time domain integral in equation 4.2 to find the radiated seismic energy, summing the P, SH, and SV components for the total radiated energy. For each event, integrals of the velocity squared spectra were calculated over the entire bandwidth above the noise, typically to 200–300 Hz. For seismic energy determination, each spectrum was integrated over the bandwidth interval from 2 Hz to at least 200 Hz. We determined the source dimension (d) from f_o using the source model of Sato and Hirasawa (1973) and average results for P and S waves (equation 4.5).

$$d = \frac{C v}{2\pi f_o} \qquad (4.5)$$

We estimate C as 1.5 and 1.9 and v as 5.8 km/s and 3.3 km/s is for P and S, respectively.

4.5 Attenuation Correction and Frequency Resolution

Archuleta et al. (1982) observed high frequency spectral decay of ω^4 and ω^5 for earthquakes in the caldera region. In a shallow borehole study Archuleta (1986) later showed that this unusually high decay rate is not caused solely by attenuation in the uppermost 200 m. To improve understanding of attenuation in the caldera region and its effect on source parameter measurements, we used the borehole data to quantify attenuation at depth and near the surface and to investigate the spatial distribution of attenuation. Like many previous studies, we assume constant Q. Although Ide et al. (2001) show that this assumption can lead to underestimates of seismic energy for small earthquakes, the consistency of our approach with previous studies allows us to directly compare seismic source parameters in Long Valley to those found in other regions.

To evaluate attenuation in the upper 2 km of caldera fill we formed spectral ratios between the borehole station and surface stations that lie along the same ray path for a particular source (Figure 4.7). For the selected events, the part of the path between the source and the borehole is virtually identical for both stations, so the spectral ratio reflects only borehole to surface attenuation. Attenuation was determined from the slope (m) of the log spectral ratio: $Q = -\pi t / m$, where t is the travel time. We obtained both Q_p and $Q_s < 40$ in the Bishop tuff, results similar to those of many other studies throughout California that have found low near surface Q (Hauksson et al., 1987; Malin et al., 1988; Aster and Shearer, 1991; Blakeslee and Malin, 1991; Archuleta et al., 1992; Gibbs et al., 1994; Jongmans and Malin, 1995; Abercrombie, 1997).

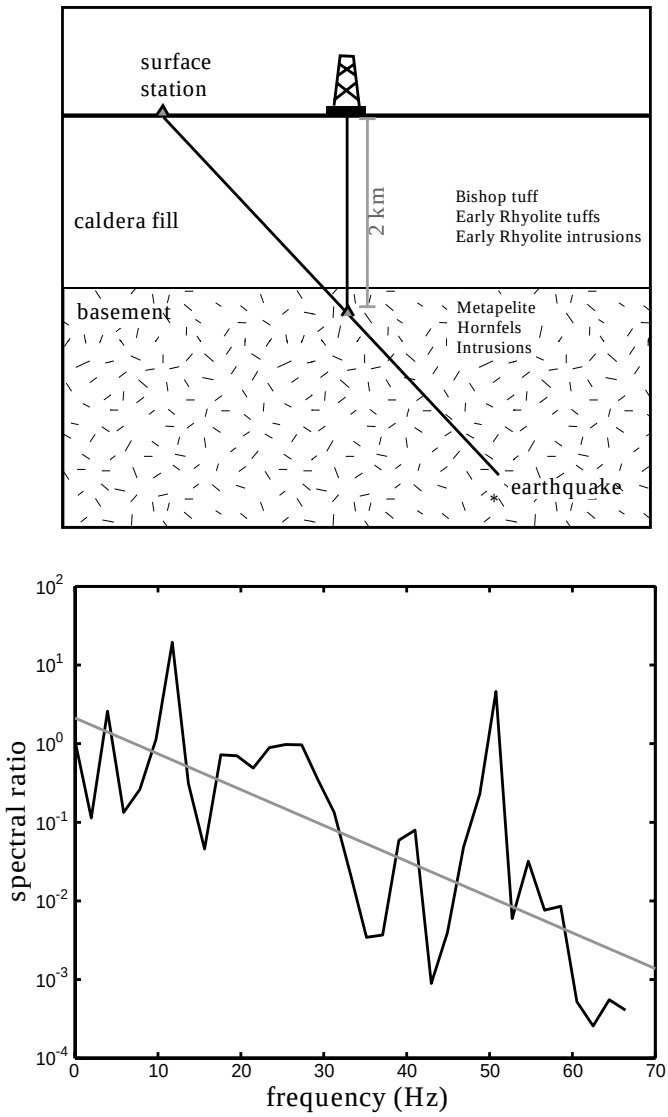

Figure 4.7 - Cartoon of ray path geometry used to estimate attenuation in the upper 2 km of caldera fill (upper panel). Assuming straight ray paths, attenuation between earthquake hypocenter and borehole instrument is common for both stations. Thus, the spectral ratio describes attenuation between the borehole instrument and the surface station. Example spectral ratio (lower panel). Q determined from slope of best fit line through spectral ratio.

Path-averaged Q values obtained from borehole recordings by fitting spectra with the ω^2 source model (equation 4.4) indicate that $Q_s/Q_p > 1$ at seismogenic depths. In dry elastic solids $Q_s/Q_p < 1$ (Knopoff, 1964), but the effects of fluids and scattering can upset this proportionality (Winkler and Nur, 1982; Menke and Dubendorff, 1985). Our result of $Q_s/Q_p > 1$ is consistent with many other studies (e.g. Hough and Anderson, 1988; Abercrombie, 1995; Hough et al., 1999). Since $Q_s/Q_p < 1$ along teleseismic ray paths, attenuation in the upper crust ($Q_s/Q_p < 1$) seems to reflect the differences in the media .

Measured Q values vary from $Q_p \sim 100$ and $Q_s \sim 200$ for earthquakes in the inner caldera to $Q_p \sim 400$ and $Q_s \sim 800$ for earthquakes south of the caldera. The Q results imply that attenuation varies spatially, with strong attenuation occurring in the inner caldera in the region of the borehole seismometer. This is consistent with the conclusion of Sanders and Nixon (1995), who image a low Q_s anomaly beneath the resurgent dome of the caldera based on S to P amplitude ratios. Our data indicate that ray paths between the borehole and south eastern dome have particularly strong attenuation. The resulting Q model is shown in Figure 4.8.

Q measurements indicate that correcting the seismograms for attenuation is extremely important for measuring seismic source parameters of small to moderate sized earthquakes in the Long Valley area, even when the sensor is at 2 km depth in basement rocks. Singh and Ordaz (1994) showed that frequencies up to six times the corner frequency are required to correctly measure 80% of the radiated seismic energy for a source with an ω^2 source spectrum. Larger events in this data set have reliable frequency resolution up to 60 times the corner frequency. When the radiated energy for these events is calculated with the spectra truncated at 6 times the corner frequency, approximately 80% of the total energy is recovered, verifying the theory. Thus, seismic energy can be seriously miscalculated if

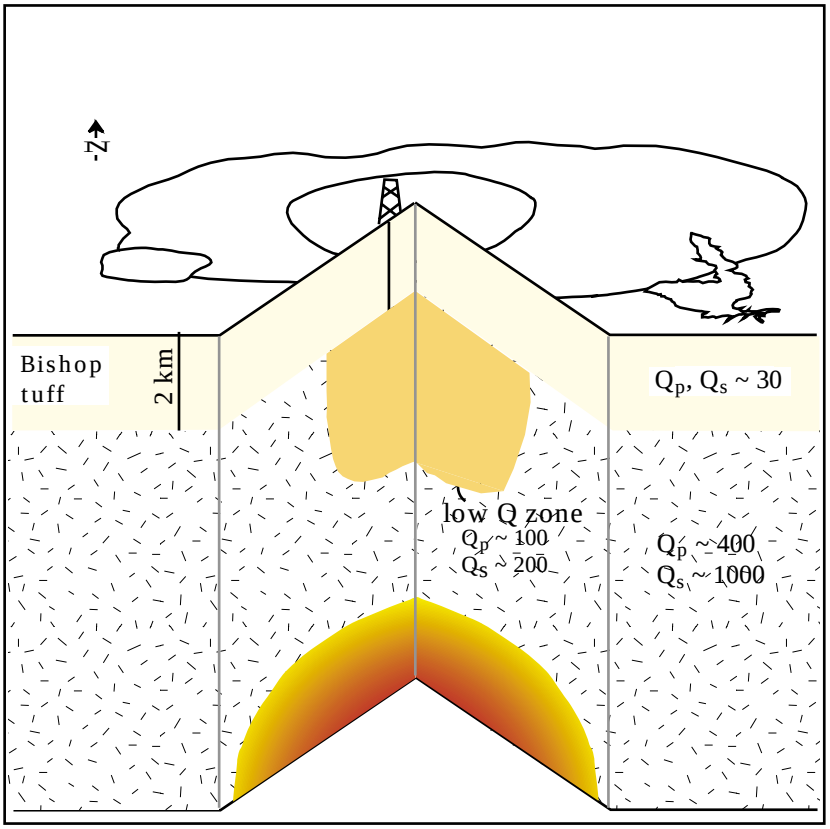

Figure 4.8 - Cartoon of the general three zone Q model inferred from earthquake spectra. Near surface attenuation is very high (Qp and Qs <30). Intracaldera attenuation is ~4 times higher than attenuation in the surrounding basement rock. Path averaged Q measured for individual earthquakes is described in Figure 4.11.

attenuation is underestimated or ignored, especially for small earthquakes. All of our data with the exception of three small earthquakes (9709210331, 9709230631, 9709240150) have frequency resolution from 1 Hz to at least f_o*6 for the S wave spectra. Since almost all of the seismic energy is radiated by S waves, we expect to have robust seismic energy estimates.

Under-correction for attenuation could also make the corner frequencies of small earthquakes appear inordinately low, leading to anomalously low stress drop estimates (Hanks, 1982); Anderson and Hough, 1984; Anderson, 1986). Archuleta (1986) concluded that the stress drop scaling breakdown for small earthquakes observed in the caldera region is not an artifact of attenuation in the upper 200 m. However, our measurements indicate that attenuation at depths greater than 200 m is the cause of the previously proposed stress drop scaling breakdown.

4.6 Source Dimension Scaling and Faulting Characteristics

Stress drops calculated from corner frequencies of attenuation corrected spectra using the circular source model of Sato and Hirasawa (1973) range from 0.02 MPa to 26 MPa (Figure 4.9, Table 4.2). This range of stress drops is consistent with many other studies, including Archuleta et al. (1982) and Abercrombie (1995). We see no evidence for a change in stress drop with moment in the caldera (Figure 4.9), supporting the results of researchers (Hanks, 1982; Anderson and Hough, 1984; Anderson, 1986; Abercrombie, 1995) who conclude that the stress drop scaling breakdown and apparent minimum source dimension observed by some authors (e.g. Archuleta et al., 1982) is an artifact of high frequency loss resulting from attenuation.

Due to the dependence of equation 4.3 on rupture dimension cubed, stress drop estimates are strongly model dependent. For example, the Brune (1970) and Madariaga (1976) circular source models would change our S wave stress drops by factors of 1.2 and 0.71, respectively. Whereas a unilateral rupture model which included directivity could change stress drop estimates by up to a factor of 6. Complexity and variety of seismic sources in the caldera, which are revealed by the elaborate shapes of P and S wave arrivals in the high-frequency borehole

seimograms (Figure 4.4), indicate that any simple source model such as those previously mentioned cannot accurately describe all events in this data set. We believe that the pulse shapes reflect the source as well as the path because 1) the P and S waves have the same shape (Figure 4.4) and 2) events which have almost identical ray paths display a variety of pulse shapes. Consequently, inherent model uncertainties dictate that individual stress drop calculations are order of magnitude estimates.

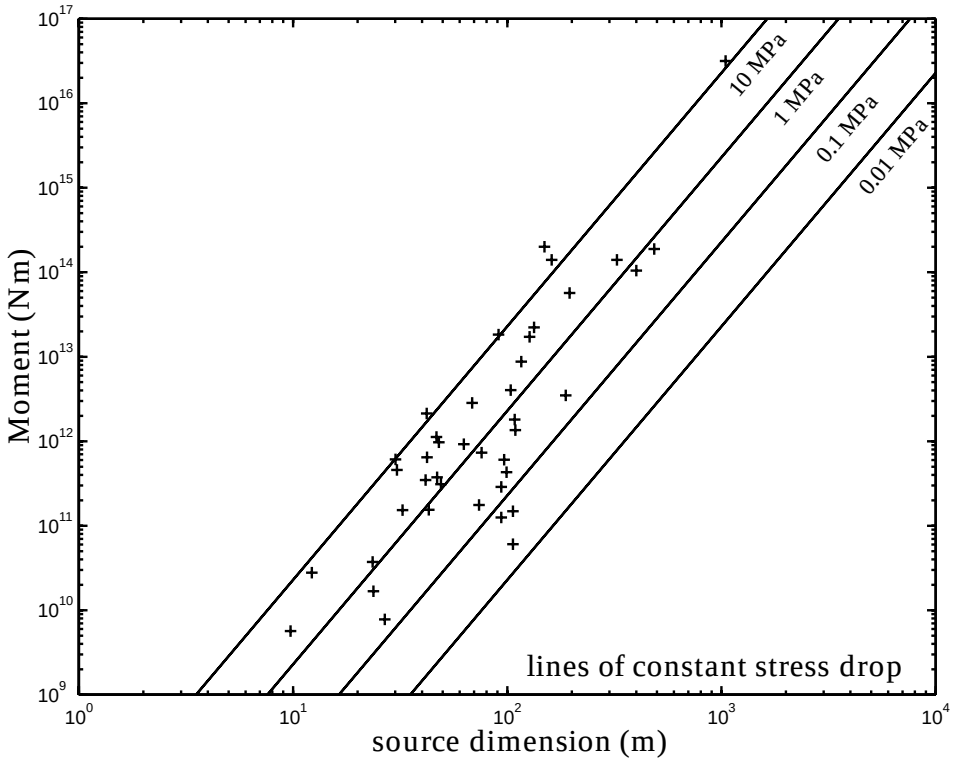

Figure 4.9 - Seismic moment versus source dimension, showing lines of constant stress drop.

Table 4.2
Source Parameter Results

Event	M	Mo (N-m)	Es (J)	σ_a (MPa)	d (m)	$\Delta\sigma$ (MPa)	P width (s)	P f_o	S f_o	Qp	Qs	Q zone
9701111854	1.6	3.11E+11	4.28E+04	0.004	49	1.2	0.045	49	14	55	117	II
9709112323	1.9	7.32E+11	1.04E+06	0.04	76	0.7	0.07	23	11	240	504	NA
9709151934	1.8	6.05E+11	2.24E+06	0.11	97	0.3	0.082	17	9	136	235	I
9709152242	1.7	3.74E+11	8.52E+06	0.68	47	1.6	0.016	131	12	100	201	I
9709160251	1.7	4.31E+11	1.72E+05	0.01	99	0.2	0.07	16	9	193	455	II
9709160912	1.5	1.76E+11	9.29E+04	0.02	74	0.2	0.065	14	21	246	223	II
9709170247	1.7	3.47E+11	4.95E+05	0.04	42	2.1	0.06	46	19	72	138	I
9709172200	2.8	1.83E+13	1.18E+09	1.94	91	11	0.07	23	32	288	427	NA
9709201047	2.0	1.12E+12	4.29E+06	0.11	47	4.8	0.08	28	23	276	374	NA
9709210331	0.8	1.68E+10	5.16E+04	0.09	24	0.5	0.04	43	67	150	217	II
9709210949	1.9	9.21E+11	2.91E+06	0.09	63	1.6	0.042	18	21	110	140	I
9709211614	2.4	4.03E+12	2.81E+07	0.21	104	1.6	0.07	13	10	105	160	I
9709211620	1.2	6.06E+10	5.14E+04	0.03	106	0.02	0.08	16	8	251	292	I
9709211659	1.4	1.25E+11	6.43E+05	0.15	94	0.07	0.08	16	10	259	292	NA
9709211856	2.1	1.81E+12	6.97E+06	0.12	108	0.6	0.063	19	7	126	162	I
9709211910	1.8	6.10E+11	1.54E+07	0.76	30	9.8	0.05	84	23	94	170	I
9709211915	1.0	3.72E+10	9.92E+04	0.08	24	1.3	0.03	70	37	103	166	I
9709212050	2.9	2.23E+13	2.87E+08	0.38	133	4.1	0.075	14	6	89	130	I
9709212102	2.0	9.71E+11	1.45E+07	0.45	48	3.9	0.04	48	15	83	149	I
9709212107	2.3	2.84E+12	3.09E+07	0.33	69	3.9	0.11	26	12	88	147	I
9709212115	1.7	4.58E+11	2.42E+07	1.58	31	7	0.06	104	21	80	160	I
9709212301	1.4	1.53E+11	4.80E+05	0.09	32	2	0.025	81	21	137	555	III
9709212340	1.4	1.55E+11	4.97E+05	0.1	43	0.9	0.07	46	18	68	194	I
9709220213	1.8	6.45E+11	1.13E+07	0.53	42	3.8	0.061	79	15	105	166	I
9709230130	2.2	2.13E+12	1.16E+08	0.84	42	13	0.06	80	15	77	194	III
9709230256	2.1	1.36E+12	2.13E+05	0.005	109	0.5	0.12	11	11	685	797	NA
9709230326	1.6	2.88E+11	4.74E+05	0.05	94	0.2	0.124	10	21	544	539	NA
9709230631	0.5	5.66E+09	3.52E+04	0.19	10	2.7	0.016	148	100	131	169	I
9709230734	0.6	7.81E+09	7.67E+02	0.003	27	0.2	0.026	60	33	73	108	I
9709240150	0.9	2.79E+10	1.34E+05	0.13	12	6.7	0.024	103	92	129	195	III
9709240911	1.4	1.48E+11	4.20E+05	0.08	106	0.05	0.07	16	8	166	510	II
9711041302	2.3	3.48E+12	1.30E+07	0.11	188	0.2	0.112	8	5	121	204	I
9711071517	3.1	5.68E+13	1.43E+09	0.75	196	3.3	0.18	5	9	79	139	III
9711230219	3.5	1.89E+14	5.22E+08	0.08	485	0.7	0.35	2	4	112	194	III
9802971938	3.3	1.05E+14	1.37E+09	0.39	400	0.7	0.21	3	3	304	612	III
9805240310	2.6	8.75E+12	9.68E+08	3.32	116	2.4	0.08	9	13	211	274	III
9806080355	3.5	2.00E+14	6.00E+08	0.09	149	26	0.19	9	7	143	248	IV
9806090524	5.0	3.16E+16	3.68E+13	34.9	1094	12	0.625	1.3	0.9	299	369	IV
9806090829	2.8	1.72E+13	1.36E+08	0.24	127	3.7	0.11	16	6	210	344	IV
9806090845	3.4	1.40E+14	6.60E+08	0.41	161	15	0.16	9	6	211	162	IV
9806091330	3.4	1.40E+14	2.24E+09	0.48	325	1.8	0.25	10	14	157	286	IV

Zone I Qp = 100, Qs = 200; Zone II Qp = 150, Qs = 280; Zone III Qp = 120, Qs = 270; Zone IV Qp = 200, Qs = 300.

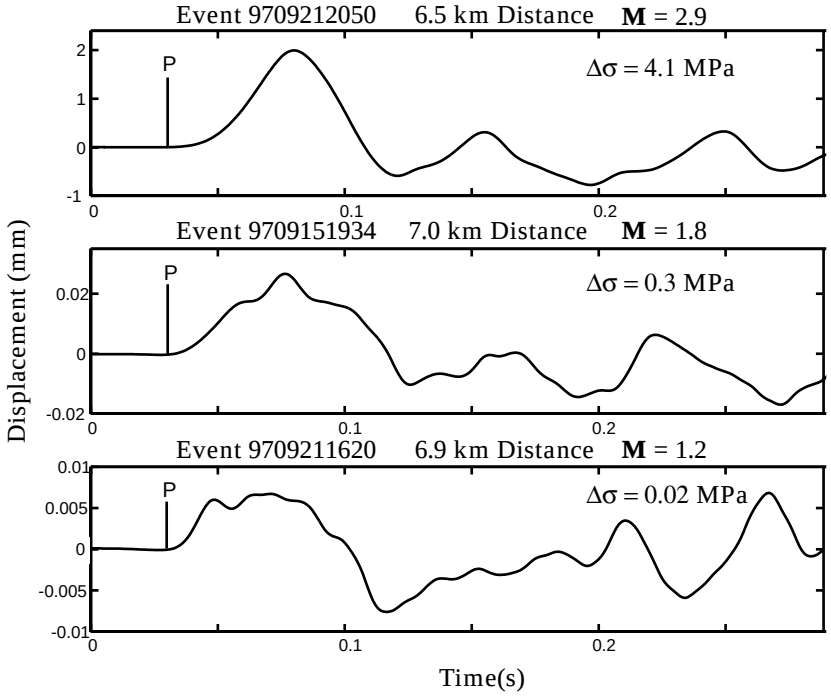

Figure 4.10 - P displacement pulses of three earthquakes of varying moments but equal pulse widths, demonstrating variety in pulse shapes and calculated stress drops. These three events are located in approximately the same place (within 0.5 km of each other). Since they have the same ray paths and the same path effects, variations in pulse shape reflect the source. These events lie along a vertical profile at source dimensions of ~190 m in Figure 4.9.

Figure 4.10 demonstrates the variability and complexity in earthquake source shapes visible in the borehole recordings which lead to scatter in stress drop estimates. The figure shows P displacement pulses of three approximately co-located events (southeast resurgent dome) in order of decreasing magnitude. All three events have roughly equal pulse widths (0.075 s to 0.08 s) and Q corrected corner frequencies (P ~16 Hz, S ~8 Hz), and thus the same interpreted

source dimension (~100 m). Since the seismic moments of these three events range over almost three orders of magnitude, the events represent a vertical profile in Figure 4.9, showing a diversity of stress drop estimates for a source dimension of ~100 m. If the high frequency complexity of the two smaller events in Figure 4.10 is a source effect, these could be multiple events, in which case we are underestimating stressdrops for the subevents and might be underestimating the stress drop for the total event, depending on how the final slip in configured. The observed complexity in Figure 4.10 could also be influenced by the path, in which case the true source might have a simple shape consistent with our model. This example shows that some of the very low stress drop estimates might result from application of consistent spectral fitting techniques rather than natural phenomena. In subsequent analysis on the data studied in this chapter, Ide et al. (2001) show that if longer time windows are used, corner frequencies are better constrained, and the scatter in stress drop is lower.

4.7 Radiated Seismic Energy Scaling

To calculate radiated seismic energy, we correct spectra for attenuation using a regionalized Q model that averages Q values determined by the best fitting ω^2 model for individual events in each region. The model defines zones in the caldera which have similar Q values and averages Q within each zone, thereby eliminating outlying measurements in the same proximity (Figure 4.11, Table 4.2).

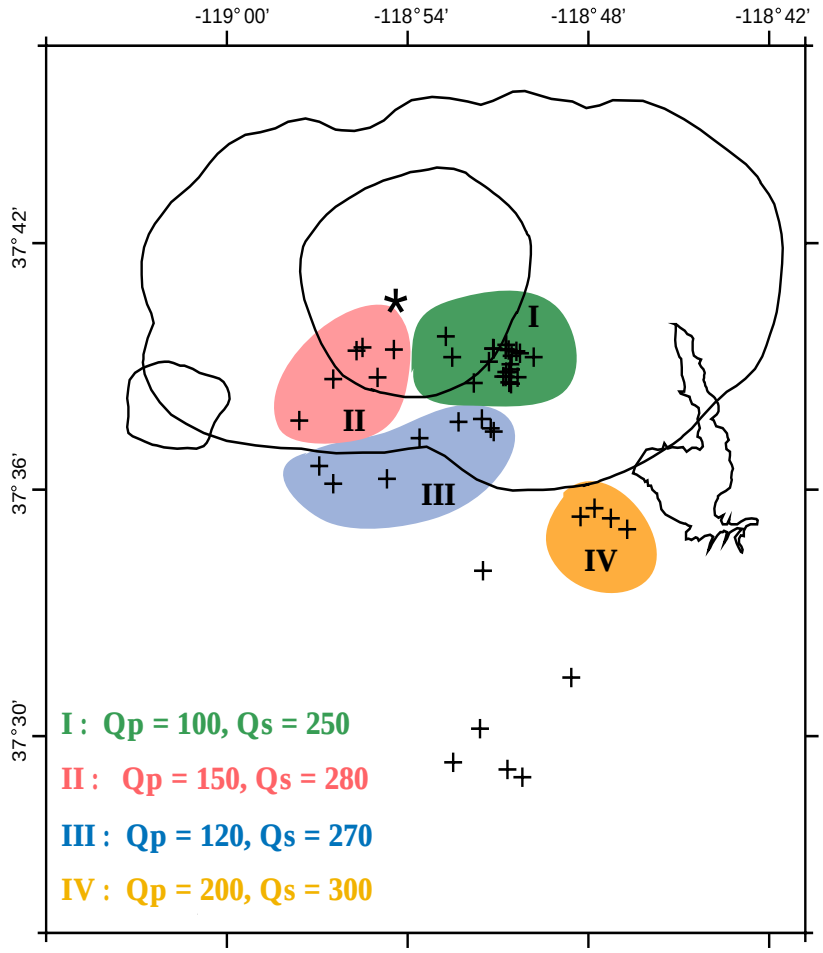

Figure 4.11 - Map showing path-averaged Q zones used to correct spectra for seismic energy estimates. Q zones were obtained by averaging measured Qs for all earthquakes in the region.

We find that radiated seismic energies range from 10^4 J at **M** 1 to 10^{13} J at **M** 5, corresponding to apparent stresses of 0.003 to 30 MPa, assuming $\mu = 3 \times 10^4$ MPa (Table 4.2, Figure 4.12). Figure 4.12 shows seismic energy measurements before and after correction for attenuation (crosses and circles, respectively). Since attenuation affects the smallest events most severely, correcting for attenuation decreases the change in apparent stress with moment. However, like

Abercrombie (1995) and others (e.g. Kanamori et al., 1993; Mayeda and Walter, 1996), we find that apparent stress increases somewhat with increasing moment even after correction for attenuation. When these results are directly compared to the results of other seismic energy studies (Figure 4.13), most of the events have apparent stresses consistent with the range that others have observed (e.g. Abercrombie, 1995). Thus, when analyzed in a manner consistent with other studies, these "tectonic" Long Valley earthquakes appear to be governed by the same processes as earthquakes in non-volcanic areas.

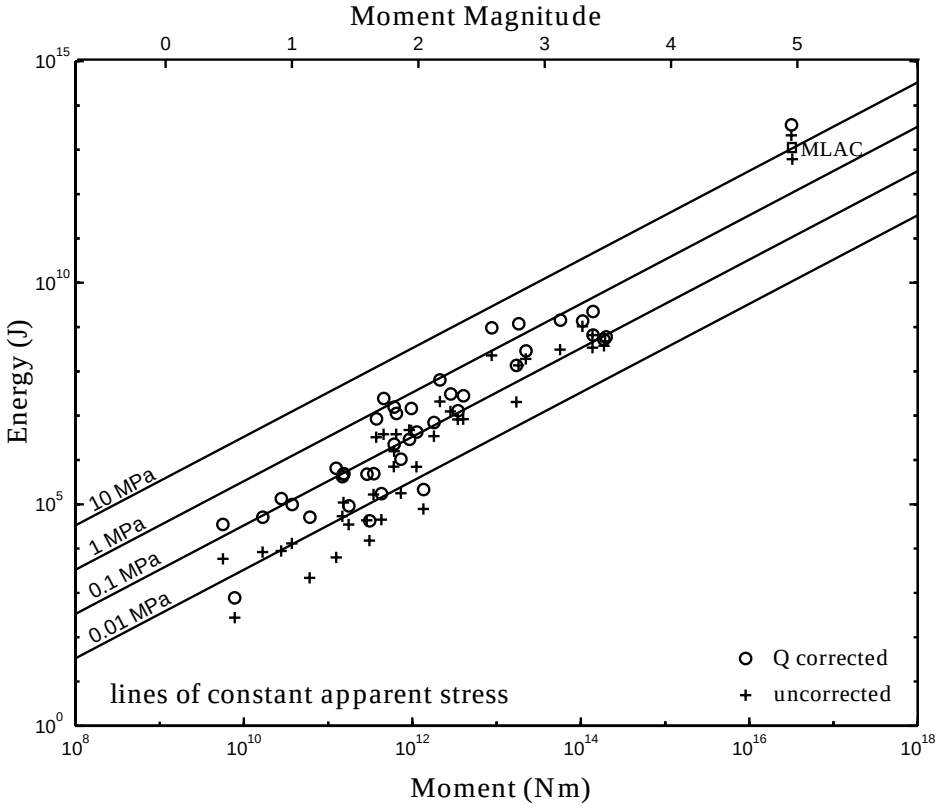

Figure 4.12 - Radiated seismic energy versus seismic moment, showing lines of constant apparent stress. Circles are corrected for attenuation. Crosses are uncorrected. The square is the result obtained for station MLAC to verify borehole measurements of the M 5 event

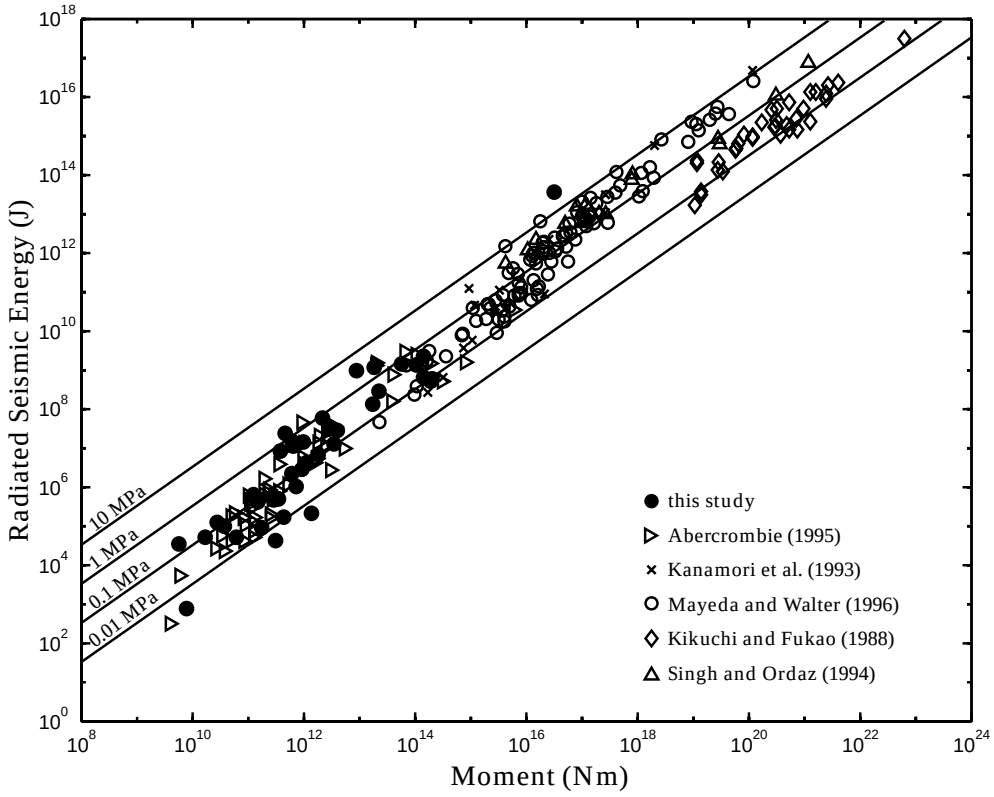

Figure 4.13 – Compilation of seismic energy measurements from both near source and teleseismic studies.

The change in apparent stress with moment appears to occur in these data at about the **M** 2 magnitude range. Above **M** 2, earthquakes appear to scale in a self-similar fashion, with the possible exception of the largest, **M** 5, earthquake (Event 9806090524), which is discussed in more detail below. However, by reanalyzing these data Ide et al. (2001) show that the energy estimates for the smaller earthquakes in our data set (< **M** 2) are underestimated due to unmodeled path effects. Thus, like stress drop, apparent stress appears to follow constant scaling, implying that all earthquakes are equally efficient.

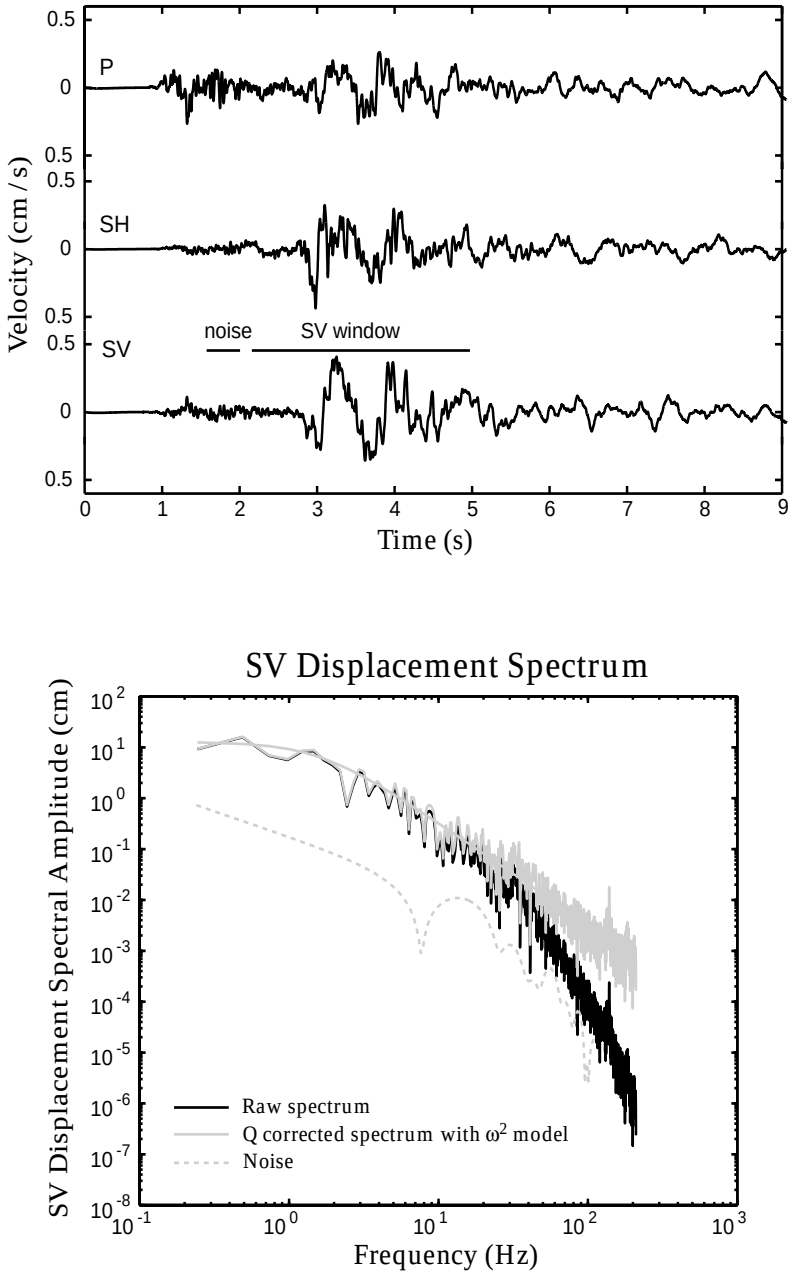

Figure 4.14 - Rotated velocity seismograms from the borehole and SV displacement spectrum for event 9806090524.

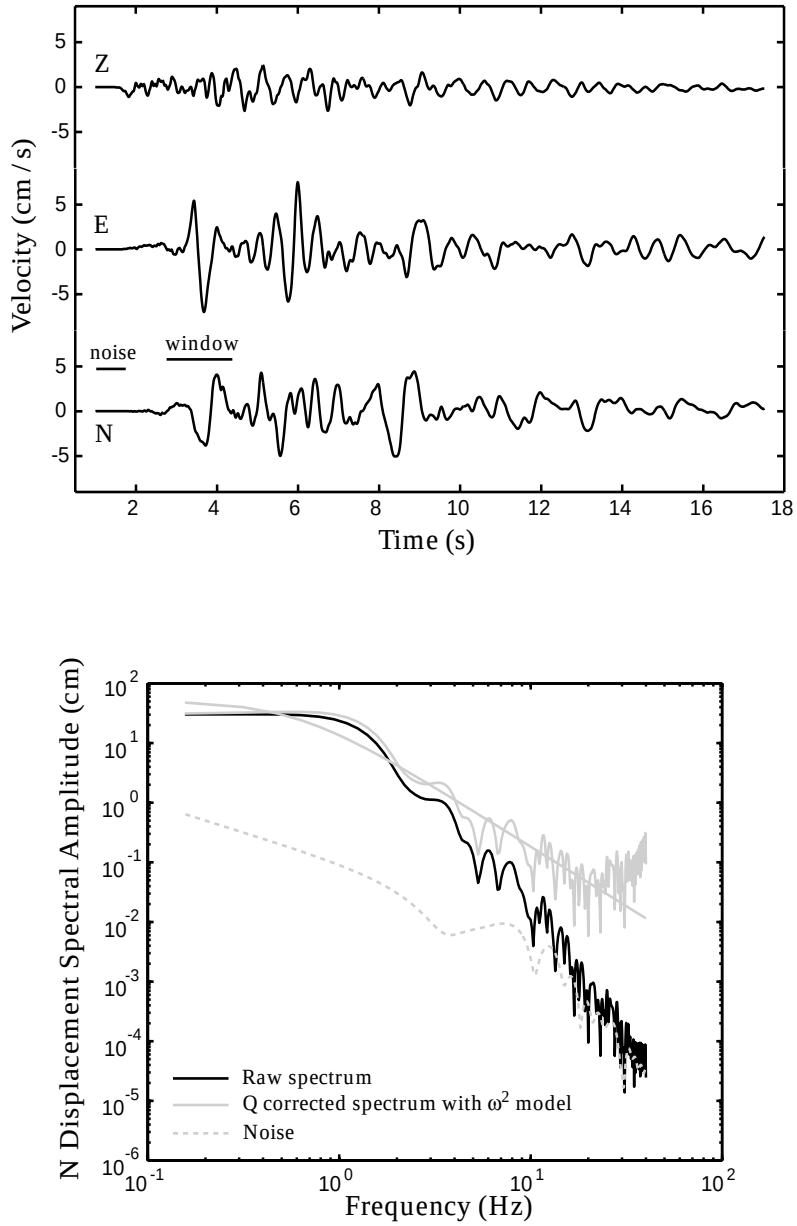

Figure 4.15 – Surface seismograms and S displacements spectrum for the N component for event 9806090524, as recorded on the force-balance accelerometer of the TERREscope station, MLAC, operated by Caltech. Note that the bandwidth is limited at high frequencies to 10 Hz, as compared to a high frequency bandwidth extent of 100 Hz at the borehole station (Figure 14).

Because the **M** 5 earthquake is an anomaly in our results, we now describe this event in detail. Figure 4.14 displays the borehole seismograms and SV spectrum for the **M** 5 earthquake. Signal is well above the noise for over 7 octaves above the corner frequency (0.9 Hz). Therefore, the spectra should give a robust estimate of the total radiated seismic energy. However, source parameters computed at a single station could be biased by rupture propagation effects, such as directivity. As a consistency check we found source parameters for this event at a nearby surface accelerometer, MLAC of the Caltech TERREscope network (Figure 4.15), which is located 8 km from the hypocenter (Figure 4.1). Seismograms and the S displacement spectrum for the N component are shown in Figure 4.15. The MLAC analysis yields an apparent stress of approximately 10 MPa, a factor of 3 lower than the borehole estimate (Figure 4.12). Thus, seismic energy as determined from the borehole data may be overestimated due to rupture propagation effects.

4.8 Stress and Seismic Efficiency

To estimate shear stresses at depth and seismic efficiencies (fraction of energy that is radiated seismically or the ratio of apparent stress to shear driving stress) for earthquakes in the caldera, we combine Coulomb faulting theory with knowledge of the state of stress in the caldera. Focal mechanism stress inversions and borehole breakout analyses indicate that the caldera region is a strike-slip to normal faulting environment (Moos and Zoback, 1993). Assuming hydrostatic pore pressures, a coefficient of friction of 0.6, and a vertical stress equal to the overburden pressure, the Coulomb failure criterion predicts a maximum shear stress of 40 MPa in a normal faulting environment ($S_V > S_{HMAX} > S_{HMIN}$) and 70 MPa in a strike-slip faulting environment ($S_{HMAX} > S_V > S_{HMIN}$), assuming $S_2=S_V=(S_1+S_3)/2$) at the average hypocentral depth of these events (7 km).

By examining a variety of laboratory and earthquake data sets in a broad range of lithology types and faulting environments, McGarr (1998) observes that seismic efficiency is less than or equal to 6%. Most of our events have seismic efficiencies consistent with this conclusion (Figure 4.16). However, the **M** 5 earthquake (Event 9806090524) discussed previously has an unusually high seismic efficiency of >15 % based on the driving stress analysis and energy measured in the borehole and at the surface station MLAC.

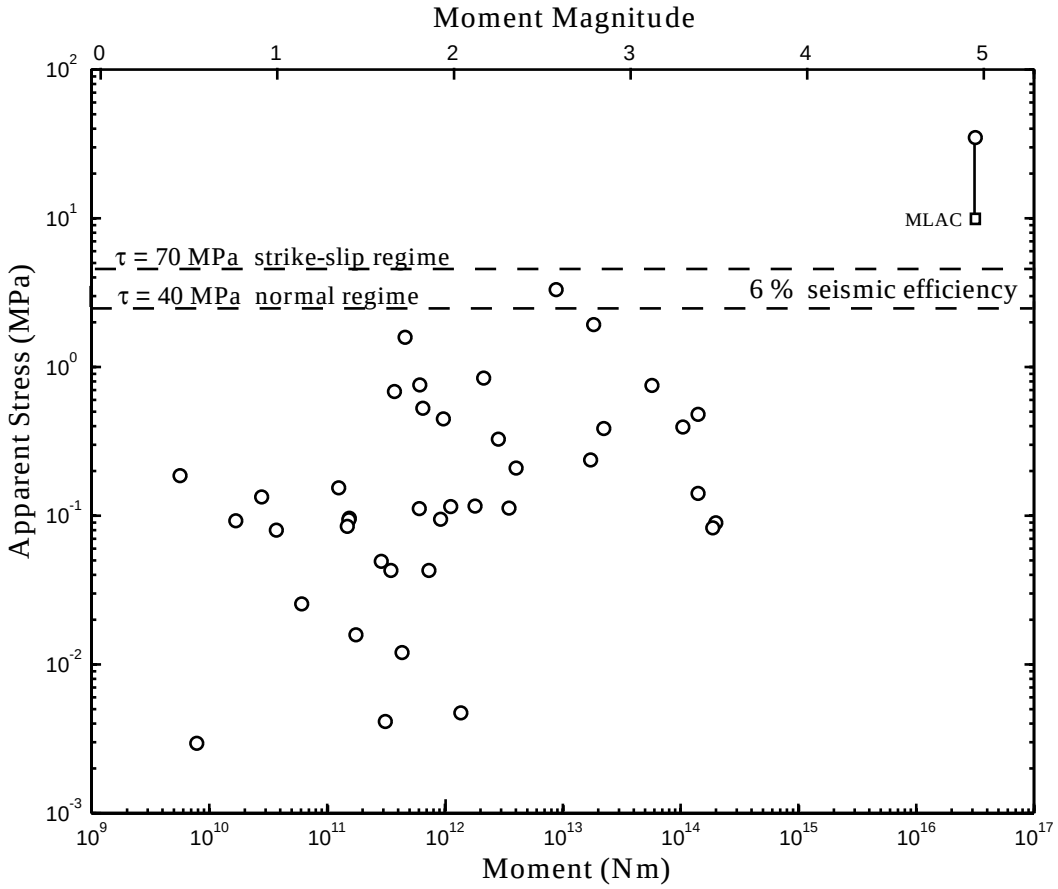

Figure 4.16 – Apparent stress versus seismic moment, showing the bounds of 6% seismic efficiency for shear driving stresses of 40 to 70 MPa.

4.9 Summary

We find that both static stress drops and apparent stresses range from roughly 0.01 MPa to 30 MPa for earthquakes of **M** 0.5 to **M** 5 in the Long Valley caldera and the adjacent Sierra Nevada block, based on a constant Q model. Attenuation is significant in the basement rock of the caldera (path averaged Q_p = 100 to 400, Q_s = 200 to 800). Therefore, correcting for attenuation is essential to avoid underestimating the stress drops and seismic energies of small events. Stress drops are roughly constant over the entire magnitude range studied (Figure 4.9), and apparent stress appears to be constant down to **M** 2 (Figure 4.12). Ide. et al. (2001) show that constant apparent stress continues down to ~ **M** 0.5 when additional path effects are accounted for. Based on tectonic driving stresses of 40 - 70 MPa at the depth of faulting in the caldera, as inferred from Coulomb faulting theory, apparent stress estimates lead to seismic efficiencies that are consistent with McGarr (1999) of less than or equal to 6% for most events analyzed.

Although this study was later shown by Ide et al. (2001) to produce results which are partially contaminated by path effects, particularly for earthquakes < **M** 2, it is important to note that when using source parameter analysis techniques consistent with other studies, tectonic-type Long Valley earthquakes appear to be governed by the same processes as earthquakes in other non-volcanic regions.

Acknowledgments

We would like to thank Satoshi Ide and Greg Beroza for greatly improving this work. We are grateful to Don Rock, Phil Harben, and Paul Kasameyer of Laurence Livermore National Laboratory for installation of their seismometer and Reftek recording system and Hisao Ito and Takao Ohminato of the Geological Survey of Japan for installation of their Kinkei recording system. Peter Malin of Duke University and Stuart Wilkinson of the USGS provided invaluable assistance in the field, and Peter Malin graciously shared the data from his temporary surface array. We would also like to thank Mark Zoback, Art McGarr, Nicholas Deichmann, Rachel Abercrombie, and an anonymous reviewer for their enlightening comments and constructive reviews.

Chapter 5

EVIDENCE FOR FLUID-DRIVEN SEISMICITY IN THE LONG VALLEY CALDERA

A shorter version of this chapter will be submitted for publication with Mark Zoback, Bill Ellsworth, and David Hill as coauthors to the *Journal of Geophysical Research*.

5.1 Abstract

The Long Valley caldera in eastern California was in a state of strong unrest in late 1997 and early 1998. During this time period, uplift of the caldera's resurgent dome due to the intrusion of magma deep within the caldera (Langbein et al., 1998; Battaglia et al., 2000) was accompanied by unusually high rates of seismicity in the south moat of the caldera and the release of carbon dioxide along the flanks of Mammoth Mountain (McGee et al., 2000). Although the majority of earthquakes that occurred during this period were brittle, double-couple events, a few earthquakes, including one **M** 4.9 and two **M** 4.6 events, appear to have had significant dilatational components in their source processes, which have been interpreted as evidence for magmatically-induced fluid injection (Dreger et al., 2000).

To understand better one particular swarm and the possible role of fluids in faulting, we relocated November 22, 1997 seismicity using a double-difference algorithm (Waldhauser and Ellsworth, 2000). The resulting high-resolution locations reveal that the November 22 seismicity initiated at the lower eastern corner (9 km depth) of the western south moat seismic zone and migrated ~4 km upward and westward along the fault zone away from the initiation region at a rate of ~0.05 m/s. Several aspects of the earthquakes and earthquake seismograms imply that fluids were involved in the source processes of some of the earthquakes in the migration sequence. Analysis of the focal mechanisms in context of the local stress field suggests that pore fluid pressure was extremely high during this migration sequence. These combined observations strongly suggest that seismicity on November 22, 1997 was triggered by a fluid or a pressure transient associated with magmatic intrusion at depth within the caldera.

5.2 The 1997–1998 Long Valley Caldera Crisis

The most recent episode of marked unrest in the Long Valley caldera occurred in mid 1997–early 1998 after more than a year of quiescence (Figure 5.1). This episode began in May 1997, when the rate of expansion of the caldera's resurgent dome increased due to the intrusion of magma beneath it (Langbein, 1998; Simons et al., 2000). One month later, seismic swarms began in the south moat of the caldera (Figure 5.2). Rates of resurgent dome uplift and south moat seismicity increased throughout 1997 until they peaked on November 22, 1997. On that day alone, the caldera experienced 2 mm of uplift across its resurgent dome (Hill et al., in press), 3 **M** 4.6 and greater earthquakes, and more than 1000 **M** 1.2 and greater earthquakes.

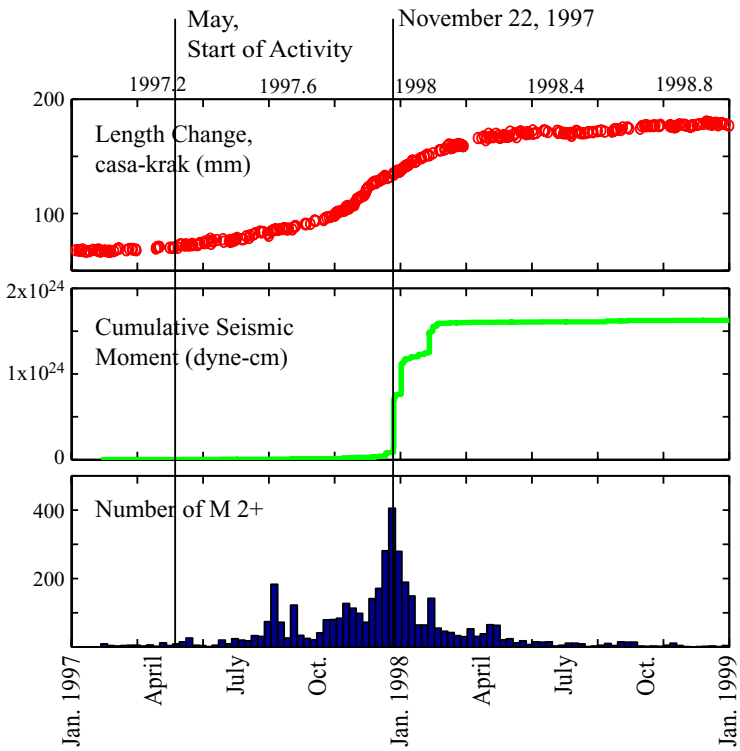

Figure 5.1 - Activity in the 1997–1998 episode: deformation across the casa-krak baseline (upper panel, see Figure 5.2 for baseline location), cumulative seismic moment (middle panel), and histogram of number of magnitude 2 and greater earthquakes (lower panel).

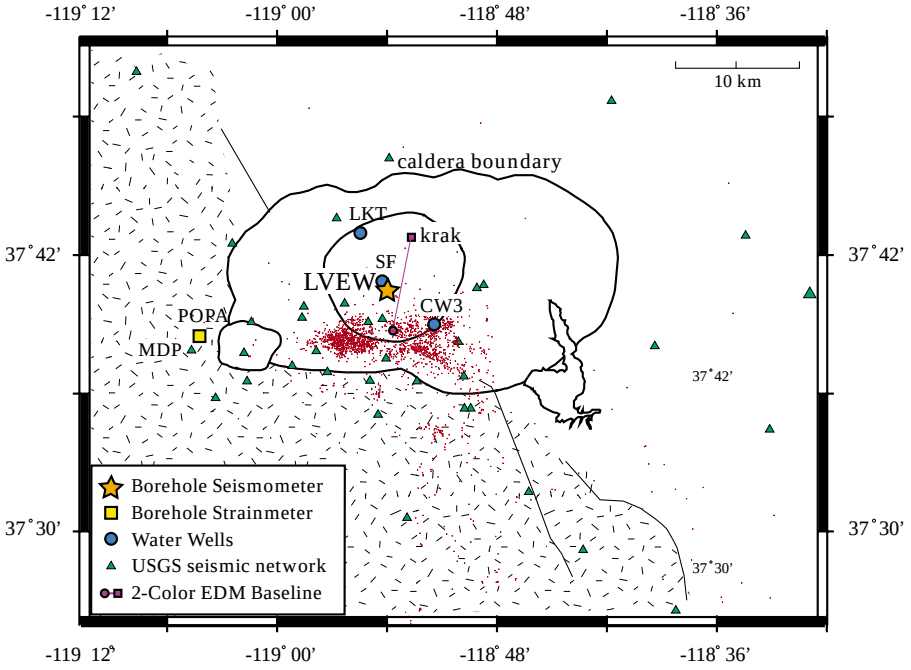

Figure 5.2 - Map of the Long Valley area showing locations of seismographs, water wells, and selected geodetic instruments. Red dots are epicenters of M 2 and greater earthquakes from the 1997–1998 swarms.

At ~17:20 UTC, the time of the **M** 4.9 earthquake, on November 22, 1997 (the second of the 3 **M** 4.6+ earthquakes) the beginning of an unusual transient compressional strain signal was observed at the Devil's Postpile borehole strainmeter (POPA) (Dreger et al., 2000) and three water wells located inside the caldera recorded unusual water level changes (Roeloffs et al., 1999) (Figure 5.3). When combined with other deformation data, the POPA and water level data suggest that fluid which had been intruding into the caldera in 1997, moved rapidly into the south moat beginning on November 22, 1997 (Langbein et al., 1998; Roeloffs et al., in preparation) at roughly the time of the **M** 4.9 earthquake. Following November 22, 1997, activity decreased, and by March 1998, deformation and seismicity had returned to background rates (Figure 5.1). The caldera has been relatively quiet since that time.

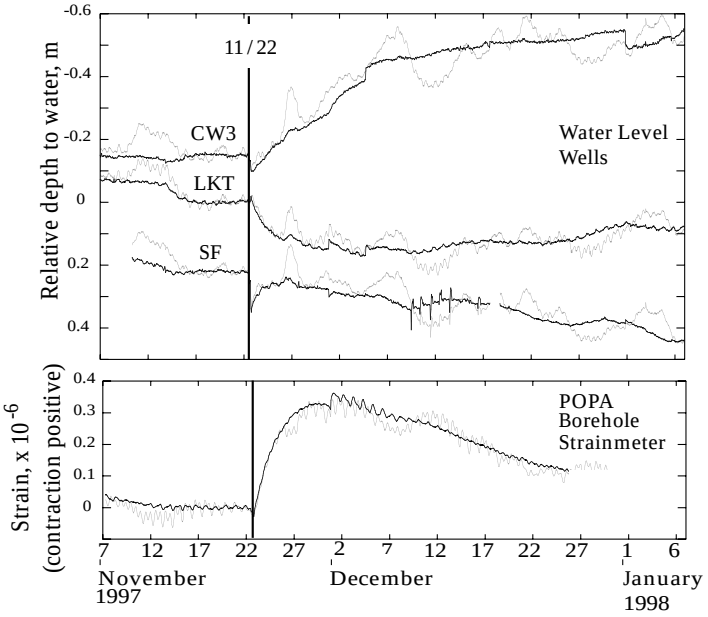

Figure 5.3 - Water level changes (upper panel) and strain changes (lower panel) associated with 1997–1998 activity. Gray lines are raw data. Black lines are corrected for tides and atmospheric pressure effects. Figure courtesy of Evelyn Roeloffs.

5.3 Critical Questions About the Development of Crisis Episodes

Inflation of the resurgent dome generally appears to precede an increase of seismicity in Long Valley caldera deformation episodes. This suggests that magmatic intrusion may trigger south moat seismicity during periods of caldera unrest. However, south moat earthquakes do not appear to slip in response to a stress field caused by magmatic intrusion beneath the resurgent dome. Rather, they appear to slip in response to tectonic stresses (see Chapter 3), though earthquake swarms may be triggered by magmatic intrusion. This observation leads to an important question: What are the specific mechanisms by which magmatic activity triggers earthquakes?

Close examination of the 1997–1998 episode provides insight into this

question. The three **M** 4.6+ earthquakes on November 22, 1997 had significantly non-double-couple (NDC) moment tensor solutions (71%, 34%, and 27% double-couple, respectively, and 27%, 33%, and 29% isotropic, respectively) (Dreger et al., 2000). The isotropic components of the moment tensor solutions imply that opening occurred across the faults during shear failure (shear failure is represented by the double-couple components of the moment tensor solutions). Based on these observations, Dreger et al. (2000) suggest that on November 22, 1997, high pore fluid pressures triggered earthquakes and magmatically-derived fluids intruded into faults during shear failure.

Although their study provides insight into the processes associated with faulting during the 1997–98 episode of unrest, the non-double couple moment tensors observed on November 22, 1997 are mechanically problematic. Planes opening in mode I failure are oriented perpendicular to the minimum principal stress (Hubbert and Willis, 1957; Ode, 1957). Planes failing in shear, however, must be oriented at some angle to the minimum principal stress so that there is shear stress acting across the fault plane. It follows that in a crustal volume containing many faults of varying orientations, shear deformation and opening would not occur simultaneously on the same planar fault unless the fault is segmented and consists of planes of various orientations (Baer, 1991). Thus, to better understand the November 22, 1997 seismicity, we must answer two critical questions: 1. How does magmatic activity trigger faulting? 2. How do shear failure and opening appear to occur nearly simultaneously?

In this chapter, we describe in detail the development and waveform characteristics of seismicity on November 22, 1997. Based on these observations, we address the two questions listed above and suggest a possible scenario for deformation and seismicity in November 1997.

5.4 Temporal/Spatial Development of the 1997–1998 West South Moat Seismic Swarms

In order to observe the spatial and temporal development of seismicity in the 1997–1998 Long Valley caldera seismic episode, we relocated these earthquakes using the double-difference algorithm, *hypoDD* (Waldhauser and Ellsworth, 2000; Waldhauser, 2001) and P-wave arrival times from the Northern California Seismic Network (see Chapter 2). To further improve resolution of November 22, 1997 earthquake locations, we included high-quality P-wave arrival time picks from the Long Valley Exploratory Well (LVEW) in the relocations for 671 earthquakes on this day. Relocated hypocenters for the 1997–1998 swarms are shown in Figure 5.4, color-coded with respect to time.

The majority of seismic moment release in the 1997–1998 seismic episode and in previous seismic episodes occurred in the west south moat seismic zone (WSMSZ) (see Chapter 2). This is the only region of the caldera where discrete planes cannot be inferred from hypocenter locations (Figure 5.4). Rather, the earthquake locations reveal that the west south moat seismic zone is a ~1 kilometer-wide near-vertical fault zone composed of many small faults. We designate this fault zone WSMSZ1.

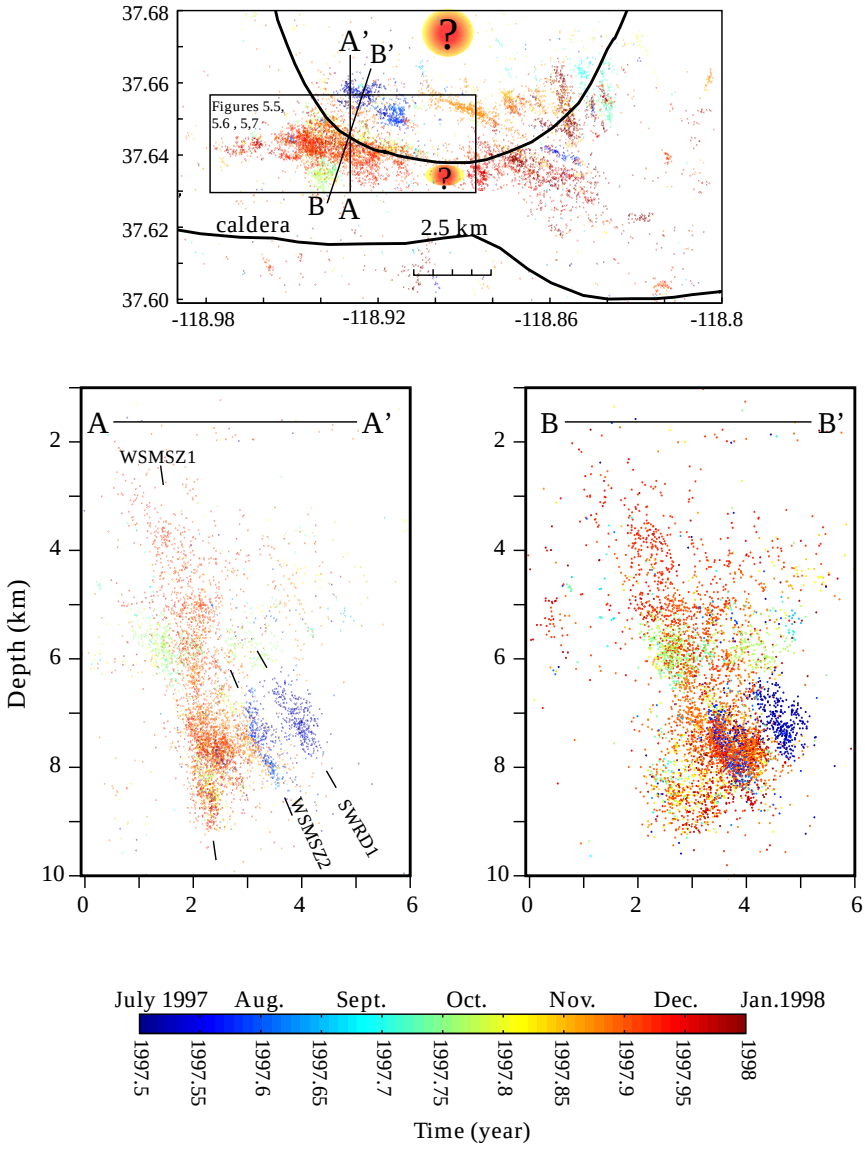

Figure 5.4 - Map view (upper), N / S cross section (lower left), and N17E / S17W cross section (lower right) of seismicity in 1997–1998, color-coded with respect to time. Question marks indicate possible magmatic inflation sources during this time (Langbein et al., 1998, Battaglia et al., 1999). Box designates area of Figure 5.5.

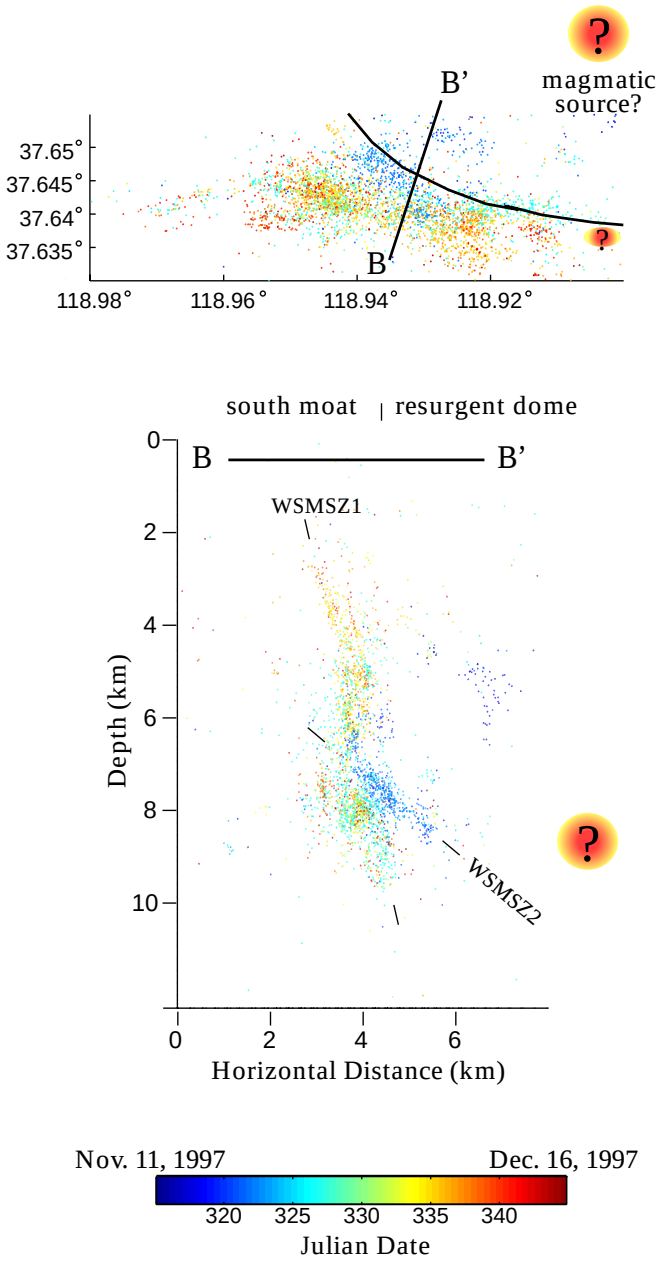

Figure 5.5 - Map view (upper) and N17E/S17W cross section (lower) of west south moat seismicity in mid-November through mid-December 1997, the most seismically energetic month of the 1997–1998 episode, color-coded with respect to time. Question marks indicate possible magmatic inflation sources during this time (Langbein et al., 1998, Battaglia et al., 1999). Figure 5.4 shows location of this figure.

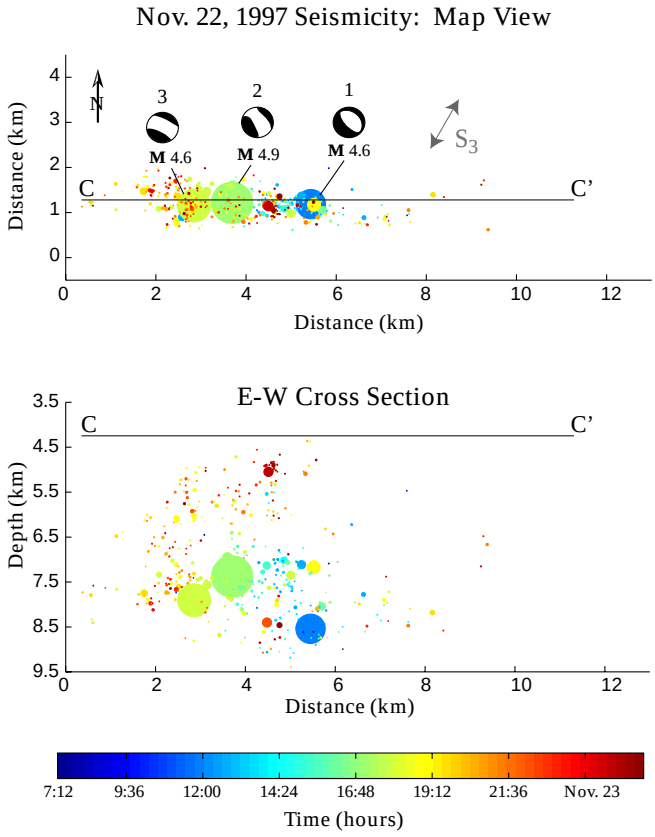

Figure 5.6 - Map view (upper) and east/west cross section (lower) of seismicity on November 22, 1997. Earthquake symbols are scaled with moment. The upper panel shows moment tensor solutions for three **M** 4.6 and greater events (Dreger et al., 2000) and the direction of minimum compressive stress (see section 5.6).

The 1997–1998 seismic swarm began in July 1997 on relatively deep (7-9 km), north-dipping faults (WSMSZ2, SWRD1) that splay outward from the base of the WSMSZ1 fault zone (blue earthquakes in Figure 5.4). It is important to note that these structures are oriented such that they may form connecting pathways between WSMSZ1 and a probable source of magmatic intrusion beneath the resurgent dome, as identified by Langbein (1989), Langbein et al. (1995), Marshall et. al (1997), Langbein et al. (1998), and Battaglia et al. (1999). WSMSZ2 and

SWRD1 continued to be active into September 1997. In late September, earthquakes began to occur in a 2 km wide volume around the WSMSZ1 fault zone (green earthquakes in Figure 5.4). Seismicity rates increased in early-mid November and the small fault WSMSZ2 again hosted the most of the seismicity (blue earthquakes in Figure 5.5). As the swarm progressed into late November, seismicity again shifted into the kilometer-wide zone of WSMSZ1 (Figure 5.5), which then hosted the November 22, 1997 earthquakes.

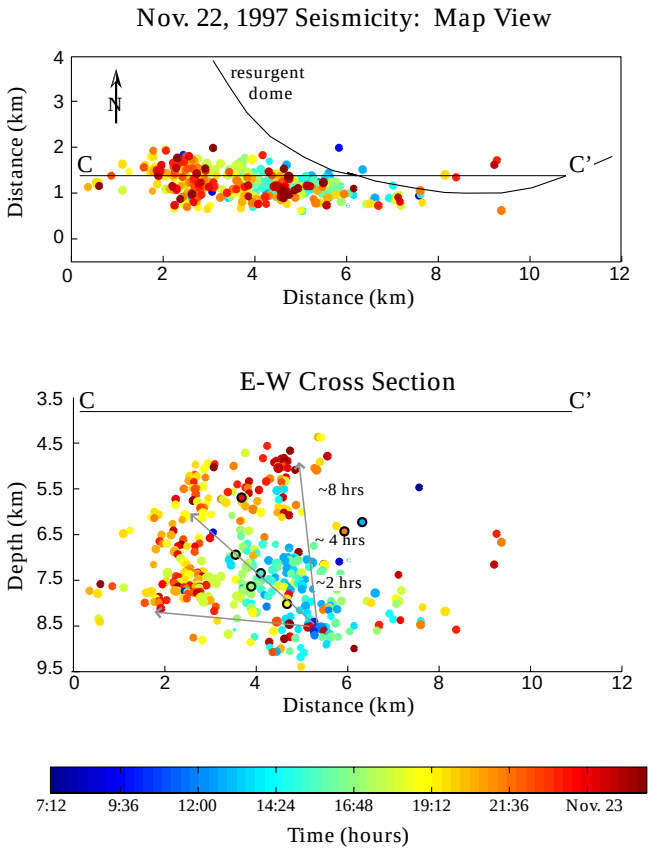

Figure 5.7 - Map view (upper) and east/west cross section (lower) of seismicity on November 22, 1997. Earthquake with black borders in lower panel have an unusually emergent source, as discussed in section 5.5.2.

The November 22, 1997 hypocenters are shown in Figure 5.6, scaled according to magnitude. On this day, seismicity initiated at the lower eastern corner (9 km depth) of the western south moat seismic zone near the time of the first NDC **M** 4.6 earthquake and near the time of the possible south moat intrusion described in section 5.2. In the following 23 hours, the hypocenters of seismicity migrated ~4 km upward and westward along the fault zone away from the initiation region at an average rate of ~0.05 m/s, forming a pattern of radially-expanding earthquake hypocenters (Figures 5.7).

5.5 Distinctive Earthquakes

In order to understand better the nature of faulting in the 1997–1998 Long Valley seismic episode, we examined characteristics of waveforms recorded at 2 km depth in the LVEW (see Chapter 4) and at surface stations. Unlike, the "tectonic" earthquakes described in Chapter 4, many earthquakes in the November 1997 WSMSZ swarm appear to have been magmatically-influenced. In addition to the NDC focal mechanisms associated with the 3 **M** 4.6+ earthqauakes on November 22, 1997, unusual characteristics of this swarm include spasmodic bursts, slowly emergent events, and low frequency events. No harmonic tremor was observed, however.

5.5.1 *Spasmodic Bursts*

Spasmodic bursts are characterized by many "tectonic" brittle-failure earthquakes of about the same magnitude occurring in rapid-fire succession with overlapping coda (Figure 5.8). West south moat seismicity in November and December of 1997 contained many spasmodic bursts and had a relatively high b-value of 1.21.

Spasmodic bursts were relatively infrequent in the west south moat seismic zone before mid-November, 1997. In mid-November through December spasmodic bursts were common. They were most frequent and most vigorous on November 22. On this day ~70% of earthquakes ruptured in spasmodic burst sequences. The spasmodic bursts shown in Figure 5.8 occurred several minutes before and after the **M** 4.9 NDC earthquake on November 22, 1997.

Spasmodic bursts have been observed previously in the Long Valley area in the 1989 Mammoth Mountain swarms (Hill et al., 1990) and in the caldera's south moat in 1980–1982 (Ryall and Ryall, 1983), but explanations for them are highly speculative. The observation that spasmodic bursts occur in geothermal areas (Nitsuma et al., 1985) strongly implies that they are related to fluid movement. Hill et al. (1990) suggest that spasmodic bursts can be thought of as an "unzipping" of subadjacent faults due to a transient increase in pore-fluid pressure along a fault zone.

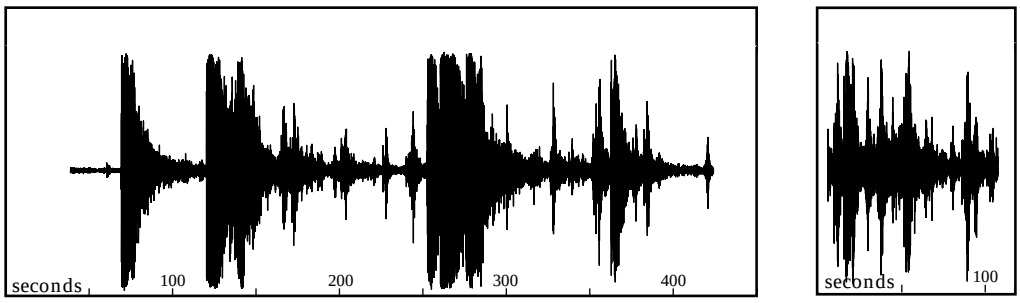

Figure 5.8 - Seismograms recorded at surface station MPD (see Figure 5.2) showing spasmodic bursts. The record shown in the left panel began ~8 minutes before the **M** 4.9 earthquake. The record shown in the right panel began ~7 minutes after the **M** 4.9 earthquake.

5.5.2 *Unusually Emergent Events*

The great majority of earthquakes in the west south moat seismic zone in 1997–1998 were typical "tectonic", brittle-failure events. However, Figure 5.9 shows examples of earthquakes, including the November 22, 1997 **M** 4.9 NDC earthquake, with extremely long, complex source processes (up to 0.5 s). Events of this type appeared intermittently in the west south moat throughout mid–late November, but were the most common on November 22, 1997, like the spasmodic bursts. Earthquakes with these long, emergent source processes were much less frequent than spasmodic bursts, however. Only ~2% of November 22, 1997 earthquakes displayed these long, emergent source processes.

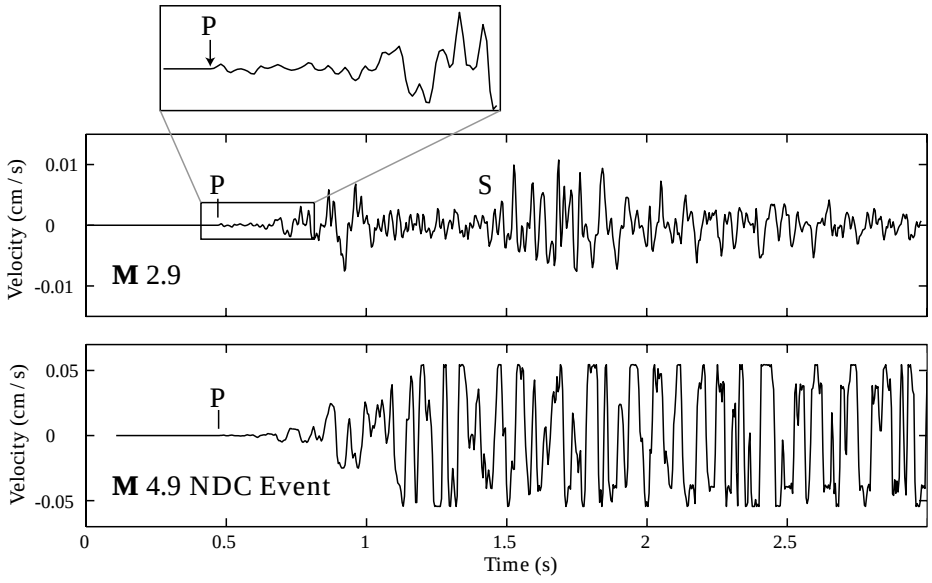

Figure 5. 9 - Seismograms form the LVEW (see Figure 5.2) showing earthquakes with unusually emergent long-duration source processes.

On November 22, 1997 unusually emergent events occurred throughout the core of the seismicity migration zone (Figure 5.7), either contemporaneous with the migrating seismicity front, or shortly following it. Based on the similarity of the waveforms of these emergent events, we infer that the smaller earthquakes of this type must have had source processes similar to that of the **M** 4.9 earthquake. Thus, these slowly emergent earthquakes may also have involved significant dilatation across faults (hydraulic fracturing?) associated with shear faulting.

5.5.3 *Low-Frequency-Enriched Events*

Seismograms recorded in the LVEW indicate that the **M** 2.9 earthquake shown in the Figure 5.9 and many other events in the November 1997 swarm had unusual spectra which were dominated by energy at 10 Hz and lower (Figure 5.10). “Tectonic” earthquakes occurring in the same areas had impulsive P-wave arrivals and had higher frequency content in their comparatively broadband spectra (Figure 5.10). Thus, the relatively low frequency nature of some events was not a path effect. Long period events enriched in 2 Hz energy have been observed previously with surface recordings in the Long Valley area deep beneath the west flank of Mammoth Mountain (Pitt and Hill, 1994). Such low frequency-enriched events are often observed in active volcanic areas, but the explanations for them are somewhat speculative. Likely explanations involve the resonance of fluid-filled channels (Chouet , 1992; Julian, 1994).

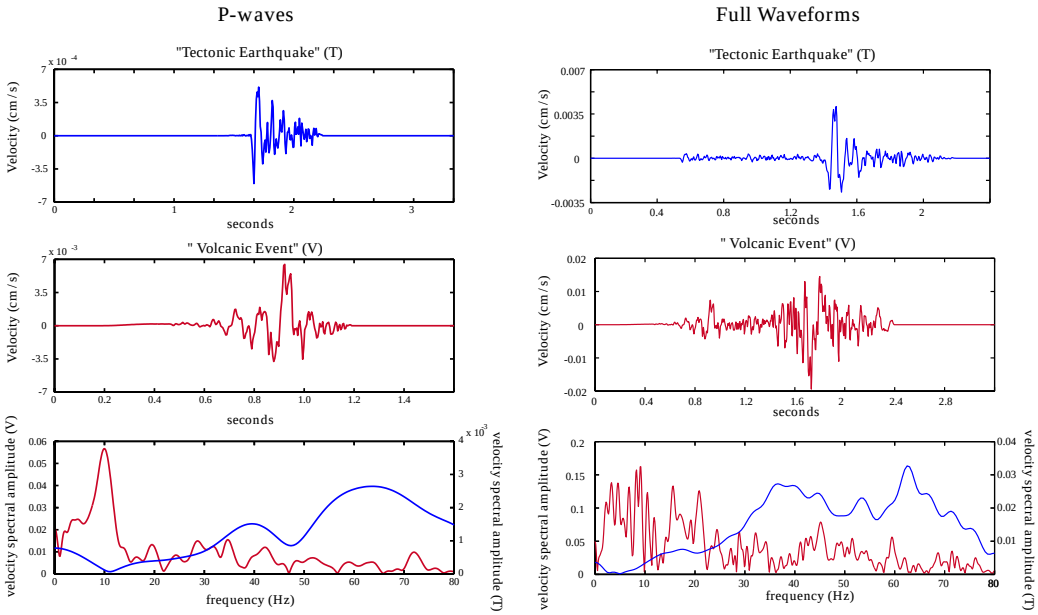

Figure 5. 10 - Comparison of spectra of typical “tectonic” earthquake (blue) with spectra of an unusual low-frequency-enriched event (red), possibly reflecting the movement of fluids. These earthquakes are approximately collocated.

5.6 Stress Analysis and Inferred Pore Pressures

To understand the kinematics of seismicity on November 22, 1997, we selected the best-constrained double-couple focal mechanisms from this day by visual inspection (45 events). Examination of the focal mechanisms in Figure 5.11 reveals that earthquakes in the migrating seismicity swarm on November 22, 1997 occurred on a wide variety of fault planes. It is difficult to reconcile how both normal faulting (Events 1 and 3) and reverse faulting (Events 2 and 4) can occur at nearly the same location (Figure 5.12). The P and T axes distribution from November 22, 1997 focal mechanisms shown in Figure 5.13 demonstrates that these earthquakes can only occur in a uniform stress field if some of the faults are quite weak.

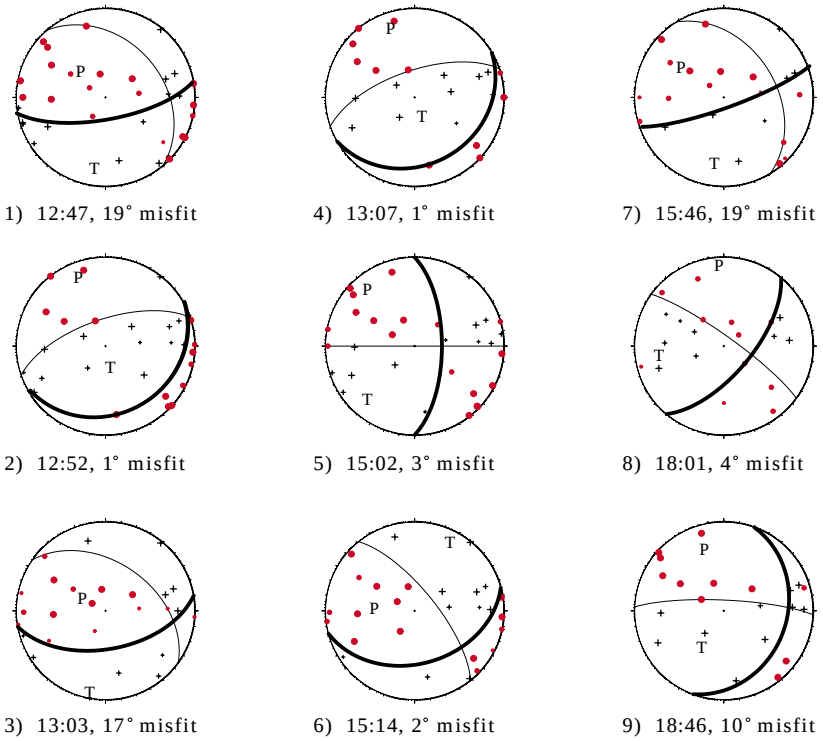

Figure 5.11 - Selected high-quality focal mechanisms from the west south moat seismic zone on November 22, 1997. Red circles designate dilatational first motions. Black crosses designate compression. Thick black lines indicate nodal plane better oriented for failure based on calculated stress field. Captions indicate UTC time of earthquakes and minimum misfit between the observed and predicted slip vector of the two nodal planes based on the calculated stress tensor.

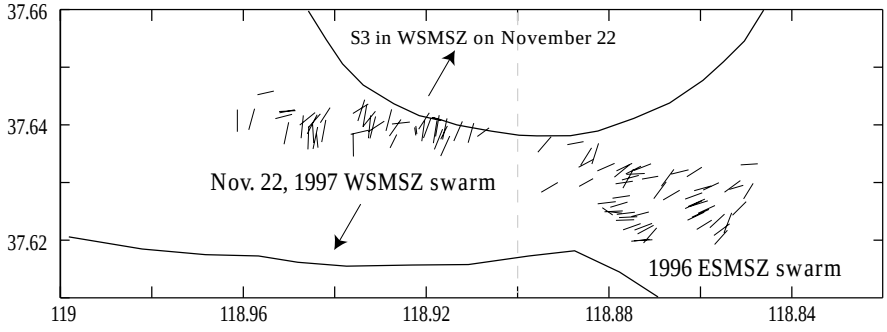

Figure 5.12 - T axes of November 22, 1997 west south moat earthquakes (left) and 1996 east south moat earthquakes (right) for comparison. Line length denotes plunge. Only T axes from well-constrained focal mechanisms (such as those in Figure 5.11) are shown.

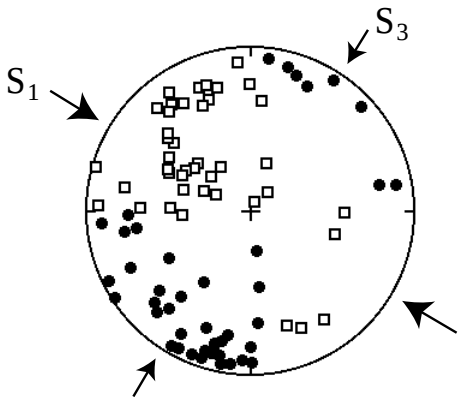

Figure 5.13 - Stereographic projection of P axes (open squares) and T axes (black circles) for well-constrained focal mechanisms from November 22, 1997.

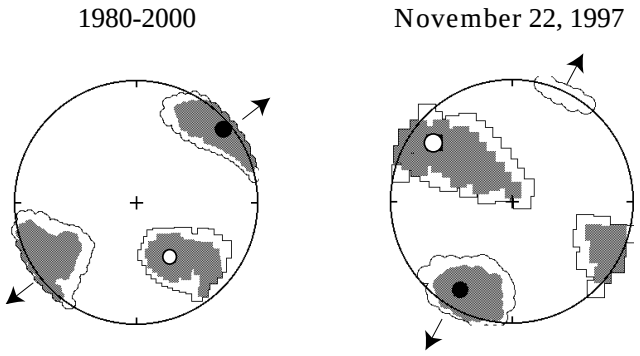

Figure 5.14 - Stress axes results for 1980-2000 (see Chapter) on left and November 22, 1997 on right (S3 = black circle, S1 = white circle). The 68% (white with black outline) and 95% (shaded) confidence regions are shaded. Stereographic plots were constructed using FMSI software (Gephart, 1990).

To investigate the strength of faults in the November 22, 1997 swarm, we determined the orientations and relative magnitudes of the principal stresses on this day in a manner similar to Chapter 3, using the algorithm of Gephart and Forsyth (1984). The focal mechanism stress inversion results indicate that the minimum compressive stress was oriented 210˚, plunging 17˚ on November 22, 1997. This relative extension direction differs from the relative extension direction determined in Chapter 3 for this area based on data from 1980–2000 by ~20˚ horizontally and ~25˚ in plunge (Figure 5.14), although these two stress inversion results are not significantly different at the 95% confidence level. The average misfit to the calculated stress tensor for November 22, 1997 seismicity is generally high at 14˚ (misfit is defined as the minimum angle between the observed and predicted slip vectors for the two nodal planes). However, because the misfit distribution shown in Figure 5.15 does not vary coherently in space, we have no evidence that the stress field in the WSMSZ on November 22, 1997 is heterogeneous over the broad scale.

With knowledge of the stress field on November 22, 1997, we can calculate the shear to normal stress ratios on fault planes which failed in earthquakes on this day. Figure 5.16 shows a normalized 3-D Mohr diagram for November 22, 1997 earthquakes. In Figure 5.16, we assumed that the fault plane for each event was the nodal plane better oriented for failure in the stress field calculated for November 22, 1997. These presumed fault planes are not required to be the planes of minimum misfit determined in the stress analysis.

Based on the Mohr Coulomb analysis, we now investigate the cause of the NDC moment tensor solutions for the three **M** 4.6+ earthquakes on November 22, 1997. The first motion focal mechanism for the first **M** 4.6+ earthquake is poorly determined, yet gives us some indication of the orientation of the fault plane (Figure 5.17). The best oriented failure plane for the first **M** 4.6+ NDC earthquake was

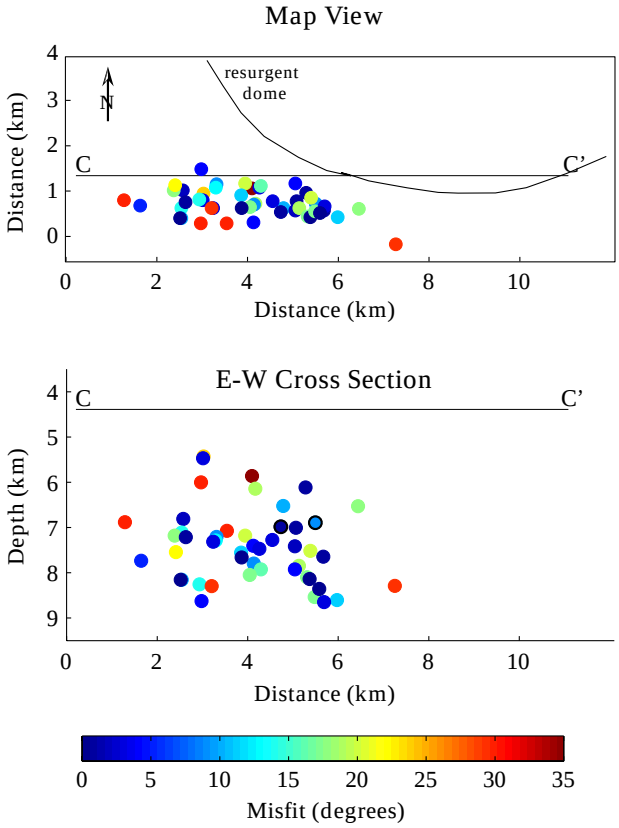

Figure 5.15 - Map (upper) and east / west cross section (lower) showing distribution of misfit to best fitting stress tensor. Misfit is the difference in degrees between the observed slip vector on the nodal plane better oriented for failure and the slip vector predicted for that plane by the best fitting stress tensor. Reverse faulting earthquakes #2 and #4 from Figure 5.11 are outlines in black in lower panel.

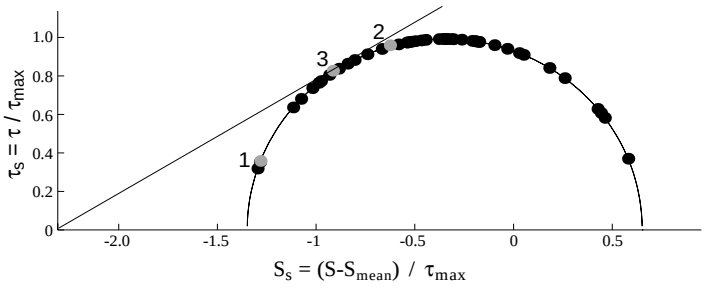

Figure 5.16 - Normalized 3D Mohr diagram of November 22, 1997 failure planes, assuming the nodal plane which is better oriented for failure was the fault plane. The **M** 4.6+ earthquakes are shown with gray dots.

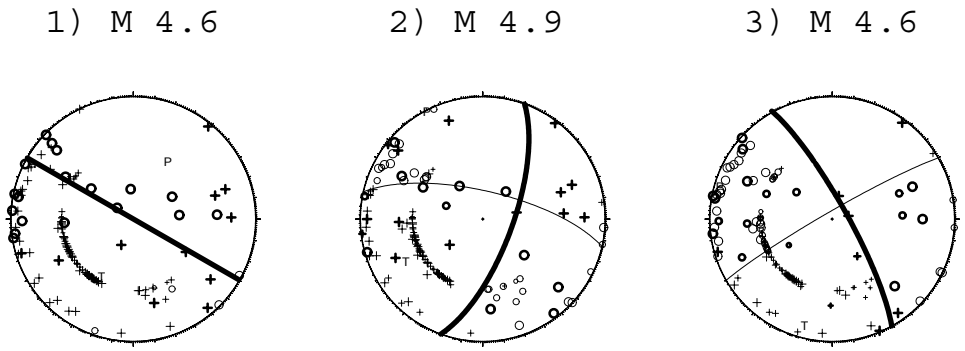

Figure 5.17 - First motion focal mechanisms for M 4.6+ earthquakes. Circles designate dilatational first motions. Crosses designate compressional first motions. Thick line designates more optimally oriented nodal plane.

nearly perpendicular to the least principal stress (Figure 5.16), and therefore little shear stress was acting across the presumed fault plane. This earthquake may have begun as a shear failure event and developed into a hydraulic fracture after the rupture completely relaxed shear stress across the plane.

The second and third **M** 4.6+ NDC earthquakes each have a nodal plane which was very well oriented for failure (Figures 5.16 and 5.17). If the well oriented nodal planes were the fault planes, the Mohr-Coulomb analysis conducted here does not give insight into the cause of the NDC moment tensors for the second and third **M** 4.6+ earthquakes. It is possible that these events may have occurred on interconnected nonparallel cracks as seen by Baer (1991). If this was the case, fault segments oriented perpendicular to the least principal stress would open purely in Mode I failure, while fault segments at other orientations with a shear component acting across the plane may have opened obliquely or in pure shear, resulting in the observed NDC moment tensor solutions.

However, in the case of the **M** 4.9 earthquake (the second **M** 4.6+ earthquake), surface deformation suggesting right-lateral shear across the east-west

trending WSMSZ (Langbein, 1998) and the observation that one nodal plane was oriented parallel to the east-west trending WSMSZ (Figures 5.4 and 5.17) suggest that the more poorly oriented nodal plane was the fault plane. If this is correct, there was little resolved shear stress across the fault plane at the time of failure based on the calculated stress field. Like the first **M** 4.6+ earthquake, this event may have begun as a shear failure event and developed into a hydraulic fracture after the rupture completely relaxed shear stress across the plane

We now use Mohr-Coulomb theory to infer the relative pore pressures necessary to cause failure of earthquakes on November 22, 1997. Based on this theory, failure should only occur on planes whose poles touch the failure envelope for a given coefficient of friction, such as fault A in Figure 5.18. Other faults which are oriented less favorably for failure (B and C for example) must have either a lower effective normal stress (Figure 5.18a) or a lower coefficient of friction (Figure 5.18b) than event A to slip in the same stress regime (Magee and Zoback, 1997). We favor the high pore pressure explanation for the highly diverse focal mechanisms on November 22, 1997 because it is supported by observations of fluid-influenced earthquakes described previously.

Assuming the coefficient of friction is 0.6 on all faults in the WSMSZ, we can thus calculate the minimum pore pressure necessary to cause failure for each event in the November 22, 1997 migrating earthquake sequence, based on Mohr-Coulomb theory and our stress inversion results (FIgure 5.19). For this analysis, we assume that the more optimally oriented nodal plane is the fault plane. In the case where the more optimally oriented nodal plane has a higher cohesion than the less optimally oriented nodal plane (such as when the less optimally oriented nodal plane is an established fault), this assumption may be incorrect and the pore pressure required to cause failure may be higher than is shown in Figure 5.19.

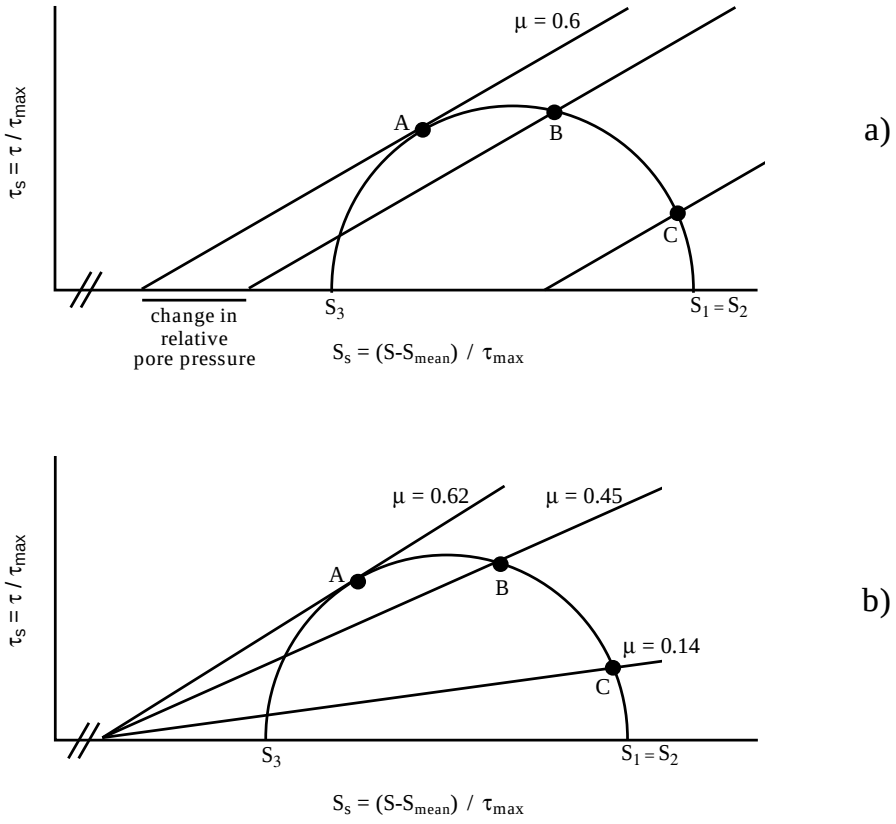

Figure 5.18 - Normalized 3D Mohr diagrams. a) Variation in hypothetical events explained by change in relative pore pressure, assuming constant friction, following Magee and Zoback (1997). b) Variation in events explained by different friction values, assuming constant pore pressure.

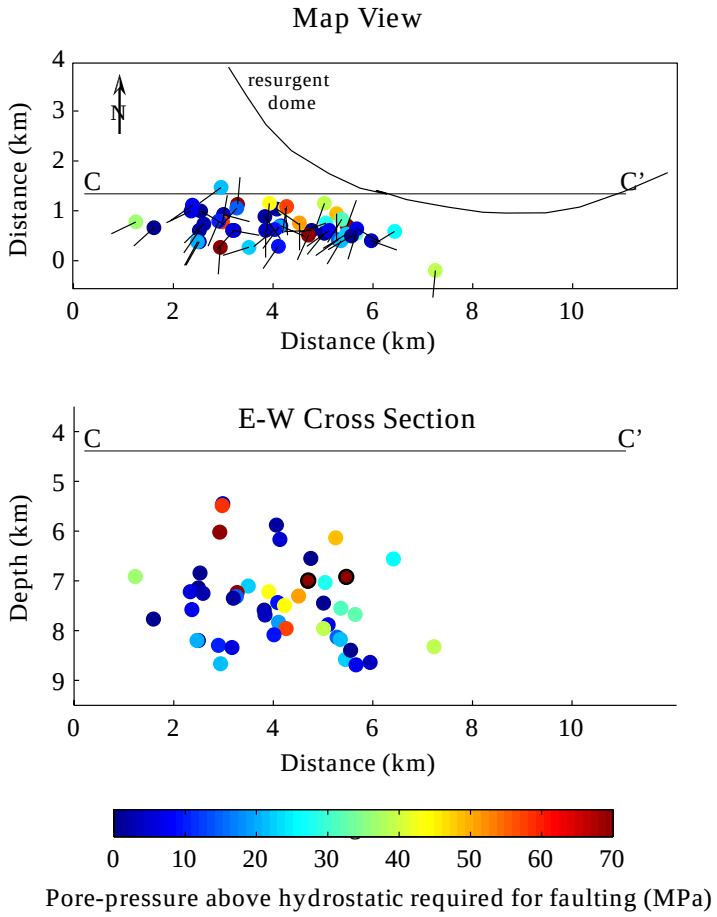

Figure 5.19 - Map (upper) and east / west cross section (lower) showing distribution of minimum pore pressures required to cause faulting (assuming constant friction) based on Mohr-Coulomb theory. Lines in upper panel indicate strike direction for the nodel plane better oriented for failure for each event. Reverse faulting earthquakes #2 and #4 from Figure 5.11 are outlines in black in lower panel.

Many earthquakes in the November 22, 1997 swarm require an elevated pore pressure of < 30 MPa, relative to hydrostatic, to fail in the calculated stress field. However, some earthquakes, including the reverse faulting events number 2 and 4 in Figure 5.11 (red dots outlined in Figure 5.19) require increased pore pressures of up to 90 MPa before failure is expected to occur. Earthquakes which require the highest pore pressures are generally located in the center of the

WSMSZ on November 22, 1997, suggesting that there were pockets of high pore pressure during the migrating seismicity sequence. However, overall there is no spatially or temporally coherent pattern to the pore pressure distribution depicted in Figure 5.19.

By comparing the spatial distribution of stress inversion misfits in Figure 5.15 with the spatial distribution of pore pressure in Figure 5.19, we can draw conclusions about the physical interpretation of misfits. For example, the reverse faulting events number 2 and 4 in Figure 5.11 are poorly oriented for failure since they require high pore pressure to fail (Figure 5.19), yet they have low misfits to the stress field on November 22, 1997 (Figure 5.15). Whereas, some planes which are well oreinted for failure have high misfits. Thus misfit does not reflect how well planes are oriented for failure. The fault planes of earthquakes with high misfits may be groved, such that the texture of the fault plane strongly influences the sense of slip.

5.7 Synthesis: A Conceptual Model for November 22, 1997 West South Moat Seismicity

Based on the evidence described above, we now propose a conceptual model for the development of the November 22, 1997 west south moat seismic zone earthquake swarm. While this scenario is obviously speculative, it provides a reasonable explanation for all observations described in this chapter (seismicity migration, deformation data, highly diverse focal mechanisms, NDC earthquakes, spasmodic bursts, earthquakes with long-duration or long-period source processes).

We suggest that magma intruding into the caldera in 1997 induced a high pressure transient in the basement rock of the south moat on November 22 due to either fluid exsolution from rising magma or magmatic heating of preexisting

fluids. These highly pressurized fluids may have triggered the first **M** 4.6 earthquake by decreasing the effective normal stress across the fault. If the first **M** 4.6 earthquake had a typical stress drop (5 MPa), the earthquake would have ruptured an area with a diameter of 2 km. Thus, the first **M** 4.6 earthquake may have provided a pathway for the rapid transport of fluids through the western south moat seismic zone.

Following the first **M** 4.6 event, we suggest that fluids propagated upward and westward away from their source along subadjacent faults throughout the WSMSZ1. The high pressures associated with this fluid movement decreased the effective normal stress across faults, causing rapid-fire failure on subadjacent faults and the observed spasmodic bursts. The high diversity in wave forms, focal mechanisms, and fault strikes (Figure 5.19) for these events suggests that the earthquakes in the migration sequence occurred on a network of interconnected faults of widely varying orientation throughout a volume of crust rather than near the tip of an expanding fault. Where the pressure transient propagating through this volume of crust raised pore pressures to the minimum compressive stress, hydraulic fracturing and NDC earthquakes occurred. In the case of some earthquakes, the fluids may have excited resonance in the walls of fractures they traveled through, causing the unusually emergent and relatively long-period earthquakes.

The anomalous strain signal observed at POPA (Figure 5.3) directly suggests that fluids (possibly magma) began intruding into the caldera's south moat during the middle of the migration sequence, beginning near the time of the **M** 4.9 earthquake (17:20 UTC). Thus, the seismic rupture of faults triggered by magmatic fluids may have provided conduits for magma to move toward the Earth's surface. However, there is no evidence for the direct involvement of magma in the source process of these earthquakes.

Our relocations indicate that the seismicity migration extended upwards to within 5 km of the caldera floor. If this migration was caused by a high pressure transient due to magmatic intrusion, as we propose, and if this transient had maintained high pressures to depths of ~1 km, the November 22, 1997 migrating seismicity sequence might have culminated in a phreatic eruption (D. Hill, personal communication, 2001). The development of previous west south moat seismic zone earthquake swarms and their focal mechanisms imply that the processes which triggered seismicity on November 22, 1997 are recurring in the caldera's west south moat.

5.8 Summary

A close examination of seismicity on November 22, 1997 in the western south moat of the Long Valley caldera reveals that this seismic swarm may have been triggered by magmatically-derived fluids. Observations that lead to this conclusion include migrating seismicity, moment tensor solutions with volumetric components, spasmodic bursts, highly variable focal mechanisms, and earthquakes with unusually emergent and low-frequency-enriched source processes. These observation imply that on November 22, 1997, a high pressure transient emanated from a magma body intruding into the caldera. It propagated upward and westward away from its source through the west south moat seismic zone, decreasing the normal stress across faults and triggering earthquakes as it migrated.

Although focal mechanisms for earthquakes in this sequence were highly diverse with many poorly oriented fault planes, slip appears to have occurred in response to local tectonic stresses described in Chapter 3. Thus, although magmatic activity triggered seismicity by decreasing the effective normal stress across faults, earthquakes slipped in accordance with the tectonic stress field.

References

Abercrombie, R. E., Earthquake source scaling relationships from -1 to 5 M_L using seismograms recorded at 2.5 km depth, *J. Geophys. Res., 100*, 24015-24036, 1995.

Abercrombie, R. E., Near surface attenuation and site effects from comparison of surface and deep borehole recordings, *Bull. Seism. Soc. Am., 87*, 731-744, 1997.

Abercrombie, R. E., A summary of attenuation measurements from borehole recordings of earthquakes: the 10 Hz transition problem, *Pure Appl. Geophys., 153*, 475-487, 1998.

Aki, K., Scaling Law of Seismic Spectrum, *J. Geophys. Res., 72*, 1217-1231, 1967.

Aki, K. and P. G. Richards, *Quantitative seismology: theory and methods*, pp. 913, 1980.

Anderson, J. G., Implication of attenuation for studies of the earthquake source, in *Earthquake Source Mechanics, Geophysical Monograph 37*, American Geophysical Union, 311-318, 1986.

Anderson, J. G. and S. Hough (1984). A model for the shape of the Fourier amplitude spectrum of acceleration at high frequencies, *Bull. Seism. Soc. Am., 74*, 1969-1994.

Archuleta, R. J., S. H. Seale, P. V. Sangas, L. M. Baker, and S. T. Swain, Garner Valley downhole array of accelerometers: instrumentation and preliminary data analysis, *Bull. Seism. Soc. Am., 82*, 1592-1621, 1992.

Archuleta, R. J., E. Cranswick, C. Mueller, and P. Spudich, Source parameters of the 1980 Mammoth Lakes, California earthquake sequence, *J. Geophys. Res., 87*, 4595-4607, 1982.

Archuleta, R. J., Downhole recordings of seismic radiation, in *Earthquake Source Mechanics, Geophysical Monograph 37*, American Geophysical Union, 319-329, 1986.

Aster, R. C. and P. M. Shearer, High-frequency borehole seismograms recorded n the San Jacinto fault zone, southern California: Part 2. Attenuation and side effects, *Bull. Seism. Soc. Am., 81*, 1081-1100, 1991.

Baer, G., Mechanics of dike propagation in layered rocks and in massive, porous sedimentary rocks, *J. Geophys. Res., 96*, 11911-11929, 1991.

Bailey, R., Geologic map of the Long Valley caldera, Mono-Inyo craters volcanic chain, and vicinity, eastern California, *U.S. Geol. Surv. Misc. Inv. Ser.* 0160-0753 pp., 1989.

Battaglia, M., C. Roberts, and P. Segall, Magma intrusion beneath Long Valley caldera confirmed by temporal changes in gravity, *Science, 285*, 2119-2122, 1999.

Bellier, O., and M. L. Zoback, Recent state of stress change in the Walker Lane zone, western Basin and Range province, United States, *Tectonics, 14*, 564-593, 1995.

Blakeslee, S. and P. Malin, High-frequency site effects at two Parkfield downhole surface stations, *Bull. Seism. Soc. Am., 81*, 332-345, 1991.

Brune, J. N., Tectonic stress and seismic shear waves from earthquakes, *J. Geophys. Res., 75*, 4997-5009, 1970.

Bursik, M., and K. Sieh, Range front faulting and volcanism in the Mono Basin, eastern California, *J. Geophys. Res., 94*, 15587-15609, 1989.

Chouet, B., A seismic model for the source of long-period events and harmonic tremor, *Volcanic Seismology, 3,* P. Gasparini, R. Scapa, and K. Aki (eds.), 133-156, 1992.

Clark, M.M. and A. R. Gillespie, Record of late Quaternary faulting along the Hilton Creek fault in the Sierra Nevada, California, *SSA Earthquake Notes, 52,* 46, 1981.

Cramer, C. H. and S. R. McNutt, Spectral analysis of earthquakes in the 1989 Mammoth Mountain swarm near Long Valley, California, *Bull. Seism. Soc. Am., 87*, 1454-1462, 1997.

Cramer, C. H., and T. R. Toppozada, A seismological study of the May 1980, and earlier earthquake activity near Mammoth Lakes, California, *Mammoth Lakes, California earthquakes of May 1980, California Division of Mines and Geology Special Report*, Sherburne, W. R. (ed), 91-122, 1980.

Dreger, D. S., H. Tkalcic, and M. Johnston, Dilatational processes accompanying earthquakes in the Long Valley caldera, *Science, 288,* 122-125, 2000.

Eichelberger, J. C., C. R. Carrigan, H. R. Westrich, R. H. Price, Nonexplosive silicic volcanism, *Nature, 323,* 598-602, 1986.

Ellsworth, W.L., F. Waldhauser, and A. Cole, A new view of the San Andreas fault: Implications for earthquake interaction at Parkfield: 17th Course, International School of Geophysics, Fault Interaction by Stress Transfer: New Horizons for Understanding Earthquake Occurrence, 2000.

Eshelby, J. D., The determination of the elastic field of an ellipsoidal inclusion and related problems, *Proc. R. Soc. London, 241,* 376-396, 1975.

Farrar, C. D., M. L. Sorey, W. C. Evans, J. F. Howle, B. D. Kerr, B. M. Kennedy, C.-Y. King, and J. R. Southon, Forest-killing diffuse CO_2 emission at Mammoth Mountain as a sign of magmatic unrest, *Nature, 376,* 675-678, 1995.

Foulger, G. R., B. R. Julian, D. P. Hill, A. M. Pitt, P. E. Malin, and E. Shalev, Evidence of hydraulic fracturing in non-double-couple microearthquakes at Long Valley caldera, California, in preparation.

Gephart, J. W., FMSI: A FORTRAN program for inverting fault/slickenside and earthquake focal mechanism data to obtain the regional stress tensor, *Comput. Geosci., 16,* 953-989, 1990.

Gephart, J. W. and D. W. Forsythe, An improved method for determining the regional stress tensor using earthquake focal mechanism data: Application to the San Fernando earthquake sequence, *J. Geophys. Res., 89,* 9305-9320, 1984.

Gibbs, J. F., D. M. Boore, W. B. Joyner, and T. E. Fumal, The attenuation of seismic shear waves in Quaternary alluvium in Santa Clara valley, California, *Bull. Seism. Soc. Am., 84,* 76-90, 1994.

Given, J. W., T. C. Wallace, and H. Kanamori, Teleseismic analysis of the 1980 Mammoth Lakes earthquake sequence, *Bull. Seismol. Soc. Am., 72,* 1093-1109, 1982.

Hanks, T. C., $f_{\max}$, *Bull. Seism. Soc. Am., 72,* 1867-1879, 1982.

Hardebeck, J. L. and E. Hauksson, Stress orientations obtained from earthquake focal mechanisms: What are appropriate uncertainty estimates?, *Bull. Seismol. Soc. Am., 91,* 250-262, 2001.

Haskell, N., Radiation pattern of surface waves from point sources in a multi-layered medium, *Bull. Seism. Soc. Am., 54,* 1811-1841, 1964.

Hauksson, E., T. L. Teng, and T. L. Henyey, Results form a 1500 m deep, three-level downhole seismometer array: site response, low Q values and $f_{\max}$, *Bull. Seism. Soc. Am., 77,* 1883-1904, 1987.

Hildreth, W., The Bishop Tuff: Evidence for the origin of compositionally zoned magma chambers, *Geol. Soc. Am. Spec. Pap. No., 180*, 43-75, 1979.

Hill, D. P., D. Dzurisin, W. L. Ellsworth, E. T. Endo, D. L. Galloway, T. M. Gerlach, M. S. J. Johnston, K. A. McGee, C. D. Miller, D. Oppenheimer, and M. L. Sorey, Response plans for volcanic hazards in the Long Valley caldera and Mono craters area, California, *U.S. Geological Survey Bulletin 2185*, in press.

Hill, D. P., R. A. Bailey, and A. S. Ryall, Active tectonic and magmatic processes beneath Long Valley caldera, eastern California: an overview, *J. Geophys. Res., 90*, 11111-11120, 1985.

Hill, D. P., W. L. Ellsworth, M. J. S. Johnston, J. O. Langbein, D. H. Oppenheimer, A. M. Pitt, P. A. Reasenberg, M. L. Sorey, and S. R. McNutt, The 1989 earthquake swarm beneath Mammoth Mountain, California: An initial look at the 4 May through 30 September activity, *Bull. Seismol. Soc. Am., 80*, 325-339, 1990.

Hough, S. E. and J. G. Anderson, High frequency spectra observed at Anza, California: Implications for Q structure, *Bull. Seism. Soc. Am., 78*, 692-707, 1988.

Hough , S. E., J. M. Lees, and F. Monastero, Attenuation and source properties at the Coso geothermal area, California, *Bull. Seism. Soc. Am., 89*, 1606-1619, 1999.

Hough, S. E., R. S. Dollar, and P. Johnson, The 1998 earthquake sequence south of the Long Valley caldera, California: Hints of magmatic involvement, *Bull. Seism. Soc. Am., 90*, 752-763, 2000.

Hubbert, M. K., and D. G. Willis, Mechanics of hydraulic fracturing, *Petroleum Trans. AIME, 210*, 153-163, 1957.

Ide, S., G. C. Beroza, S. G. Prejean, and W. L. Ellsworth, Does apparent stress vary with earthquake size? Possible mechanism of artificial size dependency, *EOS Trans. Am. Geophys. Un., 82*, F843, 2001.

Jongmans, D. and P. E. Malin, Vertical profiling of microearthquake S waves in the Varian well at Parkfield, California, *Bull. Seism. Soc. Am., 85*, 1805-1820, 1995.

Julian, B. R., Volcanic Tremor: Nonlinear excitation by fluid flow, *J. Geophys. Res., 6*, 11859-11878, 1994.

Julian, B. R., and S. A. Sipkin, Earthquake processes in the Long Valley caldera area, California, *J. Geophys. Res., 04*, 11155-11169, 1985.

Julian, B. R., G. R. Foulger, D. P. Hill, A. M. Pitt, P. E. Malin, and E. Shalev, Moment tensors of volcanic microearthquakes at Long Valley caldera, Eastern

California, *EOS Trans. Am. Geophys. U., 80,* F665, 1999.

Kanamori, H., J. Mori, E. Hauksson, T. H. Heaton, L. K. Hutton, and L. Jones, Determination of earthquake energy release and M_L using TERREscope, *Bull. Seism. Soc. Am., 83,* 330-346, 1993.

Kikuchi, M. and Y. Fukao, Seismic wave energy inferred from long-period body wave inversion, *Bull. Seism. Soc. Am., 78,* 1707-1722, 1988.

Knopoff, L., Q, *Rev. Geophys., 2,* 625-660, 1964.

Langbein, J., Deformation of the Long Valley caldera, eastern California from mid-1983 to mid-1988: Measurements using a two-color geodimeter, *J. Geophys. Res., 94,* 3833-3849, 1989.

Langbein, J., S, Wilkinson, M. J. S. Johnston, J. Feinberg, and R. Bilham, The 1997–98 inflation of Long Valley caldera and comparison with 1989–95 episode, *EOS Trans. Am. Geophys. Un., 79,* F963, 1998.

Langbein, J., D. Dzurisin, G. Marshall, R. Stein, and J. Rundle, Shallow and peripheral volcanic sources of inflation revealed by modeling two-color geodimeter and leveling data from Long Valley caldera, California, 1988-1992, *J. Geophys. Res., 100,* 12487-12495, 1995.

Lee, W. H. K. and J. C. Lahr, HYPO71 (revised): A computer program for determining hypocenter, magnitude, and first motion pattern of local earthquakes, *U.S. Geological Survey Open-File Report 75-311,* 100 pp, 1975.

Madariaga, R., Dynamics of an expanding circular fault, *Bull. Seism. Soc. Am., 66,* 639-666, 1976.

Magee, M. E. and M. D. Zoback, Mapping variations in fault strength using earthquake focal mechanisms, *EOS Trans. Am. Geophys. Un., 78,* F702, 1997.

Malin, P. E., J. A. Waller, R. D. Borcherdt, E. Cranswick, E. G. Jensen, and J. Van Schaack, Vertical seismic profiling of Oroville microearthquakes: velocity spectra and particle motion as a function of depth, *Bull. Seism. Soc. Am., 78,* 401-420, 1988.

Marshall, G. A., J. Langbein, R. S. Stein, M. Lisowski, and J. Svarc, Inflation of Long Valley caldera, California, Basin and Range strain, and possible Mono Craters dike opening from 1990-94 GPS surveys, *Geophys. Res. Let., 24,* 1003-1006, 1997.

Mayeda K. and W. R. Walter, Moment, energy, stress drop, and source spectra of

western United States earthquakes from regional coda envelopes, *J. Geophys. Res., 101,* 11195-11208, 1996.

McConnell, V. S., J. W. Valley, and J. C. Eichelberger, Oxygen isotope compositions of intracaldera rocks: hydrothermal history of the Long Valley caldera, California, *J. Volcan. Geotherm. Res., 76,* 83-109, 1997.

McGarr, A., On relating apparent stress to the stress causing earthquake fault slip, *J. Geophys. Res., 104,* 3003-3011, 1999.

McGee, K. A., T. M. Gerlach, R. Kessler, and M. P. Doukas, Geochemical evidence for a magmatic CO_2 degassing event at Mammoth Mountain, California, September-December 1997, *J. Geophys. Res., 105,* 8447-8456, 2000.

McKenzie, D. P., The relation between fault plane solutions for earthquakes and the directions of the principal stresses, *Bull. Seismol. Soc. Am., 59,* 591-601, 1969.

Menke, W. and B. D. Dubendorff, Discriminating intrinsic and apparent attenuation in layered rock, *Geophys. Res. Lett., 12,* 721-724, 1985.

Michael, A. J., Use of focal mechanisms to determine stress: A control study, *J. Geophys. Res., 92,* 357-368, 1987.

Moos, D. and M. D. Zoback, State of stress in the Long Valley caldera, California, *Geology, 21,* 837-840, 1993.

Niitsuma, H., K. Nakatsuka, N. Chubachi, H. Yokoyama, and M. Takanoshishi, Acoustic emission measurement of geothermal reservoir cracks in the Takinoue (Kakkonda) field, Japan, *Geothermics, 14,* 525-538, 1985.

Nettles, M. and G. Ekstrom, Faulting mechanism of anomalous earthquakes near Bardarbunga volcano, Iceland, *J. Geophys. Res., 103,* 17973-17983, 1998.

Ode, H., Mechanical analysis of the dike pattern of the Spanish Peaks area, Colorado, *Geological Society of America Bulletin, 68,* 567-576, 1957.

Orowan, E., Mechanism of seismic faulting, *Geol. Soc. Am. Mem., 79,* 323-345, 1960.

Pitt, A. M. and D. P. Hill, Long-period earthquakes in the Long Valley caldera region, eastern California, *Geophys. Res. Lett., 21,* 1679-1682, 1994.

Reasenberg, P. A. and D. Oppenheimer, FPFIT, FPPLOT, and FPPAGE: Fortran computer programs for calculating and displaying earthquake fault-plane solutions, *U.S. Geological Survey Open-File Report 85-739,* 27 pp, 1985.

Roeloffs, E. A., M. Sneed, D. L. Galloway, E. G. Quilty, M. L. Sorey, C. D. Farrar, and J. Hughes, Water level changes at Long Valley caldera, California, following distant and local earthquakes, *EOS Trans. Am. Geophys. Un., 80,* F980, 1999.

Roeloffs, E.A., M. Sneed, D.L. Galloway, M.L. Sorey, E.G. Quilty, C. D. Farrar, and J. Hughes, Water level changes induced by local and distant earthquakes at Long Valley caldera, California, in preparation.

Ryall, A. S., and F. Ryall, Spasmodic tremor and possible magma injection in Long Valley caldera, eastern California, *Science, 219*,1432-1433, 1983.

Sackett, P. C., McConnell, V. S., Roach, A. L., Priest, S. S., and J. H. Sass, Long Valley Coring Project, 1998 - preliminary stratigraphy and images of recovered core, *U. S. Geol. Surv. Open-File Rep. 99-158,* pp. 13., 1999.

Sanders, C. O. and L. D. Nixon, S wave attenuation structure in Long Valley caldera, California, from three-component S-to-P amplitude ratio data, *J. Geophys. Res., 100***,** 12395-12404, 1995.

Sato, T. and T. Hirasawa, Body wave spectra from propagating shear cracks, *J. Phys. Earth, 21,* 415-431, 1973.

Savage, L. C. and R. S. Cockerham, Earthquake swarm in Long Valley caldera, California, January 1983: Evidence for dike inflation, *J. Geophys. Res., 89***,** 8315-8324, 1984.

Sherbaum, F., *Of poles and zeros: fundamentals of digital seismology*, Kluwer Academic Press, 256pp., 1996.

Simons, M., Y. Fialko, L. Rivera, E. Chapin, S. Hensley, P. A. Rosen, S. Shaffer, F. H. Webb, and J. Langbein, Analysis of geodetic measurements of crustal deformation at Long Valley caldera, *EOS Trans. Am. Geophys. Un., 81,* F1322, 2000.

Singh, S. K. and M. Ordaz, Seismic energy release in Mexican subduction zone earthquakes, *Bull. Seism. Soc. Am., 84,* 1533-1550, 1994.

Stroujkova, A. and P. Malin, A magma mass beneath Casa Diablo? Further evidence from reflected seismic waves, *Bull. Seism. Soc. Am., 90,* 500-511, 2000.

Toda, S., R. S. Stein, P. A. Reasenberg, and J. H. Dieterich, Stress transferred by the Mw=6.5 Kobe, Japan, shock: Effect on aftershocks and future earthquake probabilities, *J. Geophys. Res., 103*, 24543-24565, 1998.

Townend, J. and M. D. Zoback, How faulting keeps the crust strong, *Geology, 28,* 399-402, 2000.

Vetter, U. R., and A. S. Ryall, Systematic change of focal mechanism with depth in the western Great Basin, *J. Geophys. Res., 88,* 8237-8250, 1983.

Waldhauser, F., hypoDD - A program to compute double-difference hypocenter locations, *U.S. Geological Survey Open-File Report 01-113,* 25 pp, 2001.

Waldhauser, F. and W. L. Ellsworth, A double-difference earthquake location algorithm: Method and application to the northern Hayward fault, California, *Bull. Seismol. Soc. Am., 90* 1353-1368, 2000.

Wallace T., J. Given, and H. Kanamori, A discrepancy between long- and short-period mechanisms of earthquakes near the Long Valley caldera, *Geophys. Res. Lett., 10,* 1131-1134, 1982.

Wallace, T. C., A reexamination of the moment tensor solutions of the 1980 Mammoth Lakes earthquakes, *J. Geophys. Res., 90,* 11171-11176, 1985.

Winkler, K. W. and A. Nur, Seismic attenuation: effects of pore fluids and frictional sliding, *Geophysics, 47,* 1-15, 1982.

Zoback, M. L., State of stress and modern deformation of the northern Basin and Range province, *J. Geophys. Res., 94,* 7105-7128, 1989.